PHASOR PARAMETER MODELING AND TIME-SYNCHRONIZED CALCULATION FOR REPRESENTATION OF POWER SYSTEM DYNAMICS

A Dissertation

by

CHENG QIAN

Submitted to the Office of Graduate and Professional Studies of
Texas A&M University
in partial fulfillment of the requirements for the degree of

DOCTOR OF PHILOSOPHY

Chair of Committee,	Mladen Kezunovic
Committee Members,	Thomas J. Overbye
	Srinivas Shakkottai
	Suman Chakravorty
Head of Department,	Miroslav M. Begovic

December 2020

Major Subject: Electrical Engineering

ABSTRACT

The electric power grid is undergoing sustained disturbances. In particular, the extreme dynamic events disrupt normal electric power transfer, degrade power system operating conditions, and may lead to catastrophic large-scale blackouts. Accordingly, control applications are deployed to detect the inception of extreme dynamic events, and mitigate their causes appropriately, so that normal power system operating conditions can be restored. In order to achieve this, the operating conditions of the power system should be accurately characterized in terms of the electrical quantities that are crucial to control applications. Currently, the power system operating conditions are obtained through SCADA system and the synchrophasor system. Because of GPS time-synchronized waveform sampling capability and higher measurement reporting rate, synchrophasor system is more advantageous in tracking the extreme dynamic operating conditions of the power system.

In this work, a phasor parameter calculation approach is proposed to accurately characterize the power system operating conditions during the extreme electromagnetic and electromechanical dynamic events in the electric power grid. First, a framework for phasor parameter calculation during both electromagnetic and electromechanical dynamic events is proposed. The framework aims to satisfy both P-class and M-class PMU algorithm design accuracy requirements with a single algorithm. This is achieved by incorporating an adaptive event classification and algorithm model switching mechanism, followed by the phasor parameter definition and calculation tailored to each identified event. Then, a phasor estimation technique is designed for electromagnetic transient events. An ambient fundamental frequency estimator based on UKF is introduced, which is leveraged to adaptively tune the DFT-based algorithm to alleviate frequency

leakage. A hybridization algorithm framework is also proposed, which further reduces the negative impact caused by decaying DC components in electromagnetic transient waveforms. Then, a phasor estimation technique for electromechanical dynamics is introduced. A novel wavelet is designed to effectively extract time-frequency features from electromechanical dynamic waveforms. These features are then used to classify input signal types, so that the PMU algorithm modeling can be thereafter tailored specifically to match the underlying signal features for the identified event. This adaptability of the proposed algorithm results in higher phasor parameter estimation accuracy. Finally, the hypothesis is validated through experimental testing under design and application test use cases. The associated test procedures, test use cases, and test methodologies and metrics are defined and implemented. The impact of algorithm inaccuracy and communication network distortion on application performance is also demonstrated. Test results performance is then evaluated. Conclusions, contributions, and future steps are outlined at the end.

DEDICATION

To my parents, who have made unimaginable sacrifice for me to be here today.

ACKNOWLEDGEMENTS

I would like to cordially thank my doctorate advisor, Professor Mladen Kezunovic, from whom I have learned tremendously. I would like to also thank the rest of my committee members, Professor Thomas Overbye, Professor Srinivas Shakkottai and Professor Erchin Serpedin from the Department of Electrical and Computer Engineering, and Professor Suman Chakravorty from the Department of Aerospace Engineering.

I would also like to acknowledge the friends, professors, and mentors, who have accompanied me in this endeavor. I am grateful to you all.

Finally, I would also like to thank my dog Nibbler, who has always been a loyal companion for me, and given me hope during my fight against depression.

CONTRIBUTORS AND FUNDING SOURCES

Contributors

This work work will not be completed without the encouraging and invigorating team-work with Mr. Christoph Seidl, Dr. Payman Dehghanian, Dr. Ahad Esmaeilian, and Dr. Jinfeng Ren, as well as the rest of my Dissertation committee: Professor Thomas Overbye, Professor Srinivas Shakkottai, and Professor Suman Chakravorty

Funding sources

Part of the theoretical development and experimental validation work was conducted in conjunction with the following projects:

Power System Engineering Research Center (PSERC) T-57 High Impact project titled "Management of Mission-Critical Systems Through Certification, Commissioning, In-Service Maintenance, Remote Testing, and Risk Assessment."

US Department of Energy/National Energy Technology Laboratory, Cybersecurity for Energy Delivery Systems (CEDS) program project titled "Timing Intrusion Management Ensuring Resiliency (TIMER)."

NOMENCLATURE

AC	Alternating Current
AM	Amplitude Modulation
AWGN	Additive White Gaussian Noise
CVT	Capacitor Voltage Transformer
CT	Current Transformer
CWT	Continuous Wavelet Transform
dBm	decibels referenced to one milliwatt, also known as, dB_{mW}
DFT	Discrete Fourier Transform
DTFT	Discrete-time Fourier transform
DWT	Discrete Wavelet Transform
EKF	Extended Kalman Filter
EMTP	Electromagnetic Transient Program
EMS	Energy Management System
FE	Frequency Error
FFT	Fast Fourier Transform
FM	Frequency Modulation
FOR	Frequency Occurrence Rate
FWT	Fast Wavelet Transform
f_0	nominal frequency in Hz
Δf_{DFT}	DFT bin in Hz, or DFT resolution
$\Delta \omega_{\mathrm{DFT}}$	DFT bin in rad/s, or DFT resolution

ω_0	nominal frequency ($= 2\pi f_0$) in rad/s
f_{in}	fundamental frequency of the sinusoidal signal input in Hz
GPS	Global Positioning System
IEC	International Electrotechnical Committee
IED	Intelligent Electronic Device
IEEE	Institute of Electrical and Electronics Engineers
i.f.f.	if, and only if
IpDFT	Interpolated Discrete Fourier Transform
IRIG-B	Inter-Range Instrumentation Group time code, format B
LMA	Levenberg-Marquardt Algorithm
l.h.s.	left hand side
MMSE	Minimum Mean Square Error
N	data window length in number of samples
NIST	National Institute of Standards and Technology
PDC	Phasor Data Concentrator
PLC	Programmable Logic Controller
PMU	Phasor Measurement Unit
PPS	Pulse Per Second
PT	Potential Transformer
r.h.s.	right hand side
RMS	Root-Mean-Square value
ROCOF	Rate of Change of Frequency
RTU	Remote Terminal Unit

SCADA	Supervisor Control and Data Acquisition
SMIB	Single Machine Infinite Bus
SNR	Signal-to-Noise Ratio
STFT	Short-Time (Term) Fourier Transform
SOC	Second of Century
TAI	Temps Atomique International, International Atomic Time
TOR	Time Occurrence Rate
TVE	Total Vector Error
UTC	Temps Universel Coordonné, Universal Coordinated Time
UKF	Unscented Kalman Filter
w.r.t.	with respect to
WT	Wavelet Transform
WWVB	WWVB radio station, operated by NIST

TABLE OF CONTENTS

Page

LIST OF FIGURES

Page

LIST OF TABLES

Page

1. INTRODUCTION

The electric power system is a geographically distributed infrastructure constructed and controlled to transfer electric power from power generation (power source) to power consumption (load). The power system is constantly experiencing disturbances with various levels of severity. Minor disruptions, such as variations in load demand, do not interrupt normal power system operation. Major disturbances, such as faults on transmission lines, on the other hand, may significantly disrupt power transfer, and cause power outages. If left unmitigated, local disturbances may initiate successive outages over a large geographically distributed area, resulting in large-scale cascading blackout.

Accordingly, control applications are deployed in the power systems to mitigate the cause of major disturbances. These applications evaluate the level of security of current operating state [1]-[2], detect abnormal operating conditions [3]-[4], and take necessary actions to minimize the impact of disturbances [5]-[6]. In order to facilitate control applications, the operating conditions of the power system should be monitored with adequate accuracy and speed.

This work contributes to the methodological approach to the characterization of power system dynamic operating conditions in terms of electrical quantities. In particular, this work proposes an algorithm that characterizes power system sinusoidal waveforms in terms of their corresponding phasor parameters: amplitude, phase angle, and frequency. In order to facilitate end-use control applications, the design of algorithms is constrained by the accuracy and computational time requirements imposed by the applications. The context of this Dissertation work is depicted in Figure 1.

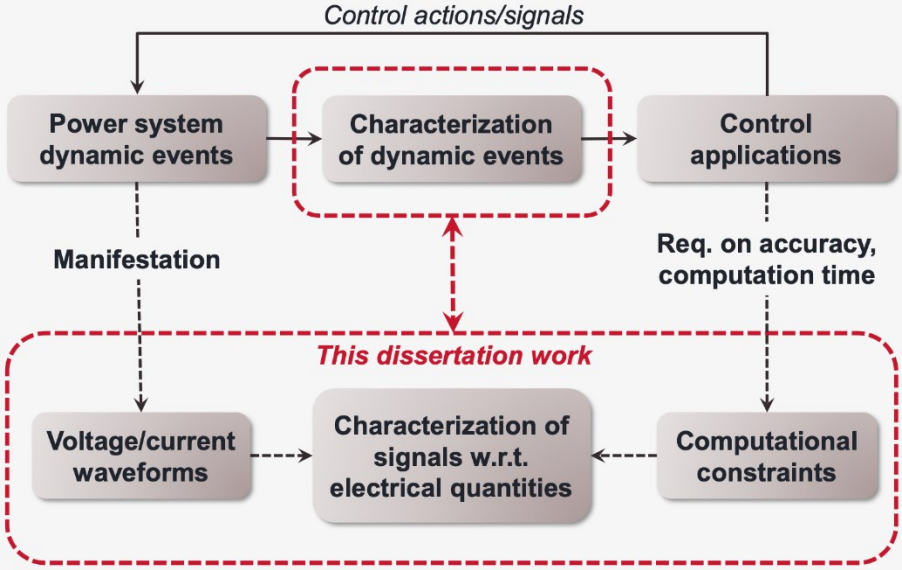

Figure 1 Background of the Dissertation work

Practically, the electrical quantities are calculated from phasor parameters, which are tracked by field devices (e.g. transducers, IEDs, PMUs) situated in substations, and are calculated from digitized power waveform measurements (samples). The monitoring infrastructures that support the provision of phasor parameters are discussed in the next Chapter.

2. BACKGROUND

2.1 Power System Monitoring Infrastructures

Currently, power system operating conditions are surveilled by two monitoring infrastructures: the SCADA system, and the GPS time-synchronized phasor measurement system. The properties of SCADA and synchrophasor systems are elaborated next.

2.1.1 Properties of SCADA System

The SCADA system has been in use for decades. Shown in Figure 2 is the data flow in SCADA system. The electrical quantities, such as RMS voltage and current, frequency, and active and reactive power are tracked by the IEDs and transducers situated in the substation control house and switchyard. Data from field devices are aggregated by RTUs and PLCs through data scanning [7]. The aggregated data collected by PLCs can be used to perform local control actions in substations, as described in [8]. Periodically polled by control center servers, RTUs may upload measurement data through radio waves, transmission lines, or other dedicated media [7]. The measurement data from RTUs are polled at various rates depending on the electrical quantity of interest, as well as the application in which the electrical quantities will be used. As regulated in standard [7], this measurement data rate varies from every 2-30 seconds. In the server station located in a control center, electrical quantity is time-stamped once it is collected by the RTUs installed in a widely dispersed area.

In SCADA, phase angle data are not directly calculated from the power system waveform samples in local field devices, but are estimated from the State Estimator application [1] executed in a control center. State Estimator application relies on a nonlinear optimization approach

and estimates phase angle differences using unsynchronized bus voltage magnitudes, line current magnitudes, and active and reactive power injections retrieved from local field sensors.

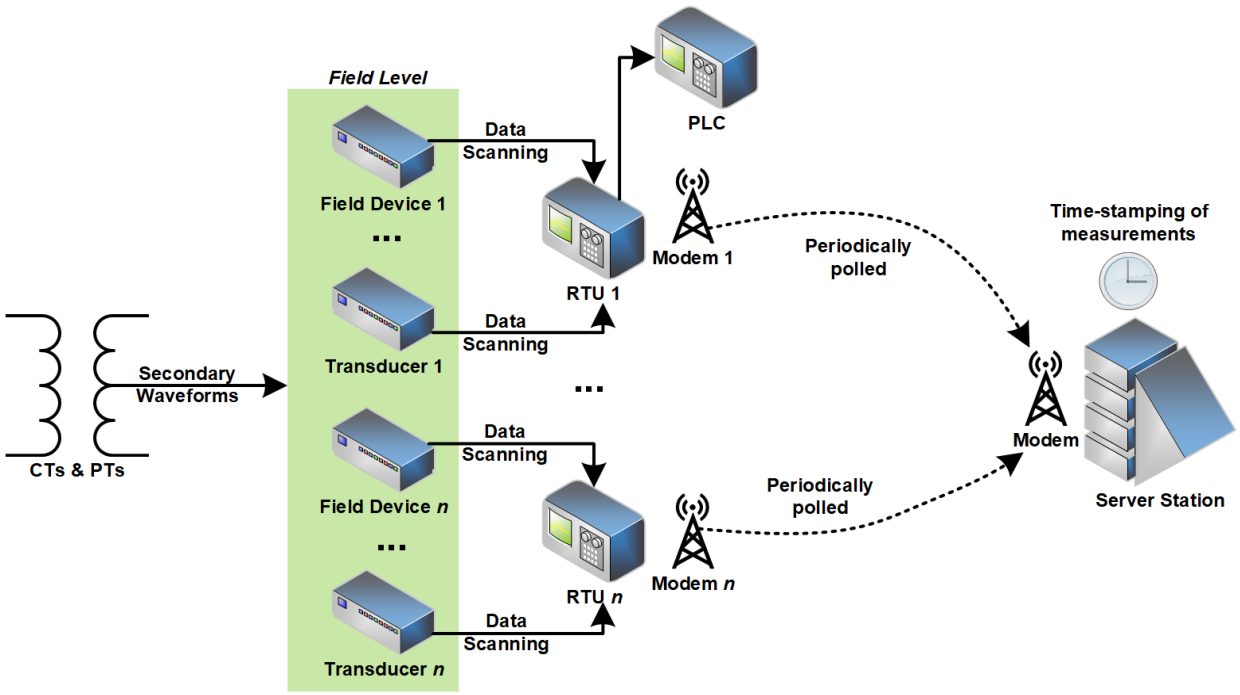

Figure 2 Data flow in SCADA system

2.1.2 Properties of Synchrophasor System

Synchrophasor system emerged in the late 20th century, when synchrophasor technology was introduced, and PMU devices, as well as devices enabled with PMU functionalities*, were deployed in the field. In synchrophasor system, as illustrated in Figure 3, analog secondary waveforms from CTs and PTs/CVTs are synchronously digitized by the data acquisition modules of PMUs. Then, phasor parameters are calculated using waveform samples, assigned GPS-syn-

* PMUs and devices with PMU functionalities are referred to as "PMUs" hereinafter

chronized timestamps, then formatted, packaged, and uploaded through a dedicated communication network to PDCs. The measurement data transfer of phasor parameters is standardized in [10]-[11].

Power system waveforms are synchronously sampled by the PMUs located at different substations. Each calculated phasor parameter is timestamped to GPS time, which is retrieved from substation GPS satellite-synchronized clock receivers. Since GPS satellite signals can be received in most parts of the world with high precision, accurate time-synchronized sampling and phasor parameter timestamping can be achieved at PMUs installed across a large geographically spanned area.

At PDC level, phasor data packets reported by various PMUs are time-aligned based on the timestamp inside each phasor data packet [9]-[11]. This implementation allows power system operators to track the snapshots of power system operating conditions associated with various time instants.

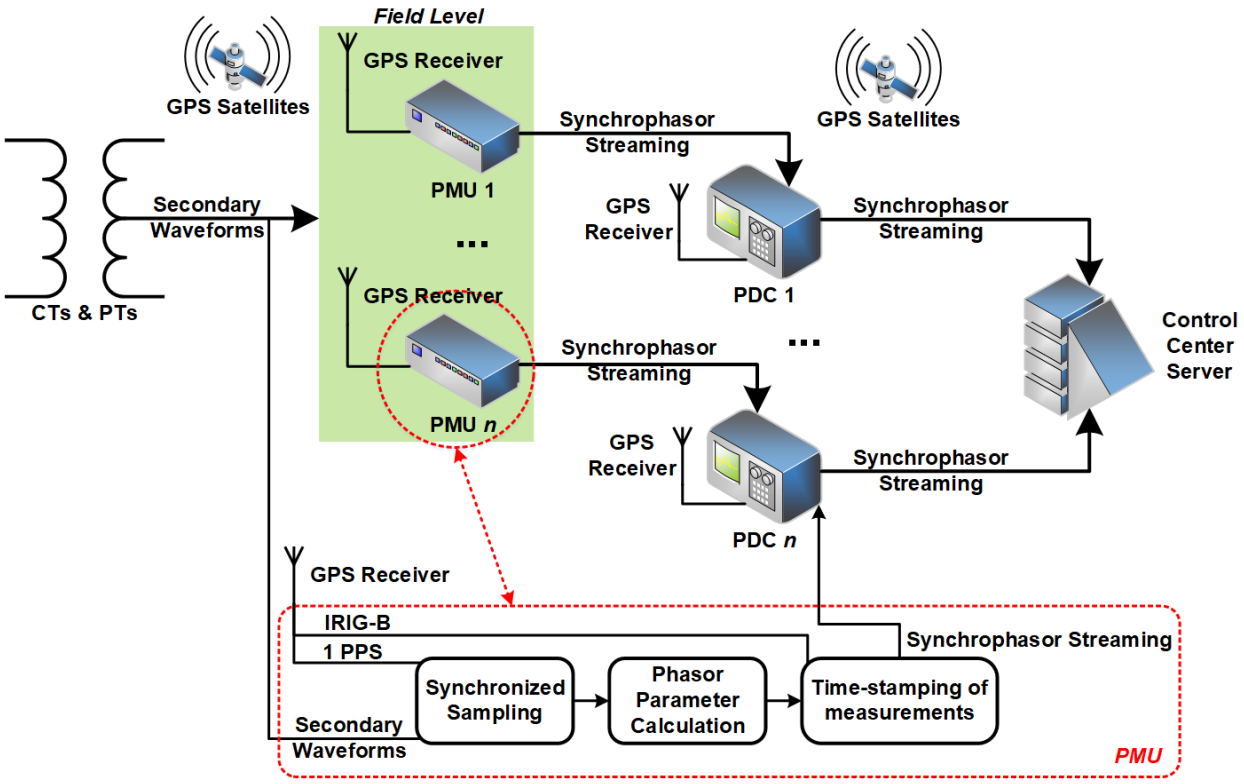

Figure 3 Data flow in synchrophasor system

2.1.3 Shortcomings of SCADA System and Benefits of Synchrophasor Systems

While SCADA has proven to be useful in providing measurement data input for a variety of monitoring and control application in the EMS, it has failed, in numerous cases [12]-[15], to facilitate EMS applications in terms of detecting large-scale blackouts. We analyzed previous catastrophic events, and summarized three primary shortcomings of SCADA, as outlined below:

(1) Phase angle separation cannot be accurately determined. The electrical quantities of interest to power system control applications are those associated with a single location, such as RMS voltage levels; or with multiple locations, such as phase angle separations between different buses. In the SCADA system, phase angles are not directly obtained by local field devices. Rather, phase angles are estimated by EMS State Estimators based on

RMS voltage, network parameters, real and reactive powers [16]. Acquiring phase angle data through state estimation is time-consuming, and results in estimation error.

(2) SCADA measurement data are not time-aligned, resulting in inaccurate even misleading representation of real-time power system operating conditions. This drawback is especially harmful during extreme power system dynamic events, where a spatiotemporal depiction of the power system operating condition is crucial. The time-misalignment of SCADA measurement data is caused by (i). The fact that waveforms are not synchronously captured by local SCADA transducers, and consequently, the accurate timestamps of calculated electrical quantities cannot be determined; (ii). Telemetry delay in communication network. Since the local RTU measurement data travel through communication channels with different telemetry delays, as a result, the SCADA server installed in a remote location cannot accurately compensate this delay, resulting in time-misalignment. Due to the mentioned combined effect, when data is stamped at the control center, an inherent inaccuracy is inevitable.

(3) Another limitation of SCADA system stems from its low measurement reporting rate. According to IEEE standard [7], RTU data are polled by control center servers at reporting rates ranging between 2 and 30 seconds, and it may take tens of minutes for a State Estimator to provide the states of the system [1],[16]. The resolution of reported measurements is not adequate to facilitate real-time control applications that require precise characterization of dynamic event features, and consequently, automated fast response in some instances. As evidenced by previous catastrophic events [12]-[15], a major blackout unfolds in stages, and often deteriorates with multiple regional isolated blackouts, such as in [12]. In each state of the cascade, there are signs indicating the deterioration of vital

electrical quantities, such as the continuous increase of phase angle separations between major buses. During these early stages, power system operators are still able to deploy necessary control actions to salvage the grid from further degradation. Once in its final stage, however, the cascading extreme dynamics in the power system may progress in a matter of a few seconds, leading to an irreversible blackout. With the SCADA measurement data update rate, power system operators may not obtain information regarding the deterioration of operating conditions under extreme dynamics in a timely fashion. This will lead to missing opportunities to rescue the power system from cascading blackouts. With SCADA data alone, situational awareness of the whole power system cannot be achieved with required resolution, and as a result, fast and accurate control actions cannot be adequately and efficiently deployed.

2.2 Time-Synchronized Waveform Sampling and its Significance

As discussed above, to accurately acquire the electrical quantities associated with multiple locations, it is imperative that the waveforms are sampled synchronously at each field device. In order to achieve this, all field devices should reference to the same time source, and the time excursion from such reference time source should be minimized at each local sampling device. Synchrophasor system uses GPS receivers to extract absolute time, and assigns GPS timestamps to calculated phasor measurements at each local device. This strategy has proven to achieve time-synchronization accuracy. A survey in Section 3.2 further discusses various time-synchronization techniques.

2.3 Conclusion

It has been elaborated that synchrophasor system is more suitable for monitoring of power system operating conditions, particularly during extreme dynamic events. This is due to

the adoption of (i). Accurate time-synchronized waveform sampling technique, and (ii). High measurement data reporting rate. Both attributes of the synchrophasor systems contribute to the observation of extreme power system dynamic events with adequate accuracy and resolution, and as a result, the improvement of control application performance in terms of fast and accurate response during extreme dynamic events. In the next Chapter, prior effort on the provision of GPS-synchronized phasor parameters, including synchronized waveform sampling techniques, and algorithmic approach for phasor calculation, is elaborated.

3. PRIOR RESEARCH

3.1 Introduction

This Chapter reviews the state-of-the-art of GPS time-synchronized phasor parameter calculation techniques. Two research areas are surveyed: time-synchronized waveform sampling techniques, and phasor parameter calculation algorithms.

3.2 Time-Synchronized Waveform Sampling Techniques

During dynamic events, the characteristics of waveforms, described by features of electrical quantities, change continuously [17]. In order to accurately characterize phasor parameters at various locations, it is crucial that the phasor parameters at each location are calculated synchronously. This need for time synchronization among measurements prompts the necessity of a common time and angle reference that can be tracked by the PMUs installed across the power grid. Two issues are discussed in the following paragraphs: (i). The interpretation of absolute time by current timing systems; (ii). The dissemination of absolute time from the source to PMUs/PDCs.

The first issue is the interpretation of absolute time by various timing systems. These timing systems include TAI, UTC, and GPS time. TAI time is always ahead of GPS time by 19 seconds. UTC time is aligned with TAI, but also maintains approximate agreement with Universal Time (UT), which is affected by the rotation of earth. Since the Earth is rotating at a decreasing speed, extra seconds (leap seconds) are periodically added in UTC time to compensate for this slowing down. Currently, TAI is leading UTC by 37 leap seconds [18]. When distributed through GPS satellites, absolute time is updated once a second, and is pinpointed to the rising edge of PPS, which is a rectangular signal generated by GPS clocks. Once a GPS clock receiver

receives absolute time and the corresponding PPS, fractions of second can be determined by dividing consecutive seconds into the desired intervals, and this is done internally in the PMU.

The other issue is the dissemination of absolute time from a reference time source. The time code is distributed via broadcasting, which is then decoded by the GPS clock receivers in substations. Two time code distribution strategies are further discussed: WWVB radio wave [19]-[20], and GPS satellite constellation [21].

WWVB radio station, operated by NIST, broadcasts WWVB time code through radio-waves in Fort Collins, Colorado. Even though the UTC-synchronization accuracy at WWVB time source can be as high as 35ns, the WWVB receivers installed in various locations will experience various degrees of path delays determined by its distance from the WWVB time source in Fort Collins, Colorado. As a consequence, considering WWVB signal transmission system delay and path delay, the overall time-synchronization uncertainty can be as large as approximately 30ms [19], which is around 1.5 nominal power cycles. As a result, the uncertainty level of WWVB time dissemination is unacceptable for the various end-use applications, such as determination of phasor angle separation.

In comparison, GPS time is disseminated by a satellite constellation system consisting of 31 dedicated GPS satellites. Each satellite carries an atomic clock that ticks with a nominal accuracy of 1ns. In most locations on earth, at least four GPS satellites are visible, and the GPS time is accurate to 14ns w.r.t. UTC. Regardless, due to the delay associated with the interpretation of GPS signal, GPS clock receivers are accurate to 100ns. By far, GPS is the most accessible, accurate, and affordable option for the dissemination of timing information over a wide geographical area.

3.3 Data Window and Window Functions

Phasor parameters are estimated by applying signal processing techniques to a section of power system waveform samples, which is commonly referred to as a "data window". The way of acquiring such data window is by "truncating" the original waveform with a window function.

Another purpose of the window function is to attenuate undesired components in input signals while retaining as much the energy of the desired signal component, in this case, f_{in} component. The unwanted components in a signal may include DC components, harmonic components, and noise.

Papers [22]-[23] provides an extensive analysis on the window functions and their impact on DFT algorithm performance. A selection of the most commonly used window functions are illustrated in Figure 4.

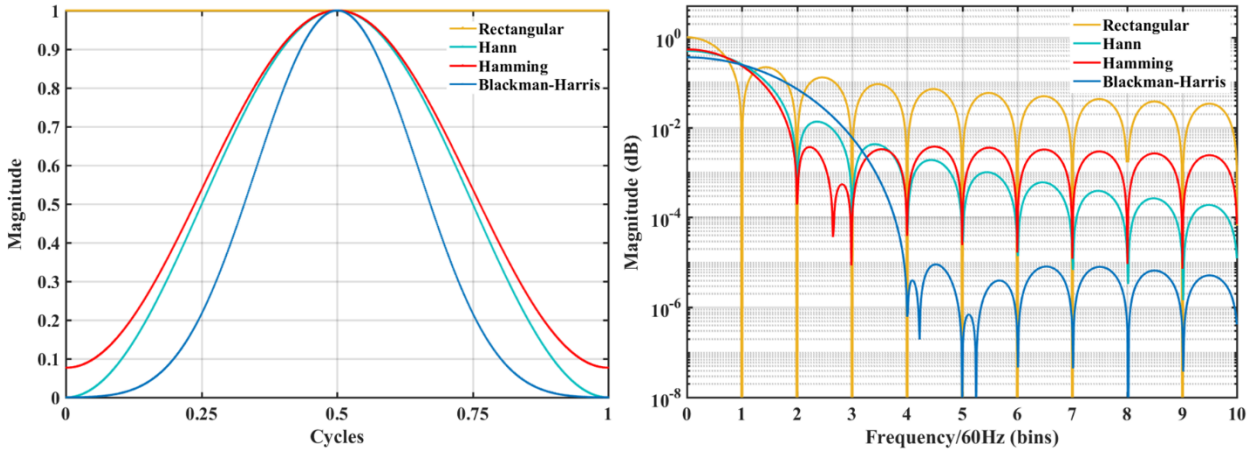

Figure 4 Commonly used window functions and their spectra

The performance metrics of a window function are its mainlobe width and sidelobe attenuation level. The mainlobe width is associated with FIR filter passband smoothness, and the sidelobe attenuation concerns the stopband attenuation. Moreover, when greater sidelobe suppression

is preferred, data window length has to be multiplied so that mainlobe width can be compressed. This affects the sharpness of passband edge, i.e., the width of transition from passband to stop-band. For instance, to achieve the same mainlobe width of 1 DFT bin, for Hann and Hamming windows, a two-cycle data window is needed; for Blackman-Harris window, a four-cycle data window is required, as shown in Figure 5. It can also be observed that, as the length of window function increases, the edge of the mainlobe becomes sharper.

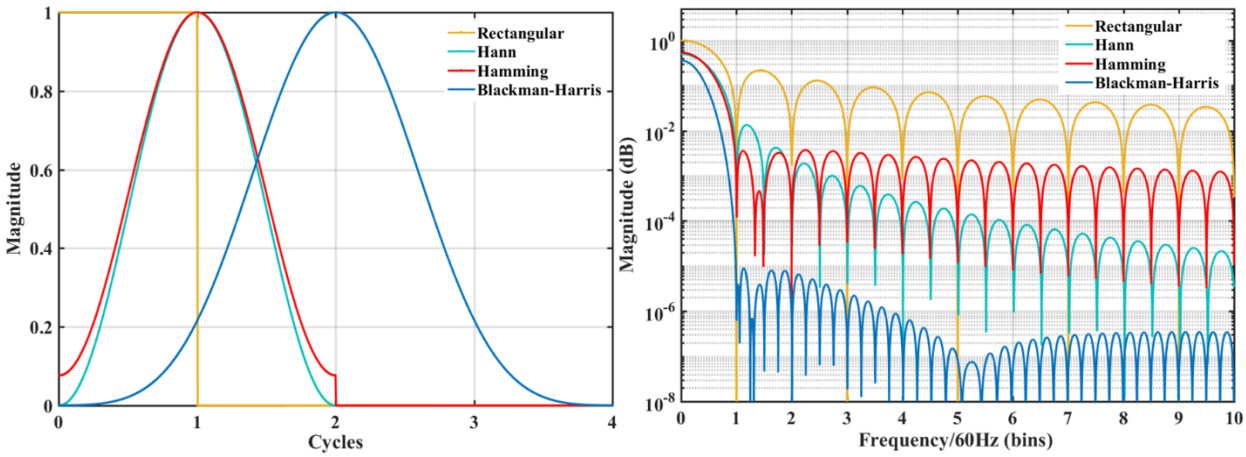

Figure 5 Window functions with window lengths adjusted and the resultant spectra

In the context of power system, the implication of using long data windows is twofold: (i). More waveform samples are needed to produce a phasor parameter, and this leads to phasor data reporting delay; (ii). Changes in waveform features, such as abrupt amplitude changes in the waveforms during faults, are attenuated or smoothed out, and this may lead to mischaracterization of extreme dynamic events. There is no standardization on the choice of window functions in phasor parameter calculation. Documents [9], [10] and [17] offer recommendations on the design of window functions.

3.4 Phasor Parameter Calculation Algorithms for Electromagnetic Dynamic Events

To adequately capture and characterize electromagnetic dynamic events, a fast computational speed is desirable. Due to their fast computational speed and easy implementation, DFT and FFT-based phasor parameter calculation algorithms are widely studied in prior work. In this section of the survey, we focus on the fundamentals of DFT, and a widely used DFT-based algorithm, known as the Interpolated DFT (IpDFT).

3.4.1 Fundamentals of Discrete Fourier Transform

DFT and FFT interpret a section of sampled waveform with a discrete frequency profile representation. The definition of DFT is shown as [24]-[25]:

$$X(k) = \frac{\sqrt{2}}{N}\sum_{n=0}^{N-1} x(n)e^{-\mathrm{j}\frac{2\pi k}{N}n}, k = 0,1,2 \dots, \left\lceil\frac{N}{2}\right\rceil - 1 \tag{3.1}$$

where $X(k)$ is the k-th harmonic phasor component, N is the total number of samples in a data window.

The frequency resolution of DFT is determined by $2\pi/N$ (rad), which is derived from,

$$2\pi\left(\frac{1}{T}\right)\frac{1}{f_s} \equiv \frac{2\pi}{N}$$

where f_s is the sampling frequency, and T is the data window length.

The DFT definition in Equation (3.1) is essentially a trigonometric interpolation calculation [26], and this can also be observed in inverse DFT (IDFT).

$$x(n) = \frac{1}{\sqrt{2}}\sum_{k=-\left\lfloor\frac{N}{2}\right\rfloor}^{\left\lceil\frac{N}{2}\right\rceil-1} X(k)e^{\mathrm{j}\frac{2\pi k}{N}n}, n = 0,1, \dots, N-1 \tag{3.2}$$

where $X(k)$ is the k-th harmonic phasor component, and N is the total number of samples in a data window.

Equation (3.2) is an expression for signal synthesis, where the synthesized signal $x(n)$ is the linear combination of N harmonic components. Each complex signal $e^{j\frac{2\pi k}{N}n}$ is weighted by the corresponding DFT coefficient $X(k)$. In DFT signal modeling, it is assumed that all the frequency components are steady-state sinusoidal signals, whose frequencies fall exactly on k/T (Hz), $k = 0,1,\dots,N-1$.

3.4.2 Calculation of Fundamental Frequency Phasors

The most commonly used approach is the "Interpolated DFT" (IpDFT) technique. In the IpDFT approach, the fundamental frequency component in the waveform is estimated using the highest three DFT bin values. The location of the peak of DFT amplitude spectrum is estimated, and is taken as the fundamental frequency. Since the spectrum of a sinusoidal signal is highly nonlinear at its peak, local linearization near the peak of the spectrum is applied. Once the fundamental frequency is estimated, the "true" value of fundamental frequency phasor is calculated through compensating for the spectrum leakage due to frequency mismatch [27]-[31].

The benefit of IpDFT is that it inherits the computational and implementation efficiency of DFT. The caveat of IpDFT is that, in complex plain, the peak of a DFT spectrum does not necessarily correspond to the actual signal fundamental frequency [32]. This can be observed in Figure 6. The red and blue dashed curves represent the positive and negative spectra of rectangular function (i.e., the "asinc" function) displaced by the actual signal frequency. The black solid line represents the continuous DTFT of the signal, and the DFT are DTFT sampled at DFT bin frequencies, denoted by black dots. Using three DFT samples with largest values, IpDFT can estimate the maxima of DTFT, which clearly deviates from the actual frequency deviation.

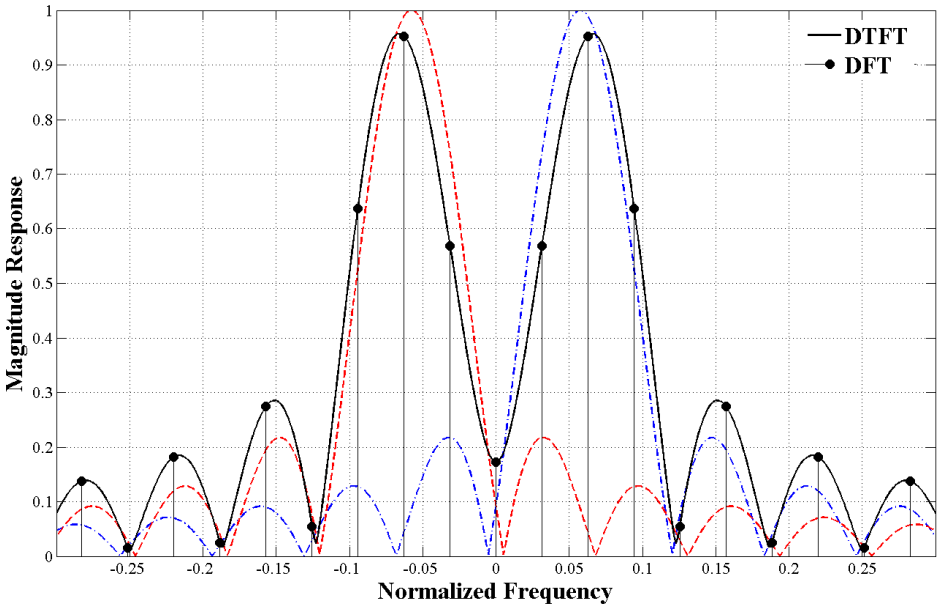

Figure 6 DTFT and DFT spectra of a single-tone sinusoidal input

3.5 Phasor Parameter Calculation Algorithms for Electromechanical Dynamic Events

During electromechanical dynamic events, electrical quantities appear to be slowly unfolding. Calculated phasor parameters should reflect this slow-evolving feature in the waveform in the signal modeling. The most commonly adopted approach for modeling slow-varying phenomena is by using polynomial curve-fitting [34]-[40].

In this method, the input signal is modeled as:

$$\begin{aligned} x(t) &= a(t)\cos[2\pi f_0 t + \phi(t)] \\ &= a(t)\cos\phi(t)\cos(2\pi f_0 t) - a(t)\sin\phi(t)\sin(2\pi f_0 t) \\ &= \mathbf{Re}[p(t)]\cos(2\pi f_0 t) - \mathbf{Im}[p(t)]\sin(2\pi f_0 t) \end{aligned} \tag{3.3}$$

where $p(t) \triangleq a(t)e^{j\phi(t)} = a(t)\cos\phi(t) + ja(t)\sin\phi(t)$ is the corresponding phasor representation.

$p(t)$ can be expanded at an arbitrary time instant $t = t_c$ using polynomials [40]:

$$p(t) = a(t)\cos\phi(t) + \mathrm{j}a(t)\sin\phi(t) \approx \sum_{i=0}^{n} d_i (t - t_c)^i \tag{3.4}$$

where $$d_i = c_i + \mathrm{j}s_i = \frac{1}{i!}p^{(i)}(t)$$

Using the identities $\mathbf{Re}[p(t)] = [p + \hat{p}]/2$ and $\mathbf{Im}[p(t)] = [p - \hat{p}]/2$, where $\hat{p}$ denotes the complex conjugate of p, both the real and imaginary parts of $p(t)$ can be expanded using polynomials:

$$\mathbf{Re}[p(t)] = a(t)\cos\phi(t) \approx \frac{1}{2}\left[\sum_{i=0}^{n} d_i (t - t_c)^i + \sum_{i=0}^{n} \mathrm{conj}(d_i) \cdot (t - t_c)^i\right] \tag{3.5}$$

$$\mathbf{Im}[p(t)] = a(t)\sin\phi(t) \approx \frac{1}{2}\left[\sum_{i=0}^{n} d_i (t - t_c)^i - \sum_{i=0}^{n} \mathrm{conj}(d_i) \cdot (t - t_c)^i\right] \tag{3.6}$$

It may be further simplified as:

$$\mathbf{Re}[p(t)] \approx \sum_{i=0}^{n} c_i (t - t_c)^i \stackrel{\text{def}}{=} q(t) \tag{3.7}$$

$$\mathbf{Im}[p(t)] \approx \sum_{i=0}^{n} s_i (t - t_c)^i \stackrel{\text{def}}{=} r(t) \tag{3.8}$$

And therefore:

$$x(t) = q(t)\cos(2\pi f_0 t) - r(t)\sin(2\pi f_0 t) \tag{3.9}$$

Linear curve-fitting and regression techniques, e.g., least square method [34]-[39], can be used to calculate parameters c_i and s_i. From Equations (3.4)-(3.9), it can be further derived that:

$$\phi(t) = \arctan\left[-\frac{r(t)}{q(t)}\right], f(t) = \frac{\mathrm{d}}{\mathrm{d}t}\phi(t) \tag{3.10}$$

The curve-fitting based algorithms are able to accurately approximate the slow-varying phenomena in signal amplitude and phase angle. However, fast changing phenomena, such as abrupt voltage drops commonly observed in faults, are not reflected in such signal modeling. Consequently, curve-fitting based algorithms in such cases result in large calculation errors with the presence of harmonics, abrupt changes, and noise in input signal. Furthermore, the choice of polynomial order may cause issues. As demonstrated in [41] and [42], increasing the order may improve calculation to an extent, but over-fitting problem occurs when the polynomial order is excessively high so that the algorithm model begin to fit noise components. The order of polynomial should be determined empirically, and in most literature, is set to quadratic terms [36],[38], [42].

3.6 Fundamental Frequency Estimation Methods

The frequency of the power grid is essentially established by the rotating speed of synchronous machine rotors. During normal operation, the synchronous machines in an interconnected power grid operate at slightly different speeds yet around nominal frequency. Under dynamic conditions, there can be significant rotating speed mismatch among the machine rotors in the power grid. In both scenarios, the waveform measured by a substation transducer/PMU is the superposition of the sinusoidal signals with different frequencies. This superposition results in an apparent modulation on amplitude and frequency of the signal [25].

Frequency is a well-defined intrinsic feature of a sinusoidal signal [43]-[45]. For example, in paper [43], instantaneous frequency is defined as:

$$f(t) = \frac{1}{2\pi}\frac{\mathrm{d}}{\mathrm{d}t}[2\pi f_0 t + \phi(t)] = \frac{1}{2\pi}\frac{\mathrm{d}}{\mathrm{d}t}\arg\left[x(t) + \mathrm{j}\mathcal{H}[x(t)]\right] \qquad (3.11)$$

where $x(t)$ follows the definition in Equation (3.3), $\mathcal{H}(*)$ is the Hilbert Transform [46], and $\arg(*)$ denotes the argument of a sinusoidal signal.

As pointed out by [43], the definition shown as Equation (3.11) is problematic when the input signal is not mono-component. Since harmonic components are prevalent in power system signals, the calculation of instantaneous frequency using Equation (3.11) incurs large error. Furthermore, during extreme dynamic conditions, abrupt changes in waveforms and phase angles result in extremely large values in frequencies calculated by Equation (3.11) [32],[47], which is not reasonable since frequency in the power system reflects rotor speed [48]-[49], and is strictly controlled within a narrow range.

The other prevalent approach is to estimate frequency parameter as a signal parameter, embedded in cosine or sine functions [32],[50]-[52]. For example, frequency may be considered as one of the state variables, such as in Kalman filter-based approaches [51], and recursively calculatedly. Nevertheless, solving for an embedded parameter in a nonlinear model can be time-consuming and may cause convergence issues.

3.7 Conclusion

In this Chapter, prior work of phasor parameter calculation algorithms is surveyed. Phasor parameters are associated with the characteristics of sinusoidal signals, i.e., amplitude, phase angle, and frequency. To reflect the features of waveforms, various signal modeling strategies are proposed, leading to algorithms such as IpDFT, polynomial curve fitting, and Kalman filter-based methods. It is observed that each algorithm is designed to match the signal properties manifested in the corresponding dynamic events. As a result, if an algorithm is specifically designed to match its signal modeling with one type of event waveform, high accuracy is expected for that type of event.

It is also known that the signal properties vary among different types of dynamic events. Consequently, an algorithm based on the waveform modeling associated with a single event inevitably leads to algorithm inaccuracy for other types of events, due to the signal modeling mismatch. For instance, DFT-based algorithms cannot adequately track the slow-varying nature of electrical quantities commonly observed in electromechanical dynamic event waveforms, and polynomial fitting algorithms cannot effectively mitigate the waveform distortions caused by harmonic and noise components, as commonly seen in electromagnetic dynamic event waveforms.

Summarizing prior work, a phasor parameter calculation approach that can maintain adequate accuracy for various dynamic scenarios is needed. This improved algorithmic approach needs to incorporate different signal modeling corresponding to different types of dynamic events, and this approach is further discussed in the next Chapter.

4. PROBLEM STATEMENT

4.1 Introduction

In this Chapter, the focus of the Dissertation is first addressed. Then, the hypothesis leading to a solution to the problem is proposed. The hypothesis validation approach is then described. Expected outcomes of the Dissertation work and the organization of this Dissertation are also outlined.

4.2 Focus of This Dissertation

This Dissertation is focusing on developing a new approach that accurately captures the signal waveform features of the extreme dynamic events in the electric power system. This is done by applying signal processing techniques to extract the properties of the event waveforms, specifically, in terms of phasor parameters.

With the new approach, phasor parameter calculation is expected to be accurate for all kinds of dynamic waveforms, which cannot be achieved by other surveyed techniques. Moreover, care will be taken to satisfy both the accuracy and computational time requirements of different control applications. Finally, the hypothesis validation through algorithm testing and result analysis is discussed.

4.3 Hypothesis

It is proposed that a new phasor parameter calculation algorithm should be designed so that phasor parameters can be characterized with adequate accuracy and speed for a variety of control applications. In order to achieve this, it is hypothesized that both the phasor parameter definitions and phasor calculation algorithms should be tailored and optimized according to the type of input signal and associated waveform features. To elaborate,

(1) The definition of phasor parameters in various dynamic operating conditions should match the features of power system waveforms associated with various dynamic events;

(2) The hypothesis is that if multiple signal models are adopted in the algorithm, each signal model can be tailored to match the corresponding waveform associated with a dynamic event. In order to achieve this, the type of dynamic event should be identified first. It is proposed that features of waveforms should be analyzed and leveraged to classify various types of dynamic signal models;

(3) In order to accurately determine the phase angle values at different locations in the power system, synchronized waveform sampling technique should be adopted.

4.4 Hypothesis Validation Approach

The hypothesis validation is conducted via algorithm testing. To achieve this, (i). Adequate PMU algorithm should be designed and implemented; (ii). Novel test procedures, methodologies and metrics should be defined, and test results should be analyzed. The approach is outlined as follows:

(1) Investigate the mechanisms of power system dynamic events, and characterize their waveform manifestations in terms of mathematical formulations. This is discussed in Chapter 5;

(2) Develop a phasor calculation algorithmic framework that is accurate and computationally efficient under both electromagnetic and electromechanical dynamic events. This framework is able to distinguish electromagnetic transients from electromechanical dynamics, and adaptively apply the most suitable PMU algorithm to measure their features. This is discussed in Chapter 6;

(3) Develop a phasor parameter calculation approach for electromagnetic transients. The proposed approach should satisfy the P-class PMU requirements [10] and support the performance of applications design for electromagnetic transient mitigation, such as fault location application. This is discussed in Chapter 7;

(4) Develop a phasor parameter calculation approach for electromechanical dynamics. The proposed approach should satisfy the M-class PMU requirements [10] and ensure the performance of applications design for electromechanical dynamics mitigation, such as oscillation detection application. This is discussed in Chapter 8;

(5) Two types of algorithm testing should be conducted. The algorithm should be evaluated against relevant IEEE/IEC standard [10] in the design test use cases. Then, the hypothesis should be validated in the application test use cases, where the impact of algorithm inaccuracy and communication channel distortion on application performance is demonstrated. In order to do so, application test use cases, comparison metrics, and comparison methodologies are specified. Hypothesis validation strategy and test results are elaborated in Chapter 9.

4.5 Expected Outcomes

The expected outcomes of this Dissertation work are:

(1) *Design a new phasor parameter calculation algorithm*. The distinctive attribute of the new algorithm is that the algorithmic framework enables event waveform classification, and adaptive signal model tuning capability. By doing so, the most apt signal modeling approach is applied for the identified dynamic event;

(2) *Hypothesis is validated under the design test use cases*. Under the design test use cases specified in [10], the proposed algorithm is able to achieve higher accuracy than the surveyed algorithms;

(3) *Hypothesis is validated under the application test use cases*. The test protocol, test methodology, and test metrics of application test use cases are specified. Selected control applications show better performance when using the phasors calculated by the proposed algorithm, than the phasors calculated by the reference algorithms.

4.6 Organization of the Dissertation

The rest of the Dissertation is organized as follows. A discussion on the extreme power system events and their waveform manifestations is conducted in Chapter 5. The framework of the proposed algorithmic tools and their interactions is discussed in Chapter 6. In Chapter 7, a phasor parameter calculation method for electromagnetic transients is proposed. Chapter 8 proposes a phasor parameter calculation approach for electromechanical transients. The performance of proposed approach is evaluated and demonstrated, and the results are discussed in Chapter 9. Conclusions and future works are outlined in Chapter 10. References and Appendices are attached at the end.

4.7 Conclusion

In this Chapter, Dissertation hypothesis, hypothesis validation approach, and expected outcomes are discussed. It is concluded that in order to compute phasor parameters with adequate accuracy and speed, phasor parameter definition and phasor parameter calculation should be tailored to the input waveform features. To validate the hypothesis, it is proposed that: (i). Features of input dynamic waveforms should be studied to differentiate different dynamic properties of the waveforms; (ii). A phasor parameter calculation algorithm should be designed and

implemented to accommodate the distinct waveform features; and (iii). The proposed algorithm should be validated in both design and application tests. These topics are elaborated in Chapters 5 to 9. Expected outcomes and the organization of the Dissertation are also outlined.

5. UNDERSTANDING THE DYNAMIC EVENTS IN THE POWER SYSTEM AND THEIR WAVEFORM MANIFESTATIONS

5.1 Introduction

The power system is composed of electrical and mechanical components such as transmission lines (conductors), insulators, power electronics devices, and rotating masses (machine rotors). The physical arrangements and connections of these physical components, as well as their interaction through magnetic and electrical fields, ultimately determines the electrical and mechanical phenomena observed in the power systems.

It is common to analyze the power system in terms of circuit components. In order to do so, physical components, as well as the connection among the components, are modeled using ideal resistance (R), inductance (L), and capacitance (C) elements. As a result of this modeling, power system phenomena are represented by the electrical quantities and mathematical formulations in which properties of electrical quantities are embedded. In this Dissertation, the power system will be studied based on the RLC circuit (stationary or rotating) modeling.

5.2 Classification of Power System Dynamic Conditions

The electric power systems are continuously regulated and coordinated, both on a local/wide-area scale [53], and in short-term/long-term sense [54]-[55]. Since electric power energy cannot be stored in large amount in the power grid, there is a tendency for the electric power system to transition to an operating condition where the electric power generation meets the load consumption. Ideally, the balance between power generation and power consumption is maintained in a “dynamic equilibrium”, where power generation dynamically “tracks” the

changes in load demand, and reduces the discrepancy between power generation and consumption. This operating condition is considered as the "normal" or steady-state operating condition.

The electric power system is subject to sustained disruptions, characterized by different levels of severity. Minor disruptions are characterized by their randomness, as well as the negligible changes to the existing operating condition. For example, the perturbations caused by environmental conditions such as wind and temperature, within a limit, do not consequentially disrupt the balance between power generation and power consumption.

Major disruptions, on the other hand, are characterized by sudden and unexpected mismatches between power generation and load demand. Major disruptions cannot be smoothly mitigated without incurring large fluctuations in electrical quantities, such as voltage levels, current flows, and frequencies [56]. During the transition of power system to another power equilibrium state, extreme dynamic events may be experienced. Major disruptions can be caused by sudden changes in power supply/consumption (e.g., loss of generation/load), sudden changes in power network topologies (e.g., opening/reclosing of circuit breakers), insulation breakdowns (e.g., faults and isolation of faulted components), or lack of damping in the power system (e.g., growing oscillations). Following a major disruption in the power system, the extreme dynamic events may be classified as electromagnetic and electromechanical dynamic events [57]-[59].

5.2.1 Decoupling of Electromagnetic and Electromechanical Dynamic Transients

Following a disturbance, such as faults, fluctuations in electrical quantities and rotor mechanical characteristics, can be observed. Strictly speaking, the ensuing fluctuations in electrical and mechanical quantities unfold simultaneously. In this Dissertation, however, the dynamic transients are decoupled into electromagnetic and electromechanical dynamics, and this is justified because of the following reasons:

(1) *The essential components driving the dynamics are different.* Electromagnetic and electromechanical dynamic events are manifested through different component interactions in the power grid. Specifically, electromagnetic dynamics are solely manifested through RLC circuit components, and electromechanical dynamics are manifested through both the movable mechanical elements of the power grid (i.e., rotors), and the RLC circuit (e.g., rotor and armature windings, transformer windings, and electric power network). The underlying "participants" in electromagnetic and electromechanical dynamic phenomena fundamentally indicate that these two dynamic phenomena should be modeled differently;

(2) *Purpose of observing the fast vs. slow dynamic events is different.* Besides harmonic and noise components, electromagnetic transients during faults are associated with dangerously high fault current. And therefore, they should be identified and isolated with minimum delay. The observation on electromechanical transients, on the other hand, is performed in the context of tracking electrical quantities under non-emergency operating conditions, where there may be no imminent harm to the power grid. This distinction also determines that electromagnetic and electromechanical dynamic events should be characterized separately;

(3) *The time constants of electromagnetic and electromechanical dynamic events, as well as the time constraints associated with the corresponding control applications are different.* The time needed for the transient electrical quantities, such as fault current, to decay to the level of $e^{-1} \approx 36.8\%$ w.r.t. $t = 0$ [60]-[61] is used to measure the damping effect during a dynamic phenomenon. In the power system, the damping capability is determined by the RLC parameters, the configuration of the circuit (e.g., damper windings on

the rotors), and the rotor inertia. As illustrated in [60]-[62], the sub-transient quantities have the time constant within 3 cycles, and transient quantities damp out within 2 seconds, and stator transients take even longer time to decay. Since protective relays operate in a few nominal cycles or less, given the large inertia of rotors, the rotor mechanical features can be considered to maintain their pre-contingency conditions.

To summarize, due to the nature of extreme dynamic events, and the time constraints of subsequent mitigation applications, electromagnetic and electromechanical dynamic events can be decoupled and studied individually.

5.2.2 Electromagnetic Dynamic Events

Electromagnetic transients are caused by sudden disruptions of electric circuits, which may be initiated by faults, lightning strikes, or opening/closing circuit breakers [56]. Electromagnetic transients cause fast changes in voltage and current magnitudes. The dramatic changes in current magnitude in a short period of time are characterized by a rich profile of decaying DC component and harmonic components, which range from kHz to MHz [25]. The transient voltage sag caused by faults in its vicinity may lead to electric motor stalling, which results in machine overheating. The transient overcurrent creates a tremendous amount of heat, which may stress insulation and switchgear, cause fire, and create safety hazard to the field workers and nearby residents. Therefore, the causes of extreme electromagnetic transients need to be mitigated and/or isolated with minimal delay.

5.2.3 Electromechanical Dynamic Events

Unlike electromagnetic dynamic events, electromechanical dynamic events are caused by the relative movements of machine rotors and their impact on electrical quantities associated with the power grid. The interaction between an electric machine rotors and the grid is enabled

by the magnetic coupling between the rotating rotor RLC circuit and the stationary power network RLC circuit. The movement of a machine rotor is initiated by an imbalance between mechanical and electrical torques exerted on the rotor, which may be provoked by sudden changes in electrical power output, such as loss of load; or abrupt changes in mechanical input, such as prime mover stalling [63].

Once the relative movements of machine rotors begin to unfold, the equivalent circuit of the power network from the perspective of each machine changes as well, resulting in changes in electrical torque output. The interactions between electric power network and machine rotors result in modulations on electrical quantities, which may last for as long as tens of seconds [64]. In the extreme scenarios, electromechanical transients can cause rotor angle instability, such as loss of synchronism of rotors and growing oscillations of electrical quantities. Without adequate mitigation strategy, electromechanical oscillations will impede power transfer, provoke voltage instability, and may eventually lead to blackouts in both local and large areas [64].

5.3 Waveform Manifestations of Power System Dynamic Events

5.3.1 Generic Waveform Formulation

Power system waveforms are sinusoidal signals, which can be expressed as:

$$x(t) = a(t) \cdot \cos[\phi(t)], t = k\Delta t \tag{5.1}$$

and,

$$\phi(t) = 2\pi \int_0^t f(\tau)\mathrm{d}\tau + \phi_0 \tag{5.2}$$

where $a(t)$ is amplitude, $\phi(t)$ is phase angle w.r.t. $t = 0$, Δt is sampling interval, ϕ_0 is the initial phase angle at $t = 0$, $f(t)$ is frequency in Hz.

In Equation (5.2), phase angle $\phi(t)$ is defined as the argument of cosine function. Alternatively, phase angle may be defined as an offset.

$$\phi(t) = 2\pi f_0 t + \phi_s(t)$$

and, $$\phi_s(t) = 2\pi \int_0^t \Delta f(\tau)\mathrm{d}\tau + \phi_0 \tag{5.3}$$

where f_0 is the nominal frequency. In this definition, phase angle is interpreted as the angle offset w.r.t. a nominal frequency cosine signal. This phase angle definition is adopted in the IEEE synchrophasor standards [10].

In a steady-state operating condition, power system waveforms are characterized with constant values of $a(t)$ and $f(t)$. In the dynamic scenarios, the amplitude and frequency are constantly modulated due to electromagnetic and electromechanical transients. This will be discussed in detail in the following subsections.

5.3.2 Waveform Manifestation of Electromagnetic Dynamic Events

The most commonly encountered electromagnetic dynamic event is fault, which is essentially shorting an energized circuit. A circuit is shorted when an unintended breakdown of insulation occurs, allowing immense current to flow through the connection. According to the discussion in Section 5.2.1, when characterizing the features of electromagnetic transient waveforms, it is assumed that the rotor speeds remain the same for the first few cycles after the fault, and therefore, the power system fundamental frequency maintains the pre-contingency values. As derived in Appendix B, also elaborated in [65], the formulation of fault current can be expressed as:

$$\begin{aligned} i_f(t) = {} & \frac{A_1}{Z_1}\cos(\omega t + \phi_1 - \theta_1) \\ & + e^{-at}\left[\frac{E_d{}'}{bL}\sinh(bt) - \frac{A_1}{Z_1}\cos(\phi_1 - \theta_1)\cosh(bt)\right], \text{i. f. f.} \frac{R^2}{4L^2} > \frac{1}{LC} \end{aligned} \tag{5.4}$$

where, $$a = \frac{R}{2L}, b = \sqrt{\frac{R^2}{4L^2} - \frac{1}{LC}}$$

$$i_f(t) = \frac{A_1}{Z_1}\cos(\omega t + \phi_1 - \theta_1)$$
$$+e^{-at}\left\{\frac{E_d{}'}{\beta L}\sin(\beta t) - \frac{A_1}{Z_1}\cos(\phi_1 - \theta_1)\cos(\beta t)\right\}, \text{i. f. f.} \frac{R^2}{4L^2} < \frac{1}{LC} \quad (5.5)$$

where, $$\alpha = \frac{R}{2L}, b = \mathrm{j}\beta, \beta = \sqrt{-\frac{R^2}{4L^2} + \frac{1}{LC}}$$

Note that the exact expression of fault current depends on the RLC values of a circuit, which determine the values of constant in Equations (5.4) and (5.5). In a transmission system, $R/(2L) < 1/\sqrt{LC}$ typically holds true. As a result, fault current is in the form of steady-state fault current superimposed by decaying DC and high-frequency harmonic components.

5.3.3 Waveform Manifestation of Electromechanical Dynamic Events

Electromechanical dynamic events are associated with the effects of rotor movements on electrical quantities. The magnetic coupling between the rotating rotor RLC circuit and the stationary stator RLC circuit (which is connected to the power network) is established through sharing the magnetic field air gap. The time scale under study is sufficiently long so that the impact of the relative movement of rotors cannot be ignored. The changes in the values of rotor angle separation affect the electric power transfer of the power network. As indicated by the swing equation [59], the change on the electrical output on a rotor will eventually affect the mechanical behaviors of the rotor, resulting in a slow unfolding dynamic event. As discussed in Section

5.2.1, in the analysis of electromechanical dynamics, it is assumed that electromagnetic transients have sufficiently dissipated, so that abrupt changes in electrical quantities will not be encountered.

By mathematical analysis, the electrical torque exerted on a rotor can be decomposed into two quadrature components: synchronizing torque and damping torque [66]. A lack of synchronizing torque leads to aperiodic loss-of-synchronism, and a lack of damping torque causes growing oscillations. These two phenomena are discussed below.

5.3.2.1 Waveforms of Loss-of-Synchronism Dynamics

After a major disturbance, a synchronous machine may lose synchronism with the rest of the system when the deceleration area is smaller than the acceleration area [59]. This happens when there is not sufficient synchronizing torque on the rotor.

In the case of loss-of-synchronism, rotor speed slowly drifts from a constant value, which can be formulated as:

$$\omega(t) = \omega_0 + 2\pi \int \left(\frac{\mathrm{d}\Delta f}{\mathrm{d}t}\right) \mathrm{d}t \tag{5.6}$$

where ω_0 is the initial frequency. In a short phasor parameter calculation window, it is assumed that rotor speed is piecewise linear. Quantity $R_f(t) \equiv \mathrm{d}\Delta f/\mathrm{d}t$ (in Hz/s) is defined to characterize the rate-of-change-of-frequency, which is a constant in each calculation window.

To summarize, the waveform manifestation in the loss-of-synchronism case can be formulated as:

$$x(t) = a(t) \cdot \cos\left[2\pi f t + \pi R_f(t) t^2 + \phi_0\right] \tag{5.7}$$

5.3.2.2 Waveforms of Oscillatory Dynamic Phenomena

The oscillation phenomena are related to the small signal stability of a synchronous machine. After a perturbation, the rotor may oscillate against the rest of the system, resulting in oscillatory modulations on electrical quantities. With insufficient damping torque, the oscillation may grow and eventually cause loss-of-synchronism. In a short phasor calculation window, it is assumed that the oscillation is a critical oscillation (does not grow or subside). This phenomena can be captured by the following representation of the waveform:

$$x(t) = [1 + k_{\mathrm{AM}}\cos(2\pi f_m t + \phi_{\mathrm{AM}})] \cdot A \cdot \cos[2\pi f_0 t + k_{\mathrm{FM}}\cos(2\pi f_m t + \phi_{\mathrm{FM}}) + \phi_0] \tag{5.8}$$

where parameters with subscript AM represent modulations on amplitude, parameters with subscript FM represent modulations on frequency; k_{AM} and k_{FM} are the modulation levels for AM and FM cases, respectively; ϕ_0 is the modulation initial phase angle, f_m is the modulation frequency.

An amplitude-modulated signal, shown in Equation (5.9), it can be shown that the waveform consists of three single-tone sinusoidal signals:

$$\begin{aligned} x(t) &= [1 + k_{\mathrm{AM}}\cos(2\pi f_m t + \phi_{\mathrm{AM}})] \cdot A \cdot \cos[2\pi f_0 t + \phi_0] \\ &= A \cdot \cos[2\pi f_0 t + \phi_0] + \frac{k_{\mathrm{AM}}A}{2}\cos[2\pi(f_0 - f_m)t + (\phi_0 - \phi_{\mathrm{AM}})] \\ &\quad + \frac{k_{\mathrm{AM}}A}{2}\cos[2\pi(f_0 + f_m)t + (\phi_0 + \phi_{\mathrm{AM}})] \end{aligned} \tag{5.9}$$

Similarly, a frequency-modulated signal can be shown to be the superposition of an infinite series of single-tone sinusoids, shown in Equation (5.10). Detailed derivation of Equation (5.10) is shown in Appendix C as Equation (C3.7).

$$x(t) = \cos(2\pi f_0 t + \phi_0) \cdot J_0(k_m)$$
$$+ \sum_{k=0,2,4,\ldots}^{\infty} (-1)^{\frac{k}{2}} J_k(k_m)\{\cos[2\pi(f_0 - kf_m)t + \phi_0 - \phi_m]$$
$$+ \cos[2\pi(f_0 + kf_m)t + \phi_0 + \phi_m]\} \quad (5.10)$$
$$- \sum_{k=1,3,5,\ldots}^{\infty} (-1)^{\frac{k-1}{2}} J_k(k_m)\{\sin[2\pi(f_0 - kf_m)t + \phi_0 - \phi_m]$$
$$+ \sin[2\pi(f_0 + kf_m)t + \phi_0 + \phi_m]\}$$

It is important to differentiate the frequency profile representations of amplitude and frequency modulated waveforms, shown in Equations (5.9) and (5.10), from the Fourier representation of these two types of dynamic input signal. Both representations perceive the input signal in terms of the superposition of harmonic components. Nevertheless, FFT reconstructs input signal in terms of a predetermined fundamental frequency (i.e., the FFT frequency resolution) and its harmonics; whereas the frequency profile representation portraits the input signal in terms of the *actual* frequency composition. In a few words, the FFT spectral analysis on a piece of AM or FM waveform may not accurately represent the *true* spectral profile of the signal, due to picket fence effect [67]-[68] and spectral leakage phenomenon [67]-[68].

5.4 Conclusion

In this Chapter, the physical nature and waveform manifestation of electromagnetic and electromechanical dynamic phenomena are discussed. It can be summarized that electromagnetic and electromechanical dynamic events are fundamentally different due to the physical processes that drive them, which are subsequently manifested in distinct types of waveforms. Due to this reason, electromagnetic and electromechanical dynamics will be decoupled and studies individu-

ally. The waveform formulation will determine the design of phasor parameter calculation algorithms, particularly the underlying signal modeling, which is elaborated in the following Chapters.

6. FUNDAMENTALS OF THE PROPOSED PHASOR PARAMETER CALCULATION APPROACH [*]

6.1 Introduction

In order to validate the Dissertation hypothesis, a particular algorithmic approach is developed to achieve accurate characterization of the waveform features that represent power system dynamic operating conditions. The approach includes characterizing the dynamic waveforms and defining the corresponding phasor parameters, developing and implementing a PMU algorithm, and demonstrating the accuracy of the proposed PMU algorithm.

6.2 Fundamentals of Time-Synchronized Calculation of Phasor Parameters

Time-synchronized phasors, or synchrophasors, are formally defined in IEEE C37.118-2005 [69]. In phasor representation, a complex number is assigned to the sinusoidal signal as an equivalent representation, where the modulus of the complex number equals the RMS value of the sinusoidal signal, and the argument corresponds to the phase angle of the sinusoidal signal. Frequency is not explicitly expressed in phasor representation, but is rather associated with the rate of change of phase angles.

As defined in IEEE Standard C37.118-2005 [69] and subsequent standards [9]-[11], the phase angle of a synchrophasor is the relative phase angle of the sinusoidal signal w.r.t. a 60Hz sinusoidal signal whose peak is located exactly at a second rollover.

---

[*] Reprinted with authors' permission from C. Qian and M. Kezunovic, "Synchrophasor reference algorithm for PMU Calibration System," *2016 IEEE/PES Transmission and Distribution Conference and Exposition (T&D)*, Dallas, TX, pp. 1-5, May 2016. Copyright 2016, IEEE.

A sinusoidal signal is defined in Equation (6.1).

$$\begin{aligned} x(t) &= A \cdot \cos\left[2\pi \int_0^t f(\tau) \cdot \mathrm{d}\tau + \phi_0\right] \\ &= A \cdot \cos\left[2\pi f_0 t + 2\pi \int_0^t \Delta f(\tau) \cdot \mathrm{d}\tau + \phi_0\right] \\ &= A \cdot \cos[2\pi f_0 t + \phi(t)] \\ \phi(t) &= 2\pi \int_0^t \Delta f(\tau) \cdot \mathrm{d}\tau + \phi_0 \end{aligned} \tag{6.1}$$

where ϕ_0 is the initial phase angle, f_0 is the nominal frequency, $f(t)$ is the instantaneous frequency at time t, $\Delta f(t)$ is the frequency deviation at time t. Besides, instantaneous phase angle $\phi(t)$ is defined as the total phase angle displacement w.r.t. signal $A\cos(2\pi f_0 t)$.

Phasor parameters are defined to represent the attributes of sinusoidal signal, i.e., magnitude, phase angle, and frequency, embedded in Equation (6.1). Conventionally, phase angle is defined as the entire argument of the cosine function, i.e., $[2\pi f_0 t + \phi(t)]$. Per this definition, the sinusoidal signal can be recovered by Equation (6.2).

$$\begin{aligned} x(t) &= \mathbf{Re}\left\{\sqrt{2} \cdot p_1(t)\right\} \\ p_1(t) &= \frac{A}{\sqrt{2}} e^{\mathrm{j}(2\pi f_0 t + 2\pi \int_0^t \Delta f(\tau) \cdot \mathrm{d}\tau + \phi_0)} \end{aligned} \tag{6.2}$$

Acknowledging that phase angle is in fact a relative "angle displacement" from an arbitrary angle reference, we may define phase angle as the displacement from a nominal frequency sinusoidal signal. As a result, alternatively, in IEEE standard [10], for synchrophasor applications, phase angle is defined as the instantaneous phase angle $\phi(t)$, as shown in Equation (6.3).

$$x(t) = \mathbf{Re}\left\{\sqrt{2} \cdot p_2(t) \cdot e^{\mathrm{j}(2\pi f_0 t)}\right\}, \text{ where} \tag{6.3}$$

$$p_2(t) = \frac{A}{\sqrt{2}} e^{\mathrm{j}(2\pi \int_0^t \Delta f(\tau)\cdot \mathrm{d}\tau + \phi_0)}$$

Evidently, both phase angle definitions are equivalent in terms of representing the same sinusoidal signal $x(t)$. In this Dissertation, the definition in Equation (6.3) is adopted.

6.3 Proposed Strategy and Tools for Time-Synchronized Phasor Parameter Calculation

The proposed time-synchronized phasor calculation tools aims to improve control application performance to adequately detect and mitigate extreme electromagnetic and electromechanical dynamic events. As discussed in Chapter 2, electromagnetic and electromechanical dynamic events are distinct due to their underlying physical natures, and will be studied separately. In particular, the causes of electromagnetic dynamic events should be mitigated with minimal delay, whereas electromechanical dynamic events should be accurately characterized to allow tracking. Moreover, the phasor parameter calculation should be performed in a time-synchronized fashion to accurately obtain phase angle values.

This Dissertation proposes a framework for time-synchronized phasor parameter calculation, which aims to facilitate the emergency mitigation applications during both extreme electromagnetic and electromechanical dynamic events. The strategy and reasoning are further explained as follows.

6.3.1 Determination of Data Window Function

As discussed Section 3.3, the common use of window functions is to achieve attenuation of harmonic components and noise. It is also highlighted that a window function with sharper passband edge requires longer data window to narrow the mainlobe width.

The choice of window functions has impact on PMU algorithm performance. Synchrophasor estimation inherently represents a notion of data filtering, and therefore, information loss

is inevitable. Such information loss is manifested as the inadequate characterization of changes in electrical quantities and signal parameters in the data window. Specifically, a longer window function would allow more reduction of noise interference, but would also average out more dynamic changes. A non-uniform window function acts as a digital filter and reduces Gibbs effect [23] in Fourier analysis, but will also inevitably cause longer response delay under changing dynamic conditions.

The decision on the characteristics of data window function of a synchrophasor algorithm depends on the end-use applications. For example, a fault should be isolated within 5 cycles [56], considering the operation delay associated with protective relay and circuit breaker, the phasor calculation data window should be within 2 cycles [10]. An excessively long data window would fail to identify any rapid dynamic changes in the waveform which are crucial in detecting and isolating a fault. Conversely, for oscillation detection, an adequately long data window is desired in order to effectively eliminate the impacts from harmonics with filters.

In summary, for electromagnetic transients, to achieve fast computational speed, the data window length should be within 2 cycles. For electromechanical transients, to achieve adequate computational accuracy, the window length may vary depending on the end-use application.

6.3.2 Phasor Parameter Calculation During Electromagnetic Transients

As previously examined, extreme electromagnetic transients, typically provoked by faults, should be characterized with minimal delay. DFT-based methods are by far the most computationally efficient, and therefore, they should be used as the backbone of phasor parameter calculation under rapidly changing electromagnetic conditions.

The major caveat of DFT-based method is spectrum leakage caused by the mismatch between the actual signal spectral profile and DFT signal modeling, which is caused by frequency

deviation, harmonic components, and decaying DC components in the input signal. Thus, it is proposed that DFT bin frequency should be adaptively tuned to align with the actual fundamental frequency of input signal, so that frequency leakage can be minimized. Moreover, signal properties that are not modeled in the existing DFT-based methods, such as the decaying DC components, should be characterized in the proposed algorithm.

The proposed strategy requires the frequency calculation to precede DFT-based phasor calculation. This is based on the reasoning that during the 2 cycles immediately after a fault, it can be assumed that machine rotors do not change their rotating speed due to large inertia. As a result, the frequency of the power system can be assumed to maintain its pre-contingency value.

The schematic of this proposed approach is shown in Figure 7. As shown in Figure 7, Loop (a) is an independently running fundamental frequency estimator, where the most recent frequency estimate is stored. The phasor calculation algorithm, shown as Loop (b), retrieves the latest fundamental frequency value and tunes DFT-based algorithms.

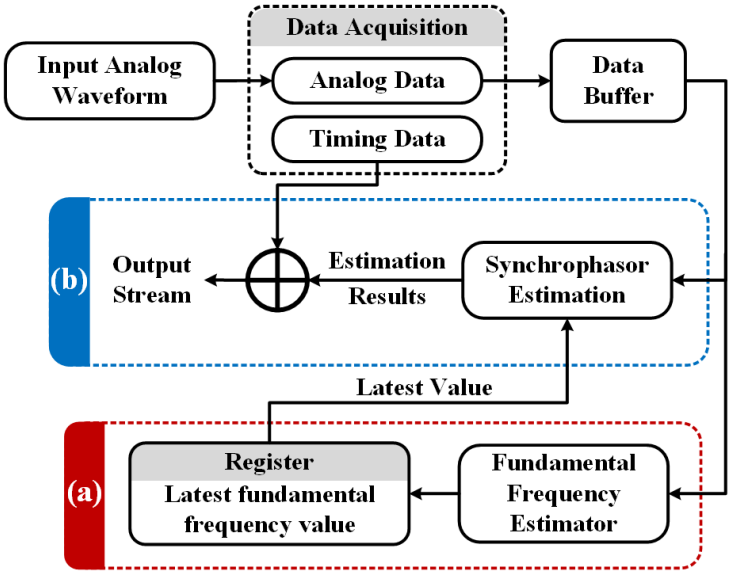

Figure 7 Proposed phasor parameter calculation schemes for electromagnetic dynamic events Loop (a), fundamental frequency estimator; Loop (b), phasor parameter calculation for electromagnetic dynamics. Modified with permission from C. Qian and M. Kezunovic, "A novel time-frequency analysis for power system waveforms based on "pseudo-wavelets"," *2018 IEEE/PES Transmission and Distribution Conference and Exposition (T&D)*, Denver, CO, pp. 1-9, Apr. 2018. Copyright 2018, IEEE

6.3.3 Phasor Parameter Calculation During Electromechanical Transients

Since the trajectories of electrical quantities during electromechanical dynamics are slow-evolving, more time-consuming, computationally demanding techniques may be used. For example, curve-fitting-based algorithms will be used to calculate phasor parameters during electromechanical dynamic events, as these techniques have shown benefits in representing the slow-varying features in signals.

As summarized in Chapter 3, a single algorithm cannot achieve accuracy for all types of electromechanical dynamic event waveforms. This is essentially due to the fact that various electromechanical phenomena are manifested in different signal formulations, and a single algorithm modeling strategy cannot match all types of electromechanical dynamic waveforms. Therefore, a

waveform type classification step is introduced to differentiate various types of electromechanical phenomena, so that the most appropriate algorithm can be adaptively "switched" to perform phasor parameter calculation. A schematic diagram is shown in Figure 8. The proposed strategy for phasor parameter calculation under electromechanical dynamics is realized by incorporating two co-independent loops. Loop (a) and loop (b) run independently, where loop (a) performs waveform classification, and stores the most recent waveform classification result in its memory (e.g., registers); loop (b) performs phasor parameter calculation. In loop (b), an algorithm switching mechanism is deployed. This mechanism adaptively selects the most accurate algorithm according to the identified waveform type, which is stored in the memory.

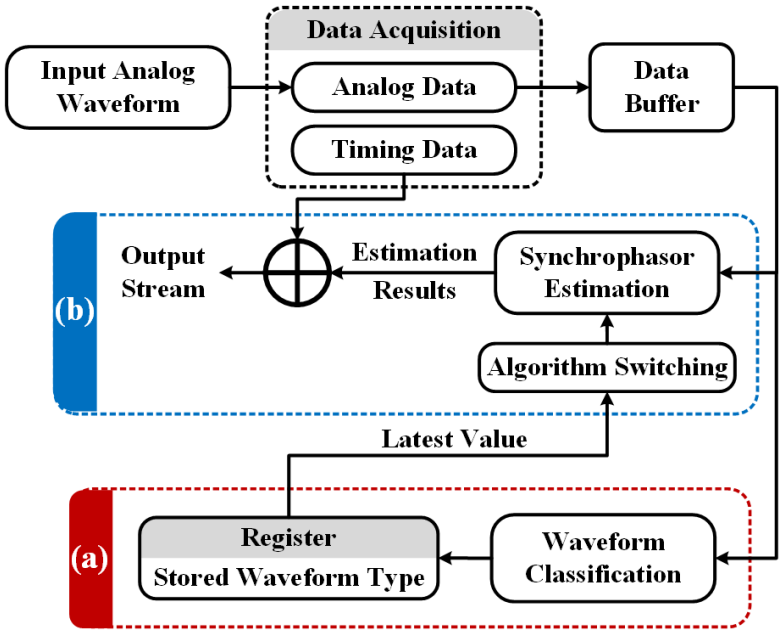

Figure 8 Proposed phasor parameter calculation schemes for electromechanical dynamic events.
Loop (a), waveform classification mechanism; Loop (b), phasor parameter calculation algorithm for electromechanical dynamics. Reprinted with permission from C. Qian and M. Kezunovic, "A novel time-frequency analysis for power system waveforms based on "pseudo-wavelets"," *2018 IEEE/PES Transmission and Distribution Conference and Exposition (T&D)*, Denver, CO, pp. 1-9, Apr. 2018. Copyright 2018, IEEE

6.4 Interaction of the Proposed Tools

Figure 9 shows the framework of how the proposed phasor parameter calculation tools are integrated. The proposed tools serve to facilitate applications that mitigate the causes of extreme electromagnetic and electromechanical dynamic events. The key features of the proposed technique are as follows:

(1) During normal operating condition and electromagnetic events, the algorithm operates in "P-Class PMU mode", where a 2-cycle data window is used for phasor parameter calculation. When the Event Classification tool detects an electromechanical dynamic waveform, the algorithm switches to "M-Class PMU mode", where a multi-cycle data window is used for phasor parameter calculation.

(2) The key modules in the proposed algorithm, which enable the aforementioned "operating mode switching" and accurate phasor parameter calculation in each mode, are the fundamental frequency estimator, and the event/waveform classification tool.

(3) The fundamental frequency estimator tracks the power system fundamental frequency, and stores the latest estimation value. This step is crucial in tuning DFT-based method to alleviate frequency leakage effect. Then, the proposed DFT-based method is used to calculate phasor parameters under electromagnetic transients. A hybridization algorithmic framework is adopted, which reduces the impact of exponentially decaying DC component. The proposed method is tailored to accurately characterize the electromagnetic dynamic waveforms. This way, fast response can be achieved. This technique is elaborated in Chapter 7.

(4) For slowly unfolding electromechanical dynamic events, the event/waveform classification technique are proposed to differentiate waveforms associated with various electromechanical dynamic events. Then, algorithms are proposed to achieve accurate phasor parameter calculation for each type of dynamic waveform. This technique is elaborated in Chapter 8.

(5) The proposed approach fundamentally integrates phasor parameter calculation for both fast and slow dynamic conditions in the power system without sacrificing accuracy for either scenario. The testing strategies and performance evaluation of proposed techniques are discussed in Chapter 9

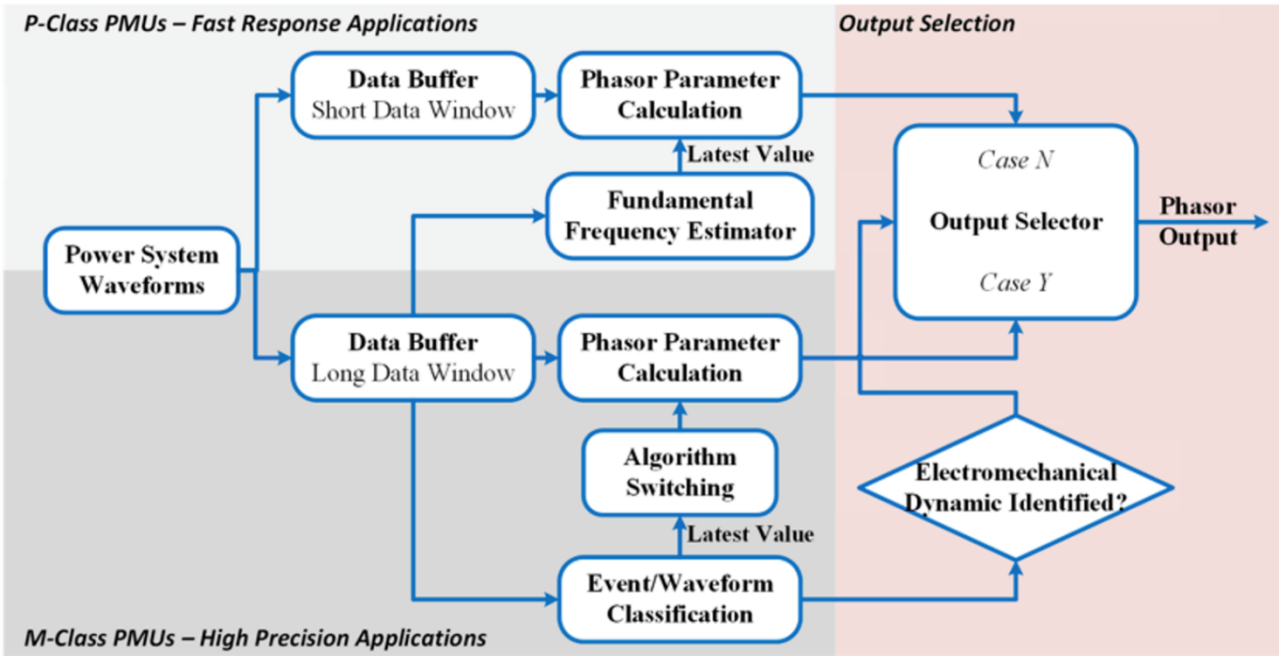

Figure 9 Hierarchical illustration of proposed algorithm design framework

6.5 Conclusion

This Dissertation proposes an algorithmic framework that allows both electromagnetic and electromechanical dynamics in the power system to be effectively characterized in terms of

phasor parameters, which is devised in Section 6.4. In particular, the phasor parameter calculation method for electromagnetic transients is outlined in Section 6.3.2, and the phasor parameter calculation method for electromechanical transients is introduced in Section 6.3.3.

In the following Chapters, the individual tools in the framework will be elaborated, and their accuracy will be tested.

7. POWER SYSTEM FUNDAMENTAL FREQUENCY ESTIMATION APPROACH AND PHASOR PARAMETER CALCULATION DURING ELECTROMAGNETIC TRANSIENTS [*]

7.1 Introduction

The electromagnetic dynamic waveforms are formulated in Section 5.3.2, and they are the subject of further study in this Chapter. To enable fast mitigation actions (protective relaying) against extreme electromagnetic dynamic events (faults), phasor parameters should be calculated within two cycles. In that time frame, the proposed PMU algorithm should mitigate the impact of harmonics, noise, and decaying DC components on phasor calculation accuracy.

In this Chapter, we improve the modeling of DFT-based algorithm to achieve the lowest computational burden while effectively eliminate the influence of decaying DC components. We introduce an adaptive DFT window length adjustment, as well as subsequent spectral compensation mechanisms. This approach mitigates the pitfalls of DFT-based algorithms caused by picket-fence [67]-[68] and frequency leakage phenomenon [67]-[68].

---

[*] Reprinted with authors' permission from: (1) C. Qian and M. Kezunovic, "Dynamic synchrophasor estimation with modified hybrid method," *2016 IEEE Power & Energy Society Innovative Smart Grid Technologies Conference (ISGT)*, Minneapolis, MN, pp. 1-5, Sep. 2016. Copyright 2016, IEEE. (2) C. Qian and M. Kezunovic, "Spectral interpolation for frequency measurement at off-nominal frequencies," *2017 IEEE Power & Energy Society General Meeting*, Chicago, IL, pp. 1-5, Jul. 2017. Copyright 2017, IEEE. (3) C. Qian and M. Kezunovic, "Hybridization framework for improved dynamic phasor parameter estimation algorithms," *2019 IEEE Power & Energy Society Innovative Smart Grid Technologies Conference (ISGT)*, Washington, D.C., pp. 1-5, Feb. 2019. Copyright 2019, IEEE. (4) C. Qian and M. Kezunovic, "Power system fundamental frequency estimation using Unscented Kalman Filter," *2019 IEEE Power & Energy Society General Meeting (PESGM)*, Atlanta, GA, USA, pp. 1-5, Aug. 2019. Copyright 2019, IEEE.

To achieve this strategy, a fundamental frequency tracking method is proposed. Due to the large mechanical inertia, it is reasonable to assume that the rotor speeds maintain their pre-contingency values for 2 cycles after a disturbance, where the phasor parameter calculation takes place. Accordingly, as proposed in Section 6.3.2, the fundamental frequency estimation is executed independently from phasor calculation. In order to reduce the uncertainty caused by measurement noise and to enable fast frequency tracking, UKF [70] is utilized, where signal fundamental frequency is built-in as a state variable. Compared to conventional frequency estimation algorithms, the proposed method can achieve high accuracy and computational efficiency when subject to low SNR condition [70].

Then, a DFT-based phasor parameter calculation algorithm is discussed. The aforementioned fundamental frequency estimator provides an ambient real-time fundamental frequency value, which is leveraged to tune phasor calculation and perform spectral leakage compensation. To alleviate the spectral leakage caused by slow-varying decaying DC component, a hybridization technique [71] is designed, where properties of decaying DC component are embedded in the algorithm signal model, and thus no longer mistakenly represented by spectral leakage components.

7.2 Limitations of DFT-Based Phasor Calculation Methods and Proposed Mitigation Solution

DFT-based algorithms are extensively used in PMUs. DFT adopts a signal model where it is assumed that the input signal is composed of a single-tone fundamental frequency signal, as well as DC and its harmonic components. Correspondingly, in frequency domain, DFT models all the frequency components as precisely residing on the frequencies associated with DFT bins [68], shown as:

$$k\Delta f_{\mathrm{DFT}} \equiv \frac{k}{T}, k \in \left(-\left\lfloor\frac{N}{2}\right\rfloor, \left\lceil\frac{N}{2}\right\rceil - 1\right)$$

which are determined by data window length T and data widow sample size N.

For instance, for a data window of 16.667 ms consisting of 100 samples, the DFT bins range from -49×60Hz to 50×60Hz (100 bins in total) with a bin interval, i.e., the DFT resolution, of $\Delta f_{\mathrm{DFT}} = 60\mathrm{Hz}$. Note that, theoretically, N can be either an odd number or an even number. Practically, however, since DFT is calculated using FFT, to expedite computational speed, N is usually chosen to be the power of 2, and thus is always an even number. This interpretation of input signal in terms of components on "frequency bins" is termed "picket fence effect" [67].

The picket fence effect does not present a major problem when the actual signal frequency profile matches the DFT bin frequencies. In the real power grid operating scenarios, the input signal frequency profile may deviate from the DFT bin frequency values. Undesirably, DFT still perceives the input signal as the superposition of the harmonics of the presumed DFT resolution. As a result, each actual frequency component in the signal will appear to "leak" into the whole DFT spectrum, and this phenomenon is named "spectral leakage phenomenon" [67]-[68]. Equivalently, due to frequency leakage, each one of the N calculated DFT components consists of the leakage portions of all of the actual frequency components in the input signal. The impact of frequency deviation on phasor parameter calculation is shown in Figure 10, where the impact of frequency leakage is quantified as TVE [10]. The spectra of five different frequency inputs are illustrated in Figure 10. Two-cycle data window is used in all cases, and therefore, the DFT resolution is 30Hz.

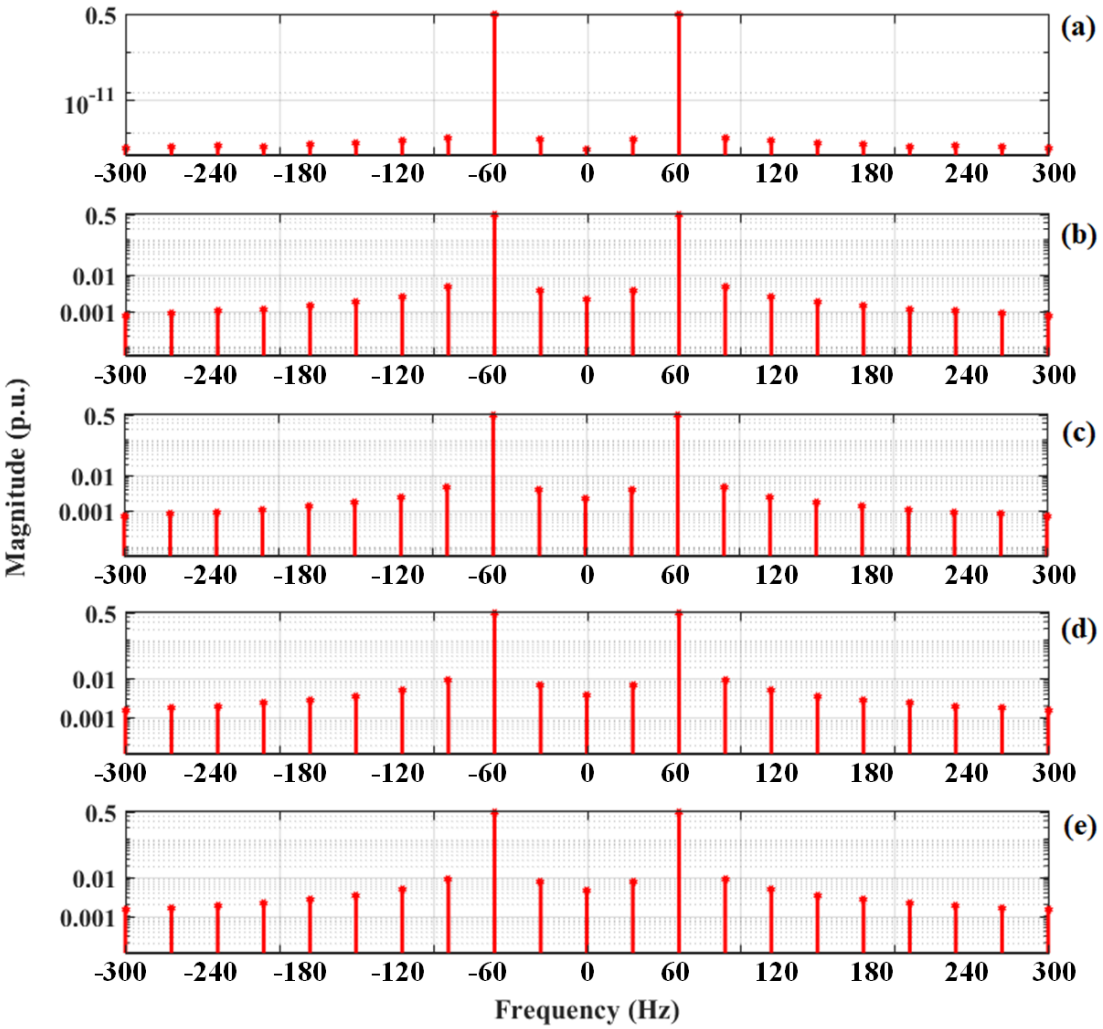

Figure 10 Frequency leakage effect with different input signal fundamental frequencies. (a) 60Hz, (b) 60.25Hz, (c) 59.75Hz, (d) 60.5Hz, (e) 59.5Hz

In a more realistic scenario, data sampling noise, such as thermal noise and electromagnetic interference, should be taken into account. In Figure 11, four SNR cases are simulated and the TVE results are illustrated. It can be clearly observed that to an extent DFT is resistant to noise infiltration. However, when the noise level is too high (30dB in Figure 11), the deterioration of DFT performance due to noise infiltration is consistent across a wide range of frequency deviation level.

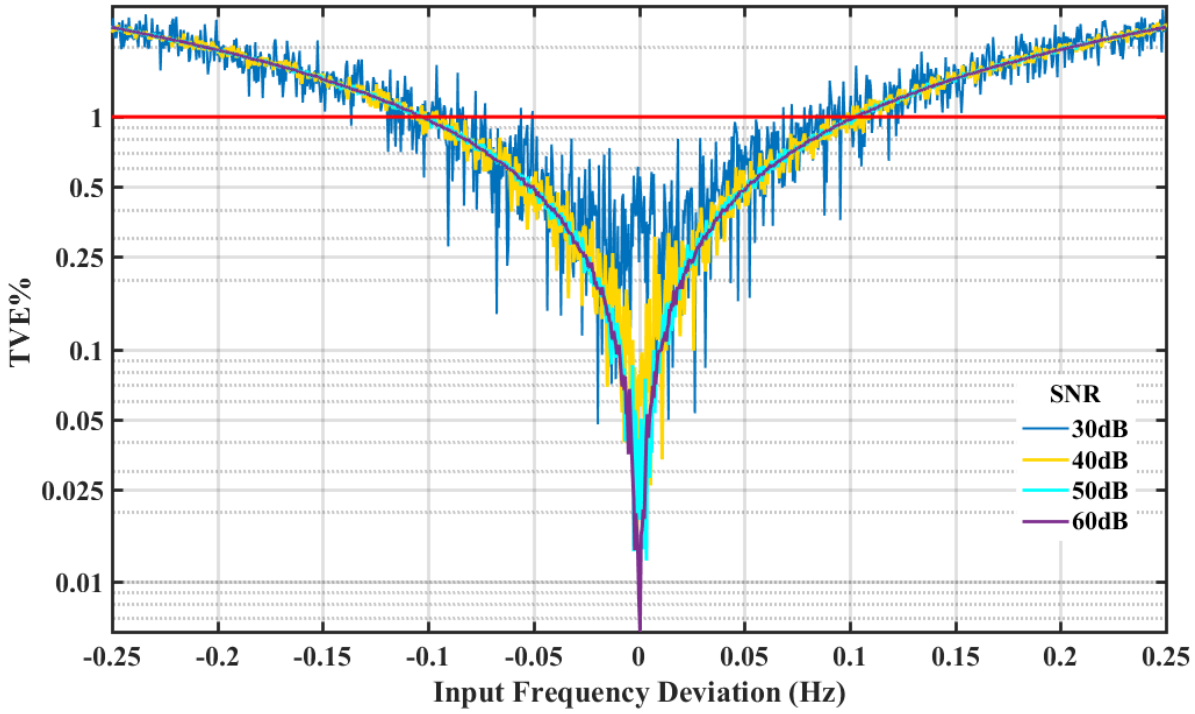

Figure 11 DFT frequency leakage impact on TVE of calculated phasors, considering white Gaussian measurement noise

A variety of measures can be taken to alleviate frequency leakage, such as increasing data window length (to increase DFT resolution), applying window function, and compensation algorithms (e.g., IpDFT). None of the existing algorithms resolves the problem of spectral leakage from a fundamental perspective, and that is to address the root cause of spectral leakage in the first place: the discrepancy between actual fundamental frequency and DFT bin frequency.

The proposed remedy of spectral leakage is to adaptively adjust DFT bin frequency, thus effectively eliminate the cause of spectral leakage. This is achieved by adjusting the DFT data window length adaptively according to the most recent signal fundamental frequency estimate. A highly noise-resistant fundamental frequency tracking method based on UKF is proposed next.

7.3 Unscented[†] Kalman Filter-Based Fundamental Frequency Tracking Technique

In the electric power system, there are two major difficulties in the estimation of fundamental frequency. First, the frequency parameter is embedded in a nonlinear sinusoidal function. Solving a nonlinear function typically requires iterative approach, which introduces the issue of computational burden and divergence. Second, the transducers and data communication channels in a substation environment are potentially contaminated by high noise level [72]. An algorithm that works on such data samples should be resistant to low SNR conditions. Traditionally, Kalman filter and EKF [73] are used for the estimation of state variables in linear and nonlinear system, respectively, where the noise in the dynamic system is modeled as AWGN. As later stated in Equation (7.13), the normal working point of the state variables is in close proximity to the most nonlinear section of the dynamic system equation, making both Kalman filter and EKF unreliable. As a result, UKF [74] is used, and is proven to be stable and accurate in frequency tracking. The limitations of Kalman filter and EKF and necessity for UKF are further elaborated in Sections 7.3.2 - 7.3.4.

7.3.1 Fundamentals of Kalman Filter

Kalman filter was invented in the 1960s [74], and was widely applied in the navigation and control of vehicles, especially aircraft and spacecraft [75]-[81]. Kalman filtering is an algorithm that uses a series of measurements from multiple sensors to jointly yield the best estimate of states of a dynamic system. Despite prevailing measurement noise and inherent uncertainties

[†] The reason for the term "unscented" in the context of "Unscented Transform" and UKF was not explained in its inventors' publications [74].

in states, Kalman filtering produces the best estimate in the sense of minimizing least square error [81]-[85].

In a dynamic system, the states of the system, by definition, are the smallest set of variables that completely characterizes the system [73],[85]. With states, the temporal development and measurement output of the system can be determined. Kalman filter is one of the approaches available to estimate state using the measurement output. Kalman filter can be derived from a variety of scientific context, such as control theory [85], probability theory [82], etc. In Appendix D, the derivation of Kalman filter is based on orthogonal projection principle, in which Kalman filter minimizes the MMSE of state estimate [86].

7.3.2 Caveats of Kalman Filter and EKF in Nonlinear State Estimation

The generic formulation of a dynamic system can be expressed as:

$$\boldsymbol{x}(n) = \boldsymbol{F}[\boldsymbol{x}(n-1), \boldsymbol{w}(n)] \tag{7.1}$$

$$\boldsymbol{y}(n) = \boldsymbol{C}[\boldsymbol{x}(n), \boldsymbol{v}(n)] \tag{7.2}$$

The generic formulation does not assume additivity of noise terms $\boldsymbol{w}(n)$ and $\boldsymbol{v}(n)$, and the dynamic system model $\boldsymbol{F}$ and $\boldsymbol{C}$ are assumed to be known.

As can be observed from Equation D.1 in Appendix D, the Kalman filtering procedure uses a weighted innovation term to correct the propagation of past state-estimate. The weight is termed Kalman gain, which is determined by the propagated correlation matrices of past state-estimate and past measurements. Intuitively, the correlation matrices symbolizes the "confidence" in either past state-estimate or measurements.

Conventional Kalman Filter achieves optimality in the sense of MMSE when the system equation is linear, and noise terms are characterized by the first two moments (mean and deviation) only. In particular, when the previous step random variable $\hat{\boldsymbol{x}}(n-1|\mathcal{Y}_{n-1})$ is Gaussian,

which can be uniquely characterized by the first two moment entirely, and the dynamic system Equations (7.1) and (7.2) are linear, the Gaussianity of $\hat{\boldsymbol{x}}(n|\mathcal{Y}_{n-1})$ and $\hat{\boldsymbol{y}}(n|\mathcal{Y}_{n-1})$ is guaranteed. In this case, the random variables after propagating through a linear system can also be uniquely determined by their first two moments, which can be derived from the state transition matrix and measurement matrix. As a result, the MMSE optimality of Kalman filter in the linear dynamic system case is achieved essentially through orthogonal projection theorem. In particular, the best estimate $\hat{\boldsymbol{x}}(n|\mathcal{Y}_n)$ is the one where uncertainty vector, $\boldsymbol{x}(n) - \hat{\boldsymbol{x}}(n|\mathcal{Y}_n)$, is uncorrelated (orthogonal) to the state vector $\boldsymbol{x}(n)$ [86].In the case of Gaussian random variables, the derivation of Kalman filter, as elaborated in Appendix D, guarantees such orthogonality, and thus is always MMSE optimal.

In most realistic scenarios, however, the dynamic systems under study are intrinsically nonlinear. In the case of nonlinear system equations, the statistics of random variables after propagation need not necessarily be determined by only the first two moments. As a result, with matrices $\boldsymbol{K}(n, n-1)$ and $\boldsymbol{R}(n)$, the MMSE optimality of Kalman filter cannot be guaranteed. Fundamentally, what is needed is the *a posteriori* values of covariance matrix. One way is to approximate the nonlinear dynamic system equations in terms of linear terms, and propagate the covariance matrix as if the system is still linear, and this is the basis for EKF [87]-[88].

The rationale for EKF is very intuitive: linearizing nonlinear system equations at the vicinity of its working point using Taylor expansion, while only the linear terms are preserved. Linearity is a strong assumption, and the approximation of nonlinearity is only valid when the system equation is almost linear around the working point of the system. Otherwise, EKF will lead to significant estimation errors. As will be discussed in later sections, the system equation is

highly nonlinear around the normal working point of power system at around 60Hz, rendering EKF ineffective.

The other way is to leave the nonlinear transformation as is, but rather estimate the *a posteriori* values of sample covariance matrix by selecting samples prior to the nonlinear transformation, letting them propagate through the nonlinear transformation, and calculating the covariance matrix. This procedure is described as the "Unscented Transform" [89]-[92].

Unlike Monte-Carlo simulation, where state samples are randomly chosen, in Unscented Transform, state samples, termed σ-points, are selected deterministically. In particular, the σ-points are meticulously chosen so that the statistics of the original distribution can be preserved up to a number of moments determined by the user. Unscented Transform is the basis of UKF [93]-[98], which is discussed next.

7.3.3 Fundamental Frequency Tracking Using UKF

Unscented Transform provides an alternative, and usually more accurate, approach to estimate the *a posteriori* values of sample covariance matrix. The implementation of UKF is described in Algorithm 3 in Appendix D.5. Compared to the linear Kalman filter and EKF, UKF is able to yield accurate estimate if the dynamic system equation is highly nonlinear, which is the case in this Dissertation.

The key to UKF is the selection of σ-points. The typical assumption is that sampling noise is AWGN, which can be characterized by its first two moments: mean vector, and diagonal covariance matrix. In a variety of literature, the selection of σ-points is based on preserving only the first two moments of input samples.

7.3.4 System Equations for Fundamental Frequency Estimation

Three consecutive samples of a single-phase waveform can be described as:

$$x_k = A \cdot \cos(\omega k \Delta t + \phi_0) \tag{7.3}$$

$$x_{k+1} = A \cdot \cos[\omega(k+1)\Delta t + \phi_0] \tag{7.4}$$

$$x_{k+2} = A \cdot \cos[\omega(k+2)\Delta t + \phi_0] \tag{7.5}$$

It can thus be proven [70] that:

$$x_{k+2} + x_k = 2x_{k+1} \cdot \cos(\omega \Delta t) \tag{7.6}$$

The electric power is transmitted through three-phase transmission system, with 120° electric phase angle displacement between any two phases. This phase angle displacement is determined by the symmetric design of synchronous generators, and thus always holds true for normal operation.

Denote phase A voltage as x_k, phase B voltage as y_k, and phase C voltage as z_k. Then,

$$y_k = A \cdot \cos\left(\omega k \Delta t + \phi_0 - \frac{2}{3}\pi\right) \tag{7.7}$$

$$z_k = A \cdot \cos\left(\omega k \Delta t + \phi_0 + \frac{2}{3}\pi\right) \tag{7.8}$$

It can be shown that y_k can be conveniently expressed with phase A waveform measurements, shown in Equation (7.9):

$$\begin{aligned} y_k &= A \cdot \cos(\omega k \Delta t + \phi_0)\cos\left(-\frac{2}{3}\pi\right) - A \cdot \sin(\omega k \Delta t + \phi_0)\sin(-\frac{2}{3}\pi) \\ &= x_k \cos\left(-\frac{2}{3}\pi\right) + \frac{x_k \cos(\omega \Delta t) - x_{k-1}}{\sin(\omega \Delta t)} \sin\left(-\frac{2}{3}\pi\right) \end{aligned} \tag{7.9}$$

Similarly,

$$z_k = x_k \cos\left(\frac{2}{3}\pi\right) + \frac{x_k \cos(\omega \Delta t) - x_{k-1}}{\sin(\omega \Delta t)} \sin\left(\frac{2}{3}\pi\right) \tag{7.10}$$

Besides, similar to Equation (7.6), for both phase B and phase C waveform samples:

$$y_{k+2} + y_k = 2y_{k+1} \cdot \cos(\omega \Delta t) \tag{7.11}$$

$$z_{k+2} + z_k = 2z_{k+1} \cdot \cos(\omega \Delta t) \tag{7.12}$$

From Equation (7.6), it can be observed that,

$$f = \frac{1}{2\pi \Delta t} \cdot \cos^{-1}\left(\frac{x_{k+2} + x_k}{2x_{k+1}}\right) \tag{7.13}$$

When the sampling frequency of a field transducer is adequately high, the argument in the inverse cosine function is close to 1. Consequently, the working point of the nonlinear equation (7.6) is at the most nonlinear part of the inverse cosine function. As a result, the EKF-based method will incur large error.

In this Dissertation, the system state-space equation is formulated as follows;

Choosing the states and measurement variables as follows:

States: $$x_{1,k} = x_k, x_{2,k} = x_{k-1}, x_{3,k} = \omega \Delta t \tag{7.14}$$

Measurements: $$y_{1,k} = x_k, y_{2,k} = y_k, y_{3,k} = z_k \tag{7.15}$$

As a result, the state update equation and measurement input equation can be expressed as:

$$x_{1,k+1} = -x_{2,k} + 2x_{1,k}\cos(x_{3,k}) \tag{7.16}$$

$$x_{2,k+1} = x_k = x_{1,k} \tag{7.17}$$

$$x_{3,k+1} = x_{3,k} \tag{7.18}$$

$$y_{1,k+1} = x_{1,k+1} \tag{7.19}$$

$$y_{2,k+1} = x_{1,k+1}\cos\left(\frac{2}{3}\pi\right) - \frac{x_{1,k+1}\cos\left(x_{3,k+1}\right) - x_{2,k+1}}{\sin(x_{3,k+1})}\sin\left(\frac{2}{3}\pi\right) \tag{7.20}$$

$$y_{3,k+1} = x_{1,k+1}\cos\left(\frac{2}{3}\pi\right) + \frac{x_{1,k+1}\cos\left(x_{3,k+1}\right) - x_{2,k+1}}{\sin(x_{3,k+1})}\sin\left(\frac{2}{3}\pi\right) \tag{7.21}$$

Note that $x_{3,k} = \omega\Delta t = 2\pi f \Delta t$, where Δt is the sampling interval. Therefore, frequency is estimated by:

$$f = \frac{x_{3,k}}{2\pi\Delta t} \tag{7.22}$$

When only single-phase measurements are available, Equations (7.16)-(7.19) should be used; when additional observations of the other two phases are present, Equations (7.20) and (7.21) can be incorporated. Frequency is estimated using Equation (7.22)

7.3.5 Selection of σ-points

In UKF, sigma points are a collection of samples from the original distribution, deterministically chosen in such a way that the first two moments of sigma points preserve the first two moments of the original distributions. The sigma points are then propagated to the new distribution through the nonlinear function, where the statistics of the new distribution can be calculated using the propagated sigma points. The selection of sigma points is done in the following way:

$$\begin{gathered} \chi_0 = \bar{x} \\ \chi_i = \bar{x} + \left(\sqrt{(n+\lambda)P_{xx}}\right)_i, i = 1,2,\dots,n \\ \chi_{i+n} = \bar{x} - \left(\sqrt{(n+\lambda)P_{xx}}\right)_i \end{gathered} \tag{7.23}$$

where n is the number of states, $\lambda = \alpha^2(n+\kappa)$, $\left(\sqrt{(n+\lambda)P_{xx}}\right)_i$ is the ith column of the square root of matrix $(n+\lambda)P_{xx}$, and can be efficiently calculated using by Cholesky decomposition [98].

The sigma points are then propagated through the nonlinear function $\gamma_i = f(\chi_i)$, where the first two moments of the new distribution can be calculated as follows:

$$\bar{y} = \sum_{i=0}^{2n} W_i^{(m)} \gamma_i \tag{7.24}$$

$$P_{yy} = \sum_{i=0}^{2n} W_i^{(c)} [(\gamma_i - \bar{y})(\gamma_i - \bar{y})^T] \tag{7.25}$$

where weights $W_i^{(m)}$ and $W_i^{(c)}$ are defined as follows:

$$W_0^{(m)} = \frac{\lambda}{n+\lambda}, W_0^{(c)} = W_0^{(m)} + (1 - \alpha^2 + \beta) \tag{7.26}$$

$$W_i^{(m)} = W_i^{(c)} = \frac{1}{2(n+\lambda)}, i = 1,2, \dots, n \tag{7.27}$$

In Equations (7.23)-(7.26), factors α and κ are used to provide fine-tuning of the "spread" of sigma points around the mean $\chi_0 = \bar{x}$. Parameter β is used to incorporate information about higher moments of the original distribution. There is no uniform method to select sigma points, and the available approaches are described in detail in [99]-[101].

7.4 DFT-Based Phasor Parameter Calculation Algorithm with Fundamental Frequency Tuning Adaptability

The calculated signal fundamental frequency can be effectively leveraged to mitigate spectral leakage effect in DFT calculation. Specifically, by changing data window length according to actual signal fundamental frequency, DFT bin frequencies can be adaptively tuned to match the actual harmonic frequency profile of input signal. Regardless, since the data window size can only take discreet values of multiples of the sampling interval, perfect matching between DFT bin frequencies (determined by window length) and input frequency profile may not always be feasible. As a result, spectral compensation may still be necessary. The spectral compensation approach is discussed in detail next.

7.4.1 Effect of the Sampling Rate on Adaptive Window Sizing Method

As aforementioned, by tracking the actual fundamental frequency, and subsequently adjusting the data window size, spectral leakage in DFT calculation will be alleviated and even avoided. The resolution of such window length adjustment, which fundamentally determines the performance of such technique, depends solely on sampling frequency. Intuitively, the higher the sampling frequency is, the more flexible and accurate such adjustment can be. A MATLAB simulation is conducted to show that it is impractical to rely on increasing sampling frequency to achieve alleviation of spectral leakage.

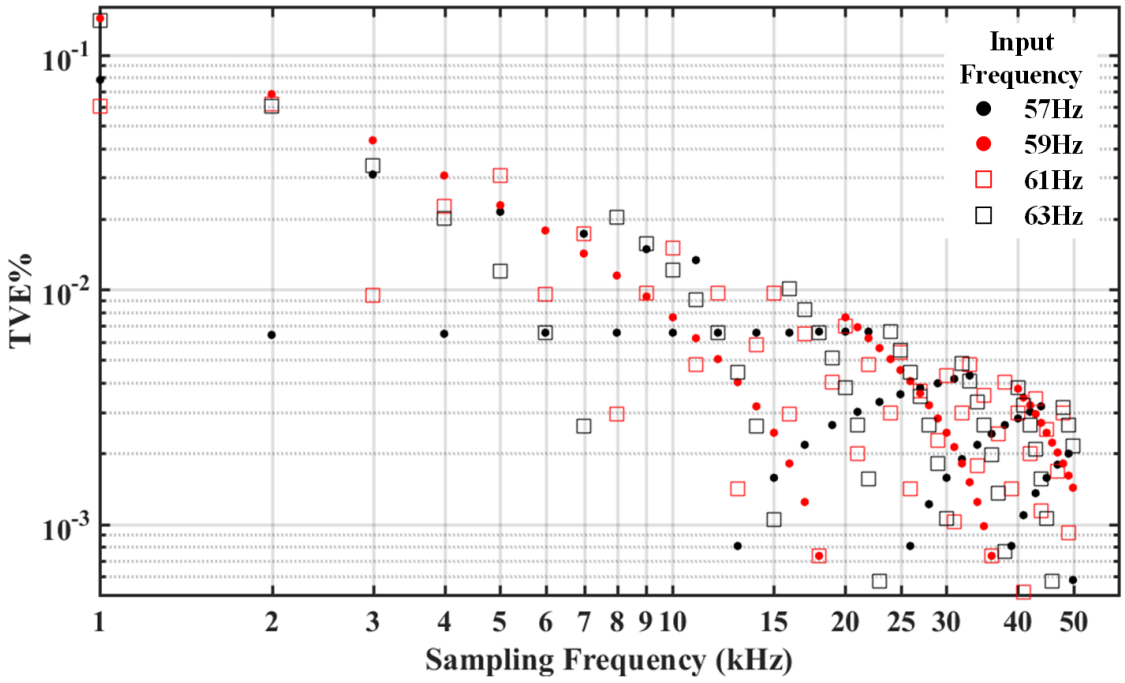

Figure 12 Effect of sampling frequency on TVE when adaptive window sizing is adopted

As shown in Figure 12, if it is desired to compensate for spectral leakage with increasing sampling frequency alone, the sampling frequency need to be higher than 15kHz. Among the

current commercial PMU models manufactured by Schweitzer Engineering Laboratories (SEL), the typical sampling rate is 960Hz (16 samples/cycle) and 7680Hz (128 samples/cycle), and only one model samples above 15kHz (30.72kHz, or 512 samples/cycle). It is thus asserted that increasing sampling rate alone is not adequate to mitigate spectral leakage within a practical context, and as a result, additional compensation is needed.

7.4.2 Formulation of Spectral Leakage Compensation Technique

7.4.2.1 Key Definitions

k: input harmonic order

m: DFT bin number

K: highest harmonic order +1

$\alpha_k \equiv k f_{\text{input}}/f_{\text{sampling}}$

$N \equiv \left\lfloor \frac{f_{\text{sampling}}}{f_{\text{input}}} \right\rfloor$: total number of samples in a cycle

$$a_k^m \equiv 2\pi\alpha_k - \frac{2\pi m}{N} \qquad A_k^m \equiv e^{\mathrm{j}\frac{a_k^m(N-1)}{2}} \frac{\sin\left(\frac{1}{2}a_k^m N\right)}{N \cdot \sin\left(\frac{1}{2}a_k^m\right)}$$

$$b_k^m \equiv -\left(2\pi\alpha_k + \frac{2\pi m}{N}\right) \qquad B_k^m \equiv e^{\mathrm{j}\frac{b_k^m(N-1)}{2}} \frac{\sin\left(\frac{1}{2}b_k^m N\right)}{N \cdot \sin\left(\frac{1}{2}b_k^m\right)}$$

7.4.2.2 Relationship Between Leakage Frequency Components and DFT Bin Frequencies

When spectral leakage occurs, each frequency component, kth harmonic, in the actual signal leaks into all frequency bins. Equivalently, the component at frequency bin m consists of the leakage contribution originated from each actual kth harmonic component. It can be shown that once the fundamental frequency is determined, there is a deterministic relationship between the kth harmonic component and the mth DFT bin component. The mth DFT bin component can

be conveniently acquired, and thus the "true" phasor associated with the kth harmonic component can be derived.

The input signal can be expressed in terms of the superposition of harmonic components:

$$\begin{aligned} x(n) &= \sum_{k=0}^{K} A_k \cos(2\pi\alpha_k n + \phi_k) \equiv A_k \cos(2\pi\alpha_k n + \phi_k) \\ &= \frac{A_k}{2} e^{\mathrm{j}2\pi\alpha_k n} e^{\mathrm{j}\phi_k} + \frac{A_k}{2} e^{-\mathrm{j}2\pi\alpha_k n} e^{-\mathrm{j}\phi_k} \end{aligned} \tag{7.28}$$

where Einstein summation convention [102]-[103] is applied to simplify the writing of equations throughout the rest the section.

Taking the DFT of $x(n)$:

$$X^m = X_k^m \equiv \frac{\sqrt{2}}{N} \sum_{n=0}^{N-1} x_k(n) e^{-\mathrm{j}\frac{2\pi}{N}mn} \tag{7.29}$$

Substitute $x_k(n)$ in Equation (7.29) with Equation (7.28), we may get:

$$X^m = \frac{\sqrt{2}}{2} \widehat{X_k} A_k^m + \frac{\sqrt{2}}{2} \left(\widehat{X_k}\right)^* B_k^m \tag{7.30}$$

where $(X)^*$ implies complex conjugate of a complex number X. Using the property $\widehat{X_k} \equiv \widehat{X_k^r} + \mathrm{j}\widehat{X_k^i}$, where $\widehat{X_k^r}, \widehat{X_k^i} \in \mathbb{R}$ are the real and imaginary parts of $\widehat{X_k}$, respectively. Similarly, $A_k^m \equiv A_k^{m,r} + \mathrm{j}A_k^{m,i}$, and $B_k^m \equiv B_k^{m,r} + \mathrm{j}B_k^{m,i}$. Substitute the quantities in Equation (7.30) with their real and imaginary parts, and equate the real and imaginary parts of l.h.s. and r.h.s, there is:

$$\sqrt{2}X^{m,r} = A_k^{m,r}\widehat{X_k^r} - A_k^{m,i}\widehat{X_k^i} + B_k^{m,r}\widehat{X_k^r} + B_k^{m,i}\widehat{X_k^i} \tag{7.31}$$

$$\sqrt{2}X^{m,i} = A_k^{m,i}\widehat{X_k^r} + A_k^{m,r}\widehat{X_k^i} + B_k^{m,i}\widehat{X_k^r} - B_k^{m,r}\widehat{X_k^i} \tag{7.32}$$

Note that, Equations (7.31) and (7.32) comply with the Einstein Notation, and the summation is w.r.t. parameter k. Rearrange in terms of $\widehat{X_k^r}$and $\widehat{X_k^i}$, we get:

$$\sqrt{2}X^{m,r} = \left(A_k^{m,r} + B_k^{m,r}\right)\widehat{X_k^r} + \left(-A_k^{m,i} + B_k^{m,i}\right)\widehat{X_k^i}$$
$$\triangleq \beta_k^m \widehat{X_k^r} + \gamma_k^m \widehat{X_k^i} \tag{7.33}$$

$$\sqrt{2}X^{m,i} = \left(A_k^{m,i} + B_k^{m,i}\right)\widehat{X_k^r} + \left(A_k^{m,r} - B_k^{m,r}\right)\widehat{X_k^i}$$
$$\triangleq \delta_k^m \widehat{X_k^r} + \varepsilon_k^m \widehat{X_k^i} \tag{7.34}$$

Reexamine the knowns and unknowns in Equations (7.33) and (7.34). On the l.h.s., $X^m, m = 0,1,\dots,N-1$ are obtained by the DFT calculation of input signal; on the r.h.s., the quantities with hats are the unknowns, i.e., the phasors that are apropos of the "true" harmonic components in the input signal. Reformat Equations (7.33) and (7.34) into matrix forms:

$$\begin{bmatrix} \sqrt{2}X^{0,r} \\ \sqrt{2}X^{1,r} \\ \vdots \\ \sqrt{2}X^{N-1,r} \end{bmatrix} = \boldsymbol{\Gamma} \begin{bmatrix} \widehat{X_0^r} \\ \widehat{X_1^r} \\ \vdots \\ \widehat{X_{K-1}^r} \end{bmatrix}$$
$$\boldsymbol{\Gamma} \equiv \begin{bmatrix} \beta_0^0 & \beta_1^0 & \cdots & \beta_{K-1}^0 & \gamma_0^0 & \gamma_1^0 & \cdots & \gamma_{K-1}^0 \\ \beta_0^1 & \beta_1^1 & \cdots & \beta_{K-1}^1 & \gamma_0^1 & \gamma_1^1 & \cdots & \gamma_{K-1}^1 \\ \vdots & \vdots & & \vdots & \vdots & \vdots & & \vdots \\ \beta_0^{N-1} & \beta_1^{N-1} & \cdots & \beta_{K-1}^{N-1} & \gamma_0^{N-1} & \gamma_1^{N-1} & \cdots & \gamma_{K-1}^{N-1} \end{bmatrix} \tag{7.35}$$

$$\begin{bmatrix} \sqrt{2}X^{0,i} \\ \sqrt{2}X^{1,i} \\ \vdots \\ \sqrt{2}X^{N-1,i} \end{bmatrix} = \boldsymbol{\Delta} \begin{bmatrix} \widehat{X_0^r} \\ \widehat{X_1^r} \\ \vdots \\ \widehat{X_{K-1}^r} \end{bmatrix}$$
$$\boldsymbol{\Delta} \equiv \begin{bmatrix} \delta_0^0 & \delta_1^0 & \cdots & \delta_{K-1}^0 & \varepsilon_0^0 & \varepsilon_1^0 & \cdots & \varepsilon_{K-1}^0 \\ \delta_0^1 & \delta_1^1 & \cdots & \delta_{K-1}^1 & \varepsilon_0^1 & \varepsilon_1^1 & \cdots & \varepsilon_{K-1}^1 \\ \vdots & \vdots & & \vdots & \vdots & \vdots & & \vdots \\ \delta_0^{N-1} & \delta_1^{N-1} & \cdots & \delta_{K-1}^{N-1} & \varepsilon_0^{N-1} & \varepsilon_1^{N-1} & \cdots & \varepsilon_{K-1}^{N-1} \end{bmatrix} \tag{7.36}$$

Note that, with all the aliasing components in the input signal effectively removed, the highest observable harmonic order is always higher than or equal to the actual existing harmonic

order, i.e., $N \geq K$. Therefore, least-square technique can be used to calculate the real and imaginary parts of the theoretical phasors, shown in Equations (7.37) – (7.39).

$$\begin{bmatrix} \widehat{X_0^r} \\ \widehat{X_1^r} \\ \vdots \\ \widehat{X_{K-1}^r} \end{bmatrix} = \boldsymbol{\Gamma}^{+} \begin{bmatrix} \sqrt{2}X^{0,r} \\ \sqrt{2}X^{1,r} \\ \vdots \\ \sqrt{2}X^{N-1,r} \end{bmatrix} \tag{7.37}$$

$$\begin{bmatrix} \widehat{X_0^i} \\ \widehat{X_1^i} \\ \vdots \\ \widehat{X_{K-1}^i} \end{bmatrix} = \boldsymbol{\Delta}^{+} \begin{bmatrix} \sqrt{2}X^{0,i} \\ \sqrt{2}X^{1,i} \\ \vdots \\ \sqrt{2}X^{N-1,i} \end{bmatrix} \tag{7.38}$$

$$\widehat{X_k} = \widehat{X_k^r} + \mathrm{j}\widehat{X_k^i} \tag{7.39}$$

where $(\boldsymbol{X})^{+}$ is the Moore-Penrose inverse of a matrix $\boldsymbol{X}$ [98], and $\widehat{X_1}$ is the desired fundamental frequency phasor component.

7.5 Hybridization Framework for Phasor Parameter Calculation

7.5.1 Signal Modeling of Proposed Algorithm

In this Dissertation, a hybridization framework is proposed to incorporate the benefits of both Fourier-based algorithms and curve-fitting based algorithms, as originally proposed in [104]. The significance of this hybridization framework in phasor calculation is that the slow-varying decaying DC component can be effectively represented in signal modeling, so that it does not result in DFT leakage components.

The rationale of the modeling is that both the decaying envelope and the sinusoidal pattern should be captured and incorporated in the modeling of the fundamental frequency signal $x_1(t)$:

$$x_1(t) = a(t) \cdot \cos\left[2\pi f_0 t + 2\pi \int \Delta f(t)\,\mathrm{d}t + \phi_0\right] = a(t) \cdot \cos[2\pi f_0 t + \phi(t)] \tag{7.40}$$

As a common practice in time domain methods [34]-[36], Equation (7.40) can be expanded as:

$$x_1(t) = q(t)\cos(2\pi f_0 t\,) + r(t)\sin(2\pi f_0 t\,) \tag{7.41}$$

where $q(t) = a(t)\cos[\phi(t)],\ r(t) = -a(t)\sin[\phi(t)]$.

Note that Equation (7.40) reflects the slow variations on f_0 component, represented by $a(t)$ and $\phi(t)$ terms, but does not take into account any harmonic components. Based on the modeling of electromagnetic dynamic waveforms in Section 5.3.2, Equation (7.41) is rewritten so that harmonic components are reflected:

$$x(t) = x_1(t) + \sum_{k=2}^{K} h(t; k, \boldsymbol{a}) \tag{7.42}$$

where $h(t; k, \boldsymbol{a})$ reflects harmonic terms, k is harmonic order, $\boldsymbol{a}$ is a vector showing the harmonic characteristics, such as amplitude, phase angle, t is time.

One common process to treat $q(t)$ and $r(t)$ in Equation (7.41) is approximation using polynomials [34]-[36], shown in Equation (7.43):

$$q(t) = \sum_{m=0}^{M-1} c_m P(t; m)\,; r(t) = \sum_{m=0}^{M-1} s_m P(t; m) \tag{7.43}$$

where m is the order of polynomial $P(t; m)$, M is the number of terms in the approximation. Most cases in literature use $M = 3$.

If we rewrite Equation (7.42), we have:

$$x(t) = \left[\sum_{m=0}^{M-1} c_m P(t;m)\right] \cdot \cos(2\pi f_0 t) + \left[\sum_{m=0}^{M-1} s_m P(t;m)\right] \cdot \sin(2\pi f_0 t) + \sum_{k=2}^{K} h(t;k,\boldsymbol{a}) \tag{7.44}$$

In polynomial methods, harmonic terms $\sum_{k=2}^{K} h(t;k,\boldsymbol{a})$ are neglected. In DFT-based methods, M is routinely set to 1, resulting in the commonly known spectrum representation. Consequently, polynomial methods are susceptible to harmonic infiltration, whereas DFT-based methods cannot accurately capture the slow-varying waveform properties in input waveforms.

7.5.2 Hybridization of Fourier and Polynomial Methods

In this Section, a hybrid method is proposed, which combines the merits of both Fourier-based methods and polynomial curve-fitting methods [40]. Specifically, the proposed algorithm is immune to harmonics and noise, and is able to mitigate the impact of slow-varying phenomenon inside a data window, including exponentially decaying DC component. The DFT of a data window is expressed as:

$$\dot{X}_0 = \sum_{k=0}^{N-1} x(k\Delta t) e^{-i\frac{2\pi}{N}k} \tag{7.45}$$

where, $$x(k\Delta t) = q(k\Delta t)\cos\left(\frac{2\pi k}{N}\right) - r(k\Delta t)\sin\left(\frac{2\pi k}{N}\right)$$

Expand $q(k\Delta t)$ and $r(k\Delta t)$ at the center of data window, denoted by $t_c = N\Delta t/2$:

$$\begin{aligned} q(k\Delta t) &\approx c_0 + c_1(k\Delta t - t_c) + c_2(k\Delta t - t_c)^2 \\ &= c_0 + c_1\left(k - \frac{N}{2}\right)\Delta t + c_2\left(k - \frac{N}{2}\right)^2 \Delta t^2 \end{aligned} \tag{7.46}$$

$$r(k\Delta t) \approx s_0 + s_1(k\Delta t - t_c) + s_2(k\Delta t - t_c)^2$$
$$= s_0 + s_1\left(k - \frac{N}{2}\right)\Delta t + s_2\left(k - \frac{N}{2}\right)^2 \Delta t^2 \tag{7.47}$$

Expand $x(k\Delta t)$ in Equation (7.45) with Equations (7.46) and (7.47):

$$X_{0,Re} = \mathbf{Re}\left[\dot{X}_0\right] = \sum_{k=0}^{N-1}\left[c_0 + c_1\left(k - \frac{N}{2}\right)\Delta t + c_2\left(k - \frac{N}{2}\right)^2 \Delta t^2\right]\cos^2\left(\frac{2\pi k}{N}\right)$$
$$- \sum_{k=0}^{N-1}\left[s_0 + s_1\left(k - \frac{N}{2}\right)\Delta t + s_2\left(k - \frac{N}{2}\right)^2 \Delta t^2\right]\sin\left(\frac{2\pi k}{N}\right)\cos\left(\frac{2\pi k}{N}\right) \tag{7.48}$$

$$X_{0,Im} = \mathbf{Im}\left[\dot{X}_0\right] = \sum_{k=0}^{N-1}\left[s_0 + s_1\left(k - \frac{N}{2}\right)\Delta t + s_2\left(k - \frac{N}{2}\right)^2 \Delta t^2\right]\sin^2\left(\frac{2\pi k}{N}\right)$$
$$- \sum_{k=0}^{N-1}\left[c_0 + c_1\left(k - \frac{N}{2}\right)\Delta t + c_2\left(k - \frac{N}{2}\right)^2 \Delta t^2\right]\sin\left(\frac{2\pi k}{N}\right)\cos\left(\frac{2\pi k}{N}\right) \tag{7.49}$$

Organize Equations (7.48) and (7.49) in terms of c_i and s_i coefficients:

$$X_{0,Re} = c_0 \sum_{k=0}^{N-1}\cos^2\left(\frac{2\pi k}{N}\right) + c_1 \sum_{k=0}^{N-1}\left(k - \frac{N}{2}\right)\Delta t \cdot \cos^2\left(\frac{2\pi k}{N}\right)$$
$$+ c_2 \sum_{k=0}^{N-1}\left(k - \frac{N}{2}\right)^2 \Delta t^2 \cdot \cos^2\left(\frac{2\pi k}{N}\right) \tag{7.50}$$
$$- s_0 \sum_{k=0}^{N-1}\sin\left(\frac{2\pi k}{N}\right)\cos\left(\frac{2\pi k}{N}\right)$$

$$
\begin{aligned}
&-s_1 \sum_{k=0}^{N-1} \left(k - \frac{N}{2}\right) \Delta t \cdot \sin\left(\frac{2\pi k}{N}\right) \cos\left(\frac{2\pi k}{N}\right) \\
&- s_2 \sum_{k=0}^{N-1} \left(k - \frac{N}{2}\right)^2 \Delta t^2 \cdot \sin\left(\frac{2\pi k}{N}\right)\left(\frac{2\pi k}{N}\right) \\
&= \alpha_0^0 c_0 + \alpha_1^0 c_1 + \alpha_2^0 c_1 + \lambda_0^0 s_0 + \lambda_1^0 s_1 + \lambda_2^0 s_1 \\
X_{0,Im} = c_0 &\sum_{k=0}^{N-1} \sin\left(\frac{2\pi k}{N}\right) \cos\left(\frac{2\pi k}{N}\right) \\
&- c_1 \sum_{k=0}^{N-1} \left(k - \frac{N}{2}\right) \Delta t \cdot \sin\left(\frac{2\pi k}{N}\right) \cos\left(\frac{2\pi k}{N}\right) \\
&- c_2 \sum_{k=0}^{N-1} \left(k - \frac{N}{2}\right)^2 \Delta t^2 \cdot \sin\left(\frac{2\pi k}{N}\right) \cos\left(\frac{2\pi k}{N}\right) \\
&+ s_0 \sum_{k=0}^{N-1} \cos^2\left(\frac{2\pi k}{N}\right) \\
+ s_1 \sum_{k=0}^{N-1} \left(k - \frac{N}{2}\right) \Delta t \cdot \cos^2\left(\frac{2\pi k}{N}\right) &+ s_2 \sum_{k=0}^{N-1} \left(k - \frac{N}{2}\right)^2 \Delta t^2 \cdot \cos^2\left(\frac{2\pi k}{N}\right) \\
&= \lambda_0^0 c_0 + \lambda_1^0 c_1 + \lambda_2^0 c_1 + \beta_0^0 s_0 + \beta_1^0 s_1 + \beta_2^0 s_1
\end{aligned}
\tag{7.51}
$$

In Equations (7.50) and (7.51), there are two knowns (real and imaginary parts of DFT) and six unknown. In order to balance the numbers of known and unknown, three equally spaced consecutive windows are used, and the signals are approximated at t_c, $t_c + \Delta t$, and $t_c + 2\Delta t$, respectively. The assumption is that during the phasor calculation period (within 2 cycles) of electromagnetic transient events, the variations in electrical quantities in a data window is small

enough, so that curve-fitting coefficients do not change when moving windows are utilized. The moving window scheme is illustrated in Figure 13.

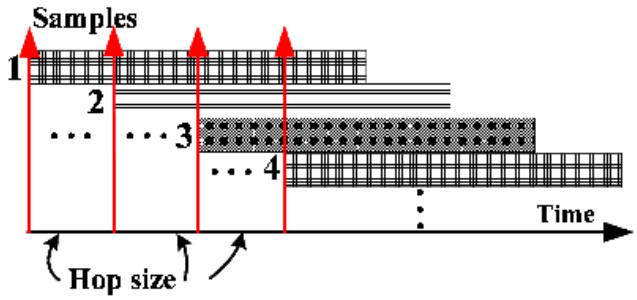

Figure 13 Illustration of overlapping windows and hop size.
Reprinted with permission from C. Qian and M. Kezunovic, "Dynamic synchrophasor estimation with modified hybrid method," *2016 IEEE Power & Energy Society Innovative Smart Grid Technologies Conference (ISGT)*, Minneapolis, MN, pp. 1-5, Sep. 2016. Copyright 2016, IEEE.

For the second window, sampling indices are from 1 to N, and the DFT of waveform:

$$\dot{X}_1 = \sum_{k=0}^{N-1} x[(k+1)\Delta t]e^{-i\frac{2\pi}{N}k} = \sum_{k=1}^{N} x(k\Delta t)e^{-i\frac{2\pi}{N}(k-1)} \tag{7.52}$$

or,
$$\dot{X}_1 e^{-i\frac{2\pi}{N}} = \sum_{k=1}^{N} x(k\Delta t)e^{-i\frac{2\pi}{N}k} \tag{7.53}$$

Similarly, for the third window, where the sample indices are from 2 to $N+1$, the DFT of waveform can be calculated:

$$\dot{X}_1 e^{-i\frac{2\pi}{N}\cdot 2} = \sum_{k=2}^{N+1} x(k\Delta t)e^{-i\frac{2\pi}{N}k} \tag{7.54}$$

The rest of the derivation is similar to Equations (7.46)-(7.51). Note that the left-hand sides of Equations (7.53) and (7.54) correspond to recursive DFT, where the instant phase angle

of sinusoid with nominal frequency is considered as the reference angle. Recursive DFT is essentially an angle adjustment, which can be done conveniently in practice. The r.h.s. of Equations (7.52) and (7.53) have the same structure as Equations (7.45), and the only difference is the indices of summation, which does not increase any computation complexity.

The fitting coefficients can be computed as follows:

$$\alpha_m^n = \sum_{k=n}^{N+n-1} \left(k - \frac{N}{2}\right)^m \Delta t^m \cos^m\left(\frac{2\pi k}{N}\right) \tag{7.55}$$

$$\beta_m^n = \sum_{k=n}^{N+n-1} \left(k - \frac{N}{2}\right)^m \Delta t^m \sin^m\left(\frac{2\pi k}{N}\right) \tag{7.56}$$

$$\lambda_m^n = -\sum_{k=n}^{N+n-1} \left(k - \frac{N}{2}\right)^m \Delta t^m \sin\left(\frac{2\pi k}{N}\right)\cos\left(\frac{2\pi k}{N}\right) \tag{7.57}$$

where $m, n = 0,1,2$ ..., the superscript on coefficient denotes the number of windows, and the subscript indicates the order of corresponding polynomial. In order to construct a solvable matrix equation, $\max(m) = \max(n)$ needs to be satisfied.

In the case where $\max(m) = \max(n) = 2$, the matrix equation is as follows,

$$\begin{bmatrix} \mathbf{Re}\left[\dot{X}_0\right] \\ \mathbf{Re}\left[\dot{X}_1\theta\right] \\ \mathbf{Re}\left[\dot{X}_2\theta^2\right] \\ \mathbf{Im}\left[\dot{X}_0\right] \\ \mathbf{Im}\left[\dot{X}_1\theta\right] \\ \mathbf{Im}\left[\dot{X}_2\theta^2\right] \end{bmatrix} = \begin{bmatrix} \alpha_0^0 & \alpha_1^0 & \alpha_2^0 & \lambda_0^0 & \lambda_1^0 & \lambda_2^0 \\ \alpha_0^1 & \alpha_1^1 & \alpha_2^1 & \lambda_0^1 & \lambda_1^1 & \lambda_2^1 \\ \alpha_0^2 & \alpha_1^2 & \alpha_2^2 & \lambda_0^2 & \lambda_1^2 & \lambda_2^2 \\ \lambda_0^0 & \lambda_1^0 & \lambda_2^0 & \beta_0^0 & \beta_1^0 & \beta_2^0 \\ \lambda_0^1 & \lambda_1^1 & \lambda_2^1 & \beta_0^1 & \beta_1^1 & \beta_2^1 \\ \lambda_0^2 & \lambda_1^2 & \lambda_2^2 & \beta_0^2 & \beta_1^2 & \beta_2^2 \end{bmatrix} \begin{bmatrix} c_0 \\ c_1 \\ c_2 \\ s_0 \\ s_1 \\ s_2 \end{bmatrix} \tag{7.58}$$

where $\theta \equiv e^{-i\frac{2\pi}{N}}$ is the rotating factor which does not change the amplitude of the phasor and rotate the phase angle clockwise by one sampling angle interval. Note that Equation (7.58) is a lin-

ear matrix equation, where the matrix on the right-hand side is fixed, whose inverse can be calculated and stored beforehand. As a result, solving the fitting coefficient is just a matrix multiplication.

Traditionally, frequency is calculated using the differentiation of consecutive angle values. This method may perform well under simulation conditions with noiseless test signals. However, when noise is presented in real measurements, differentiation will inevitably magnify computation uncertainties. Instead, two matrices are constructed for frequency deviation and ROCOF estimation using acquired fitting coefficients.

Taking the derivative of $p(t) = a(t)e^{\mathrm{j}\phi(t)}$:

$$p'(t) = a'(t)e^{\mathrm{j}\phi(t)} + \mathrm{j}p(t)\phi'(t) \tag{7.59}$$

Separating the real and imaginary parts of Equation (7.49), there is:

$$\mathbf{Re}[p'(t)] = a'(t)\cos\phi(t) - s(t)\phi'(t) = c_1 \tag{7.60}$$

$$\mathbf{Im}[p'(t)] = a'(t)\sin\phi(t) + c(t)\phi'(t) = s_1 \tag{7.61}$$

Or equivalently expressed:

$$\begin{bmatrix} c_1 \\ s_1 \end{bmatrix} = \begin{bmatrix} \cos\varphi(t) & -s_0 \\ \sin\varphi(t) & c_0 \end{bmatrix} \begin{bmatrix} a'(t) \\ \phi'(t) \end{bmatrix} \tag{7.62}$$

Solving Equation (7.62), frequency deviation can be acquired:

$$\Delta f(t) = \frac{\phi'(t)}{2\pi} \tag{7.63}$$

7.5.3 Generic Hybridization Framework for Linear Algorithms

The hybridization example in Section 7.5.2 can be generalized to a generic framework [71]. The purpose of this generalization is to provide a platform so that the merits of multiple algorithms can be exploited simultaneously. The assumption of this framework is that each candi-

date algorithm is based on linear model. This means in each candidate algorithm, the signal is decomposed by projecting the signal onto preselected vector space, and thereafter interpreted as the coefficient on each basis vector. For example, both DFT and polynomial fitting algorithm fit into this criterion. The proposed algorithm hybridization framework is illustrated in Figure 14.

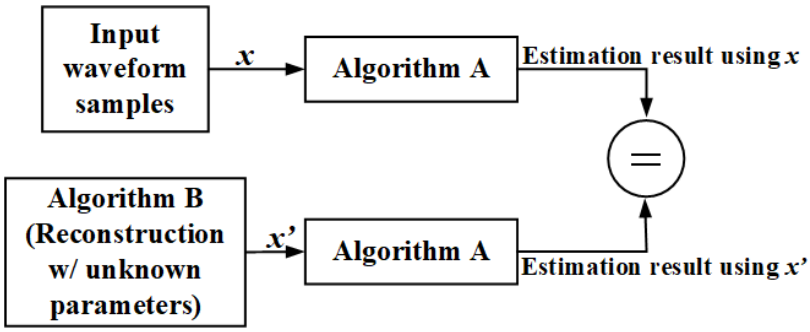

Figure 14 Proposed hybridization framework for two algorithms.
Reprinted with permission from C. Qian and M. Kezunovic, "Hybridization framework for improved dynamic phasor parameter estimation algorithms," *2019 IEEE Power & Energy Society Innovative Smart Grid Technologies Conference (ISGT)*, Washington, D.C., pp. 1-5, Feb. 2019. Copyright 2019, IEEE.

Instead of directly estimating phasor parameters, the proposed framework acknowledges that neither algorithm alone will yield satisfactory results. Algorithm A in this framework is leveraged as a filter with which some of the undesired features are removed from the input. The principle is, when the reconstructed waveform x' is a desirable replica of input waveform x, the same output from Algorithm A (filter) should be expected. Candidate methods from either frequency domain or time domain are selected for a simple demonstration of the proposed framework.

7.5.3.1 Monomial Fitting Method Used for Reconstruction

In this case, input signal measurement vector $x(t)$ are projected onto monomial basis,

$$\boldsymbol{\gamma}_i \overset{\text{def}}{=} \boldsymbol{t}^i \cos(2\pi f_0 \boldsymbol{t}), i = 0,1,2, \ldots M-1$$

$$\boldsymbol{\delta}_i \overset{\text{def}}{=} \boldsymbol{t}^i \sin(2\pi f_0 \boldsymbol{t}), i = 0,1,2, \ldots M-1$$

Denote $x'(\boldsymbol{t})$ as the reconstructed waveform measurement vector in M-dimensional vector space $\mathbb{M} = \text{span}\{\boldsymbol{\gamma}_i, \boldsymbol{\delta}_i\}, i = 0,1,2, \ldots M-1$. Then $x'(\boldsymbol{t})$ can be expressed in terms of the basis:

$$x'(\boldsymbol{t}) = H\boldsymbol{c} \tag{7.64}$$

where,

$$\begin{aligned} H &= [\boldsymbol{\gamma}_0, \boldsymbol{\delta}_0, \boldsymbol{\gamma}_1, \boldsymbol{\delta}_1, \boldsymbol{\gamma}_2, \boldsymbol{\delta}_2, \ldots, \boldsymbol{\gamma}_{M-1}, \boldsymbol{\delta}_{M-1}] \\ \boldsymbol{c} &= [c_0, s_0, c_1, s_1, c_2, s_2, \ldots, c_{M-1}, s_{M-1}]^{\mathrm{T}} \end{aligned} \tag{7.65}$$

Monomial fitting method represented in Equations (7.64) and (7.65) captures the slow varying dynamics in waveform envelopes with high accuracy, and therefore, we may assume $x(\boldsymbol{t}) = x'(\boldsymbol{t}) = H\boldsymbol{c}$ with acceptable fitting error. On the other hand, harmonic terms can be filtered out using Algorithm A (DFT in this case). Therefore, if waveform $x'(\boldsymbol{t})$ contains all the desired information in a particular application, using Algorithm A to filter either waveform $x(\boldsymbol{t})$ or waveform $x'(\boldsymbol{t})$ should yield the same results.

For Algorithm A, DFT calculation can be defined as:

$$X(\boldsymbol{k}) = Wx(\boldsymbol{t}) \tag{7.66}$$

where W is the DFT matrix, whose elements are determined by:

$$W_{m,n} = \frac{1}{\sqrt{N}} \omega^{mn}, \omega \equiv e^{-\mathrm{j}\frac{2\pi}{N}}, m, n = 0,1,2, \ldots, N-1 \tag{7.67}$$

$$x(\boldsymbol{t}) = s(\boldsymbol{t}) + h(\boldsymbol{t})$$

where $s(\boldsymbol{t})$ is the harmonic free signal, and $h(\boldsymbol{t})$ st the harmonic terms.

From the mathematical expression, it can be seen that each row of matrix W extracts one frequency component from input waveform. Due to the restriction of Nyquist theorem, up to half the sampling frequency can be extracted, the positive and negative images are actually complex conjugate pairs. Matrix W can be rearranged as shown in Equation (7.68):

$$W = \begin{bmatrix} A \\ W' \end{bmatrix}$$
$$A = \frac{1}{\sqrt{N}} \begin{bmatrix} 1 & \omega^{p} & \omega^{2p} & \cdots & \omega^{(N-1)p} \\ 1 & \omega^{N-p} & \omega^{2(N-p)} & \cdots & \omega^{(N-1)(N-p)} \end{bmatrix} \tag{7.68}$$

where p is the number of nominal cycles in an observation window. Since the only frequency components of interest are ±60Hz, only two rows associated with ±60Hz of matrix W are used, stored in matrix A.

Applying Fourier analysis W on $x(\boldsymbol{t})$:

$$Wx(\boldsymbol{t}) = \begin{bmatrix} A \\ W' \end{bmatrix} [s(\boldsymbol{t}) + h(\boldsymbol{t})] = \begin{bmatrix} As(\boldsymbol{t}) + Ah(\boldsymbol{t}) \\ W's(\boldsymbol{t}) + W'h(\boldsymbol{t}) \end{bmatrix} \tag{7.69}$$

The expression $Ax(\boldsymbol{t}) = As(\boldsymbol{t}) + Ah(\boldsymbol{t})$ yields the Fourier spectrum components of ±60Hz, which are in fact, complex conjugate. Since $h(\boldsymbol{t})$ does not contain any ±60Hz components, $Ah(\boldsymbol{t}) \equiv 0$. For the sake of simplicity, only ±60Hz component will be analyzed. As a result, matrix A instead of W is used for Fourier analysis.

As discussed before, Fourier analysis is performed on both the original waveform $x(\boldsymbol{t})$ and the reconstructed waveform $x'(\boldsymbol{t})$, and the results should be the same when reconstruction is assumed to be accurate. Thus, the following simple identity holds.

$$Ax'(\boldsymbol{t}) = AH\boldsymbol{c} \cong Ax(\boldsymbol{t}) = Af(\boldsymbol{t}) \coloneqq \boldsymbol{b} \tag{7.70}$$

where A is the DFT matrix extracting real and imaginary parts of ±60Hz components, H is defined in Equation (7.65). $x(\boldsymbol{t})$ is input waveform sample vector, $\boldsymbol{b}$ is the equivalent real and imaginary parts of ±60Hz complex conjugate components, $\boldsymbol{c}$ is the unknown vector of interest.

Equation (7.70) is the theoretical justification of proposed hybrid method where DFT is essentially used to reject harmonics. The same logic can also be applied when DFT is used as reconstruction function, as discussed in the following section.

7.5.3.2 DFT Used for Reconstruction

It should be noted that DFT is a curve fitting method as well, where the basis vectors are in fact harmonic components. Therefore, the formulation of this scheme should be essentially the same as in Section 7.5.3.1.

Consider reconstructed waveform $x'(\boldsymbol{t})$ with three frequency components, shown in Equation (7.71):

$$x'(\boldsymbol{t}) = M\boldsymbol{c} \tag{7.71}$$

where,

$$\begin{gathered} M = [\boldsymbol{m_0}, \boldsymbol{n_0}, \boldsymbol{m_1}, \boldsymbol{n_1}, \boldsymbol{m_2}, \boldsymbol{n_2}] \\ \boldsymbol{m_i} \coloneqq \cos(2\pi f_i \boldsymbol{t}) \\ \boldsymbol{n_i} \coloneqq -\sin(2\pi f_i \boldsymbol{t}) \\ \boldsymbol{c} \coloneqq [c_0, s_0, c_1, s_1, c_2, s_2]^{\mathrm{T}} \end{gathered} \tag{7.72}$$

where f_i are pre-selected frequencies that can be the output of spectrum analysis of input waveform. The case of three frequency components are selected here as an example. Polynomial fitting method is used as the filtering algorithm.

Similarly, we have:

$$\boldsymbol{d} \coloneqq H^{+}x(\boldsymbol{t}) \cong H^{+}M\boldsymbol{c} \tag{7.73}$$

where $H^{+} \equiv (H^{\mathrm{T}}H)^{-1}H^{\mathrm{T}}$ denotes pseudo-inverse of matrix H, as defined in Equation (6.73). Note that the column space of H is incomplete, since limited terms are used for expansion.

To demonstrate how to improve the accuracy of Equation (7.73), an analogous example in three-dimension is illustrated, shown in Figure 15. Assume vector $\boldsymbol{a}$ (blue arrow) is the "true" waveform vector in 3-D, which is practically observed and thus approximated in 2-D space $\mathbb{S} = \mathrm{span}\{\boldsymbol{i}, \boldsymbol{j}\}\}$. Note that, since $\boldsymbol{a} \notin \mathbb{S}$, approximation error from projection is inevitable. The effect of neglecting the rest of the basis in a complete space is discussed.

Denote the neglected base vector as $\boldsymbol{k}_1$ (red arrow), then the accurate projection of vector $\boldsymbol{a}$ should be:

$$\boldsymbol{a} = (\boldsymbol{i}, \boldsymbol{j}, \boldsymbol{k}_1) \cdot (i_1, j_1, k_1)^{\mathrm{T}}$$

When least square is used, an orthogonal complementary vector of $\mathbb{S}$, denoted as $\boldsymbol{k}_2$, is assumed instead, and the resultant projection would be:

$$\boldsymbol{a} = (\boldsymbol{i}, \boldsymbol{j}, \boldsymbol{k}_2) \cdot (i_2, j_2, k_2)^{\mathrm{T}}$$

Besides the error from vector space truncation when forming H matrix, more errors are introduced when utilizing a non-orthogonal fitting vector space.

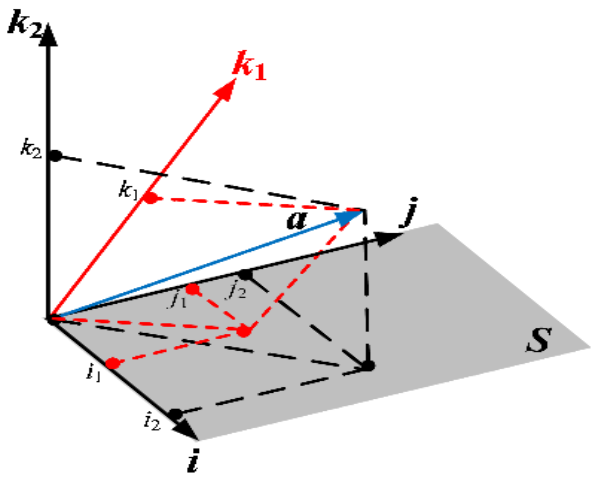

Figure 15 Illustration of least square approximation error.

As a result, it is important to find a vector space whose complementary space is orthogonal to it, and has the same column space as H. This is effectively done by QR factorization [105]-[106], expressed in Equation (7.74).

$$H = QR = [\hat{Q} \vdots Q_2]\begin{bmatrix}\hat{R}\\ \mathbf{0}\end{bmatrix} \tag{7.74}$$

where matrices $\hat{Q}$ and H have the same column space, which is orthogonal to the column space of matrix Q_2, and $Q^{-1} = Q^{\mathrm{T}}$. From this point, matrix $\hat{Q}$ will be used instead of H.

Rewrite Equation (7.73), since,

$$x(\boldsymbol{t}) = H\boldsymbol{d} = [\hat{Q}, Q_2]\begin{bmatrix}\hat{R}\\ \mathbf{0}\end{bmatrix}\boldsymbol{d} = [\hat{Q}, Q_2]\begin{bmatrix}\hat{R}\boldsymbol{d}\\ \mathbf{0}\end{bmatrix} \tag{7.75}$$

Therefore,

$$\begin{bmatrix}\hat{R}\boldsymbol{d}\\ \mathbf{0}\end{bmatrix} = ([\hat{Q}, Q_2])^{-1}x(\boldsymbol{t}) = ([\hat{Q}, Q_2])^{T}x(\boldsymbol{t}) = \begin{bmatrix}\hat{Q}^T\\ Q_2^T\end{bmatrix}x(\boldsymbol{t}) \tag{7.76}$$

Neglecting orthogonal complementary subspace Q_2, and rewrite Equation (7.73):

$$\hat{R}\boldsymbol{d} = \hat{Q}^T x(\boldsymbol{t}) = \hat{Q}^T M\boldsymbol{c} \tag{7.77}$$

Note that vector $\boldsymbol{d}$ is implicit, and does not need to be calculated. By utilizing QR factorization of fitting matrix H, extra approximation error from least square calculation is avoided.

7.6 Simulation Results

7.6.1 Fundamental Frequency Estimation

The proposed technique is implemented in MathWorks Simulink software. Sampling frequency is 6kHz. In order to evaluate the states at each time step, both EKF and UKF are used. Three sets of simulations are conducted to demonstrate better performance of UKF-based approach over EKF-based approach in the frequency estimation problem: EKF using three-phase measurements, UKF using three-phase measurements, UKF using single-phase measurement. The performance of the three cases are evaluated through metrics including optimality/bias, and sensitivity toward initial values.

7.6.1.1 Test Scenarios and Evaluation Metrics

To test the performance of the proposed approach in various power system operating conditions, both steady-state and dynamic-state waveforms are used in the simulation, including pure sinusoidal signals, steady-state signals with harmonic infiltration, amplitude-modulated signals, phase-modulated signals, and frequency ramping signals. Test signal parameters are determined based on IEEE standard. AWGN is added to pure sinusoidal signals, where the SNR is either 20dB or 40dB. The SNR is defined as:

$$\text{SNR} = 10 \cdot \log_{10}\left(\frac{\sigma^2_{\text{signal}}}{\sigma^2_{\text{noise}}}\right) = 20 \cdot \log_{10}\left(\frac{A_{\text{signal}}}{A_{\text{noise}}}\right) \tag{7.78}$$

where σ^2 is the variance, A is the RMS amplitude. Practically, A_{noise} is the standard deviation of noise, i.e., σ_{noise}.

As discussed before, since the system equation is highly nonlinear, neither EKF nor UKF will attain optimality in terms of achieving MMSE solutions. This sub-optimality condition will result in bias between estimated fundamental frequency and "true" theoretical frequency. Besides, the initial conditions consist of current step sample, previous step sample, and angular increment over one sampling interval (proportional to angular frequency). Depending on the initial conditions for states, the nonlinearity of state equations may lead to undesirable though mathematically valid solutions, if not causing divergence. Thus, the sensitivity to initial conditions should also be evaluated.

7.6.1.2 Simulations with 40dB AWGN Input

In this test scenario, 40dB SNR is associated with the signal uncertainty characterized by a standard deviation of 1% of the signal amplitude. The test signal is shown in Figure 16 (a) and (b).

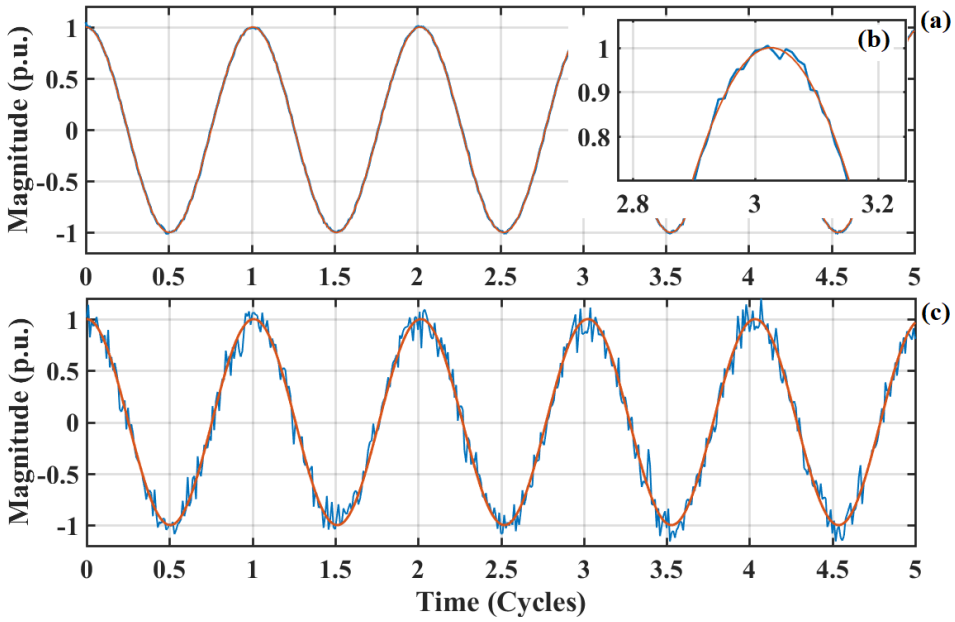

Figure 16 Test Waveforms: 59.5Hz pure cosine wave with noise infiltration. (a). Sinusoidal wave with 40dB AWGN. (b). Local Zoom-in of the Waveform in (a). (c). Sinusoidal wave with 20dB AWGN. Orange curves are noiseless signals.
Reprinted with permission from C. Qian and M. Kezunovic, "Power system fundamental frequency estimation using Unscented Kalman Filter," *2019 IEEE Power & Energy Society General Meeting (PESGM)*, Atlanta, GA, USA, pp. 1-5, Aug. 2019. Copyright 2019, IEEE.

- Frequency estimation bias:

Test results are shown in Table 1. It can be observed that highly accurate frequency estimation results can be achieved by using either single-phase or three-phase waveform measurements.

Table 1. Summary of Frequency Estimation for Input with 40dB AWGN
Reprinted with permission from C. Qian and M. Kezunovic, "Power system fundamental frequency estimation using Unscented Kalman Filter," *2019 IEEE Power & Energy Society General Meeting (PESGM)*, Atlanta, GA, USA, pp. 1-5, Aug. 2019. Copyright 2019, IEEE.

Case Details	UKF-Single Phase	UKF-Three Phase
Steady-state unbalanced	$< 5\times10^{-7}$ Hz	$< 5\times10^{-7}$ Hz
Steady-state harmonics	$< 5\times10^{-7}$ Hz	$< 5\times10^{-7}$ Hz
Amplitude modulation	$< 5\times10^{-7}$ Hz	$< 5\times10^{-7}$ Hz
Phase modulation	$< 5\times10^{-7}$ Hz	$< 5\times10^{-7}$ Hz
Frequency ramp	$< 5\times10^{-7}$ Hz	$< 5\times10^{-7}$ Hz

- Sensitivity to initial conditions:

As aforementioned, state x_3 is proportional to angular frequency $\omega = 2\pi f$, and its initial value is set to be nominal. States x_1 and x_2 are related to instantaneous sample values, and cannot be predicted, and thus are set arbitrarily to 1 p.u. In the test, the selected initial values may deviated from the "true" starting point of the system states in either frequency or amplitude. Fundamental frequency of input test signal ranges from 55Hz to 65Hz, with 1Hz increment. Besides, the amplitude deviation between selected initial conditions and "true" amplitude may be anywhere between -100% and 100%. EKF approach is tested as well to show the comparison. Test results are shown in Table 2.

Table 2. Summary of Sensitivity to Initial Conditions for Input with 40dB AWGN

Case Details	EKF-Three Phase	UKF-Three Phase
Frequency deviation ±1Hz to ±5Hz	Converge	Converge
Amplitude deviation ±50%	Diverge	Converge
Amplitude deviation ±25%	Diverge	Converge
Amplitude deviation ±10%	Converge	Converge

As can be observed, EKF-based approach may diverge when the selected initial values deviate more than 25% off the true values. In practice, this essentially means that the convergence depends on when the waveform samples are taken. There is at least 75% chance that EKF-based method may diverge. On the other hand, proposed UKF-based method will always converge.

7.6.1.3 Simulations with 20dB AWGN Input

In this test case, 20dB SNR is associated with the signal uncertainty characterized by a standard deviation of 10% of the signal amplitude. As can be seen in Figure 16 (c), the noise causes visibly significant distortion.

- Frequency estimation bias:

Test results are tabulated in Table 3. Compared to the 40dB noise input case, higher noise level increases frequency estimation bias by at least 10 times. Three-phase measurements improve estimation accuracy than single-phase measurements. Regardless, the estimation accuracy is still sufficiently high.

Table 3. Summary of Frequency Estimation Bias for Input with 20dB AWGN
Reprinted with permission from C. Qian and M. Kezunovic, "Power system fundamental frequency estimation using Unscented Kalman Filter," *2019 IEEE Power & Energy Society General Meeting (PESGM)*, Atlanta, GA, USA, pp. 1-5, Aug. 2019. Copyright 2019, IEEE.

Case Details	UKF-Single Phase	UKF-Three Phase
Steady-state unbalanced	$< 1\times10^{-5}$ Hz	$< 5\times10^{-6}$ Hz
Steady-state harmonics	$< 1\times10^{-6}$ Hz	$< 1\times10^{-6}$ Hz
Amplitude modulation	$< 5\times10^{-6}$ Hz	$< 2\times10^{-6}$ Hz
Phase modulation	$< 1\times10^{-6}$ Hz	$< 1\times10^{-6}$ Hz
Frequency ramp	$< 1\times10^{-6}$ Hz	$< 1\times10^{-6}$ Hz

- Sensitivity to initial conditions:

As shown in Table 4, similar to the 40dB noise input case, EKF-based approach is sensitive to the initial values of states x_1 and x_2. Consequently, there is at least 75% chance that EKF-based method does not converge.

Table 4. Summary of Sensitivity to Initial Conditions for Input with 20dB AWGN
Reprinted with permission from C. Qian and M. Kezunovic, "Power system fundamental frequency estimation using Unscented Kalman Filter," *2019 IEEE Power & Energy Society General Meeting (PESGM)*, Atlanta, GA, USA, pp. 1-5, Aug. 2019. Copyright 2019, IEEE.

Case Details	EKF-Three Phase	UKF-Three Phase
Frequency deviation ±1Hz to ±5Hz	Converge	Converge
Amplitude deviation ±50%	Diverge	Converge
Amplitude deviation ±25%	Diverge	Converge
Amplitude deviation ±10%	Converge	Converge

7.6.1.4 Influence of Sigma Point Selection on Estimation Bias

Due to the nonlinearity of state equations, the frequency estimation based on UKF will inevitably result in sub-optimal solutions, i.e., estimation biases. The tuning of UKF procedure, namely, the selection of parameters α, β, and κ in Equations (7.23)-(7.27) will affect frequency estimation results. This is summarized in Table 5. UKF-three phase test is used in this simulation, where this nominal frequency is 60.5Hz. The value shown in the table is the maximum estimation bias in all types of tests.

Table 5. Influence of Sigma Point Selection on Biases in Frequency Estimation
Reprinted with permission from C. Qian and M. Kezunovic, "Power system fundamental frequency estimation using Unscented Kalman Filter," *2019 IEEE Power & Energy Society General Meeting (PESGM)*, Atlanta, GA, USA, pp. 1-5, Aug. 2019. Copyright 2019, IEEE.

Case Details	20dB Noise	40dB Noise
$\alpha = 1 \times 10^{-3}$ $\beta = 2, \kappa = 0$	5×10^{-4} Hz	5×10^{-4} Hz
$\alpha = 0.1$ $\beta = 2, \kappa = 0$	$< 5\times10^{-7}$ Hz	$< 5\times10^{-7}$ Hz
$\alpha = 0.1$ $\beta = 4, \kappa = 0$	1.5×10^{-6} Hz	5×10^{-7} Hz
$\alpha = 0.1$ $\beta = 2, \kappa = 2$	5×10^{-7} Hz	5×10^{-7} Hz

It can be concluded that sigma points should be carefully selected to achieve lowest estimation uncertainties. Even though $\alpha = 1 \times 10^{-3}$ is recommended in papers [93]-[95], it can be seen that this choice does not provide best estimation result in the context of power system frequency estimation. In practice, measurement noise may not necessarily be Gaussian. As a result, β parameter should be tuned accordingly.

7.6.2 Phasor Parameter Calculation

7.6.2.1 Computational Time

The program is executed on an SEL-3355 substation computer, which is equipped with two quad-core CPUs operating at 2.1GHz. Totally 300,000 simulations are conducted, 100,000 for each phase. The computational times are recorded, and summarized in the histogram Figure 17.

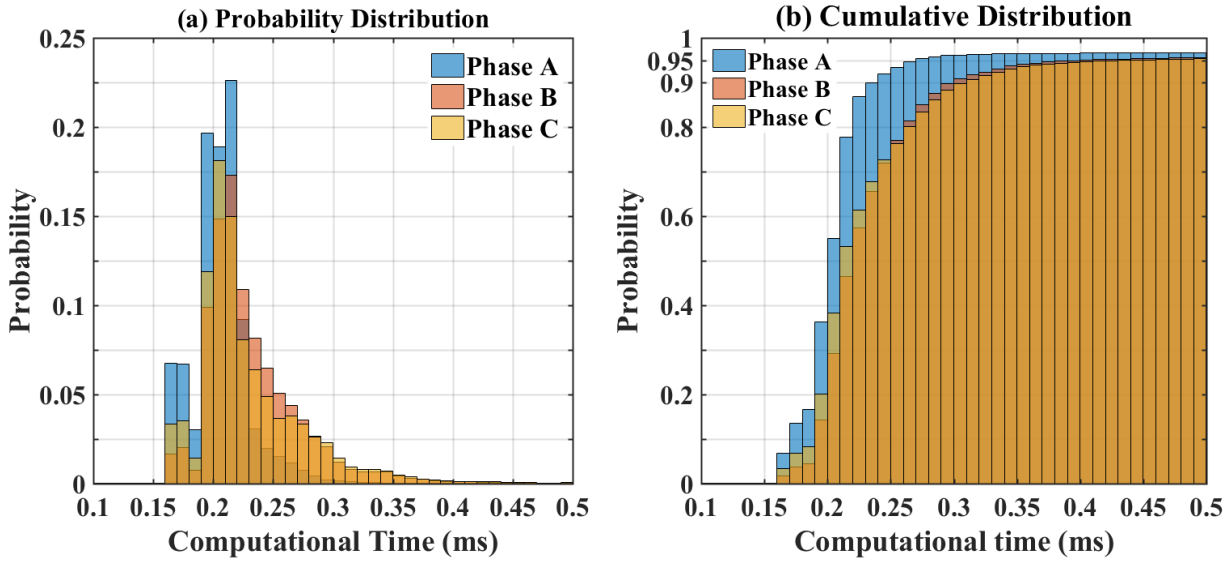

Figure 17 Histogram of phasor parameter calculation computational time.

As can be observed in Figure 17, over 90% of the computation can be completed within 0.35ms, which is less than 1/40 of the nominal cycle.

7.6.2.2 Computational Accuracy

The DFT-based method introduced in Section 7.4 and monomial fitting method are used in the demonstration of algorithm hybridization framework. In this test, waveforms containing both harmonics and slow amplitude transients are used as test waveforms. The sampling frequency is 6kHz, and hop size is 5 samples, and therefore data window length is one cycle plus 10 samples. 10% harmonic level is used.

- Curve Fitting Method Used for Reconstruction

In this case, slow transients are modeled directly while Fourier method is used to filter out harmonics. The results are shown in Table 6.

Table 6. Waveform Approximation Accuracy for Strategy I

TVE	f_{AM} = 1Hz	f_{AM} = 2Hz	f_{AM} = 5Hz
2nd Harmonic	4.2×10^{-5}%	6.5×10^{-4}%	2×10^{-2}%
5th Harmonic	4.2×10^{-5}%	6.5×10^{-4}%	2×10^{-2}%
10th Harmonic	4.2×10^{-5}%	6.5×10^{-4}%	2×10^{-2}%
30th Harmonic	4.2×10^{-5}%	6.5×10^{-4}%	2×10^{-2}%
50th Harmonic	4.2×10^{-5}%	6.5×10^{-4}%	2×10^{-2}%

It can be observed that at a certain amplitude modulation frequency level, the accuracy is not affected by harmonic order, which is expected since the harmonic components are filtered

out in the DFT-based method. The estimation errors are only from curve fitting procedure. Adding more terms in Equation (7.58) may improve the accuracy, but may also cause overfitting problem.

- Fourier Method for Used Reconstruction

In this simulation, besides N DFT harmonic components, two extra frequencies, 55Hz, 65Hz, are added to model the sidebands from amplitude modulation. The slow varying transients are further modeled in six monomial terms shown in Equation (7.58). The results are shown in Table 7.

Table 7. Waveform Approximation Accuracy for Strategy II

TVE	2nd Harmonic	13th Harmonic	35th Harmonic
f_{AM} = 1Hz	1.6×10^{-2}%	5×10^{-3}%	5×10^{-3}%
f_{AM} = 2.3Hz	6×10^{-2}%	2×10^{-2}%	2×10^{-2}%
f_{AM} = 3.4Hz	0.1×10^{-2}%	2×10^{-2}%	2×10^{-2}%
f_{AM} = 4.5Hz	5×10^{-2}%	1×10^{-2}%	1×10^{-2}%
f_{AM} = 5Hz	0	0	0

Since harmonics are still not completely filtered out, the estimation errors come from amplitude modulation sidebands. Because 55Hz and 65Hz only exactly model the sidebands at f_{AM} = 5Hz, estimation error cannot be completely eliminated otherwise. To alleviate the effect from sidebands, more frequencies in the vicinity of 60Hz can be potentially added in the Fourier model.

7.7 Conclusion

In this Chapter, the Dissertation tackles the problem of phasor parameter calculation under electromagnetic transient conditions. In order to mitigate the inherent limitations of DFT-based methods, i.e., frequency leakage and picket-fence effect, which happen when the actual signal fundamental frequency falls between DFT bins, we propose an UKF-based fundamental frequency estimator. With sufficient computational efficiency, the frequency estimator runs in the background of phasor parameter estimation, and provides the most recently system fundamental frequency update.

Then, a DFT-based algorithm that leverages the latest fundamental frequency value to adaptively tune its window size is proposed. The resultant phasor parameter calculation error caused by spectral leakage is further compensated. In order to mitigate the slow-varying process in electromagnetic waveforms, we propose a hybridization framework that incorporates the merits of both DFT- and curve-fitting-based phasor parameter calculation algorithms. The algorithm accurately captures 60Hz phasor parameters, while mitigating the impact of slow-varying decaying DC as well as harmonic infiltration on algorithm accuracy. The performance of the phasor parameter calculation algorithm is validated in MATLAB simulations.

8. POWER WAVEFORM CLASSIFICATION TOOL AND PHASOR PARAMETER CALCULATION DURING ELECTROMECHANICAL TRANSIENTS [*]

8.1 Introduction

In the electric power system, synchronous machine rotors do not rotate strictly at the same speed. In the power network, as a result, the features of the power signals, e.g., electrical quantities, appear to be modulated.

Under normal operating conditions, the mismatch among synchronous machine speeds is small, and the variations in electrical quantities appear to be randomized and tolerable. A large disturbance in the power grid, on the other hand, may cause significant excursions of vital electric properties of the power grid, such as phase angle separation [15],[107], frequency [108], active/reactive powers [12]-[13]. This abnormal deviation may end up in catastrophic results, such as large scale blackouts [13]-[14]. The properties of the modulation phenomena depends on the dynamic mechanical behavior of rotors, i.e., acceleration, deceleration, rotor speed drifting, etc. The interaction among rotors is established via magnetic coupling between rotor magnetic fields and electric network circuits.

---

[*] Reprinted with authors' permission from: (1) C. Qian and M. Kezunovic, "Synchrophasor reference algorithm for PMU Calibration System," *2016 IEEE/PES Transmission and Distribution Conference and Exposition (T&D)*, Dallas, TX, pp. 1-5, May 2016. Copyright 2016, IEEE. (2) C. Qian and M. Kezunovic, "Dynamic synchrophasor estimation with modified hybrid method," *2016 IEEE Power & Energy Society Innovative Smart Grid Technologies Conference (ISGT)*, Minneapolis, MN, pp. 1-5, Sep. 2016. Copyright 2016, IEEE. (3) C. Qian and M. Kezunovic, "A novel time-frequency analysis for power system waveforms based on "pseudo-wavelets"," *2018 IEEE/PES Transmission and Distribution Conference and Exposition (T&D)*, Denver, CO, pp. 1-9, Apr. 2018. Copyright 2018, IEEE. (4) C. Qian and M. Kezunovic, "A power waveform classification method for adaptive synchrophasor estimation," in *IEEE Transactions on Instrumentation and Measurement*, vol. 67, no. 7, pp. 1646-1658, Jul. 2018. Copyright 2018, IEEE.

The electromechanical dynamic events and their waveform characterizations are introduced in Chapter 5. It is shown that electromechanical dynamic waveforms are event-dependent. In order to effectively characterize electromechanical dynamic events, it is imperative that the features manifested in each event is represented in signal modeling accordingly [109].

In this Chapter, it is proposed that phasor parameters should be individually defined for different electromechanical dynamic events, so that the features of electrical quantities can be effectively reflected for each type of dynamic event. Besides, the signal models in algorithms should be tailored to match the corresponding waveform of dynamic events, so that the accuracy of curve-fitting can be maximized. In order to achieve such adaptive matching between algorithms and dynamic waveform, it is proposed that dynamic events should first be classified based on the time-frequency dynamic features of their waveform manifestations.

8.2 Overview on Time-Frequency Analysis Techniques

The classification of waveforms and corresponding dynamic events are accomplished by labeling the waveform measurements based on their features on both time and frequency scales.

8.2.1 General Discussion on Time-Frequency Analysis on a Waveform

A generalized notion is that signals carry information, which can be extracted and identified using signal processing techniques, such as shown in applications [110]-[113]. In this Dissertation, waveform features are leveraged to differentiate and classify waveforms, so that more accurate phasor parameter calculation algorithms can be subsequently switched for each dynamic waveform. Discussed below is how the selection of feature relates to the physical phenomena of power system.

In the electric power system, various types of electromechanical dynamic events are determined by the patterns in the movement of rotors and electrical quantities. For example, the oscillatory behavior between groups of synchronous machine rotors due to lack of damping torque is manifested as modulations on signal magnitude and/or signal frequency. In other words, what differentiates various types of dynamic events is the differences in the features of electrical quantities manifested in a duration of time.

Furthermore, since the electric power energy is generated through the rotation of synchronous machine rotors, the repetition of patterns, i.e., periodicity, is an inherent property of power system waveforms. Periodicity is conventionally represented by frequency, which is defined as the number of times a pattern repeats itself in unit time. Frequency can also be considered as a scaling factor, by which a 1Hz waveform pattern, e.g., mother wavelet, is "compressed" or "stretched". In this sense, frequency is perceived as a *scaling factor*. For example, when the "frequency" of a signal is 60Hz, it can be practically considered as compressing a 1Hz sinusoidal signal by a factor of 60. This notion is depicted in Figure 18.

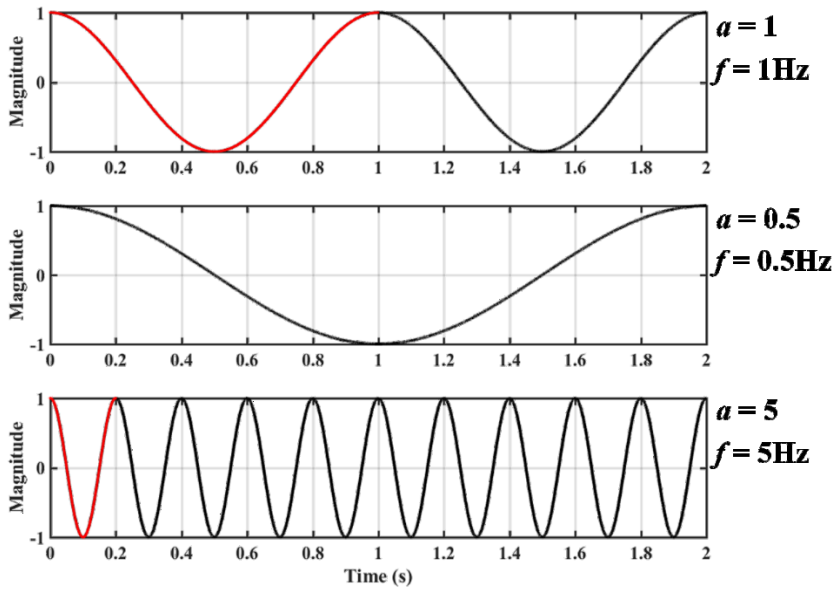

Figure 18 Illustration of the interpretation of scaling in lieu of frequency in sinusoidal waveforms

It is worth noting that, 1Hz (=1/1second) is not necessarily associated with 1 second of *sinusoidal* signal, but rather any kind of *arbitrary pattern*, e.g., "mother wavelet". Therefore, scaling factor may be used as a generalized term for frequency.

To summarize, the scale is used interchangeably with frequency, when the unit scale is defined in reference to a 1Hz pattern. Accordingly, in the analysis of power system waveforms, the pattern as well as the corresponding scale should also be incorporated in describing the features of a power system waveform, as generalized in Equation (8.1):

$$\gamma: [\boldsymbol{t}, x(\boldsymbol{t})] \mapsto \gamma[\boldsymbol{t}, a; \psi_a(\boldsymbol{t})] \tag{8.1}$$

where γ is the quantified feature, vector $\boldsymbol{t}$ is the duration of time under analysis, $\psi_a(\boldsymbol{t})$ is the arbitrarily defined pattern to which the repetition of waveform is compared and referenced, a is the scaling factor. Equation (8.1) denotes that an input time signal $x(\boldsymbol{t})$ is interpreted in terms of its

relationship with pattern $\psi_a(\boldsymbol{t})$ and scaling factor a in time, and this interpretation is enabled by a mapping function γ.

The question now is how to design a pattern $\psi_a(t)$ and a mapping calculation γ so that the coefficients $\gamma[\boldsymbol{t}, \psi_a(\boldsymbol{t})]$ are meaningful in differentiating waveform types. Among the various time-frequency techniques, STFT and wavelet analysis are discussed in the following sections to provide the background of the newly designed method.

8.2.2 Short-Term Fourier Transforms

STFT, defined in Equation (8.2), interprets the signal in terms of its sinusoidal components and the progression of those sinusoidal components w.r.t time [68],[114]-[115].

$$\text{STFT}\{x[\boldsymbol{n}]; w[\boldsymbol{n}]\}(m,k): x[\boldsymbol{n}] \longmapsto X(m,k)$$

$$X(m,k) = \sum_{n=-\infty}^{\infty} x[n]w[n-m]e^{-\mathrm{j}\frac{2\pi}{N}kn}, \text{for } k \in \left(-\left\lfloor\frac{N}{2}\right\rfloor, \left\lceil\frac{N}{2}\right\rceil - 1\right) \tag{8.2}$$

where $x[\boldsymbol{n}]$ is the discretized input waveform data window, $w[\boldsymbol{n}]$ is the window function, $X(m,\omega)$ represents the STFT results, m is the shift index, k is the harmonic order w.r.t. to DFT fundamental frequency, N is the number of samples in a DFT calculation, and $N \leq \dim(x[\boldsymbol{n}])$.

In the calculation of STFT, the input data window will first be truncated into frames. The samples associated with each frame, characterized by shift index, will then be analyzed by DFT/FFT, resulting in spectrum $X(m, \boldsymbol{k})$. With multiple shift indices in the calculations, the resultant vectors will be added to a matrix, $X(\boldsymbol{m}, \boldsymbol{k})$. Each element in the matrix, i.e., $X(m,k)$, represents the complex DFT value of the kth harmonic component in the waveform $x(m, m+N)$. $2\pi/N$ is the resolution of DFT.

STFT is most commonly used to generate spectrograms, which is defined as:

$$\text{spectrogram}\{x[\boldsymbol{n}]\}(m,k) \equiv \|X(m,k)\|_2^2 \tag{8.3}$$

One of the pitfalls of STFT is that time resolution and frequency resolution cannot be simultaneously high. Specifically, denote f_s as the sampling frequency, then the frequency resolution of STFT is f_s/N in Hz, and the time resolution is N/f_s. This means that it is theoretically not possible to observe an abrupt change in frequency composition while attaining the details of that frequency profile. This restriction is also characterized formally as the Heisenberg-Gabor limit [116]. Furthermore, STFT only allows fixed time-frequency resolution in a single STFT analysis. Once the STFT parameters are chosen, the time-frequency plain is gridded according to the predetermined time and frequency resolutions. The value of coefficient on each grid is evaluated according to Fourier Transform.

As shown in Figure 19, the STFT results with three different pairs of frequency and time resolution are presented. The input signal features an abrupt change in harmonic frequency profile at 1 second. Before $t = 1$s, the signal is composed of 60Hz, 3rd, 5th, 18th, and 20th harmonics; and after $t = 1$s, the signal components change to 60Hz, 3rd, 7th, 15th, and 19th harmonics. Intuitively, the height of each horizontal stripe represent frequency resolution: the narrower the stripe, the more effective STFT is able to pinpoint the exact frequency component. On the other hand, the vertical stripe at around 1 second represents the transient period during which the frequency profile of input signal changes. A shorter DFT window is more effective in terms of locating the instant when an event occurs.

Figure 19 demonstrates that STFT is not able to simultaneously pinpoint an event onset and frequency composition. The restriction fundamentally stems from the uncertainty principal associated with Fourier methods.

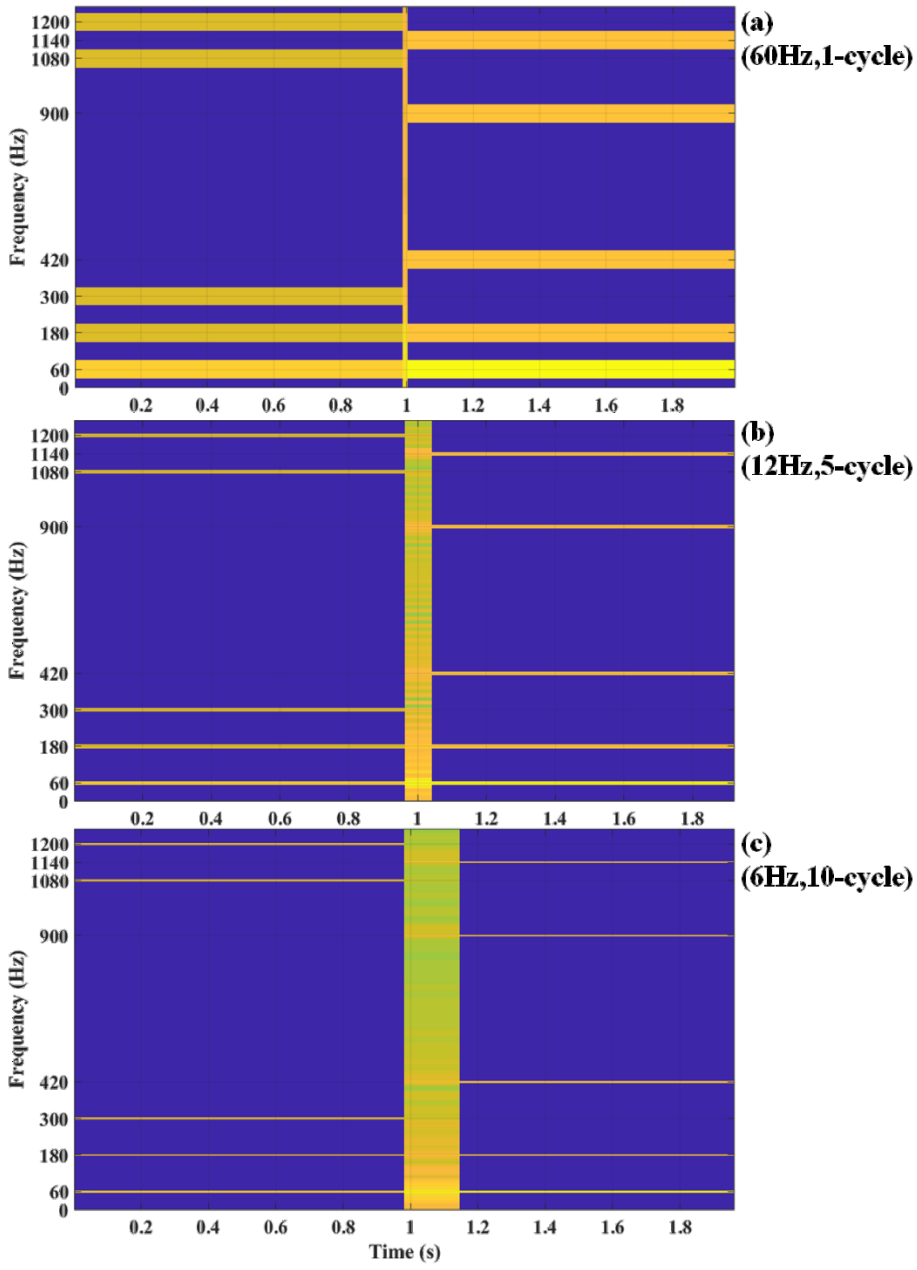

Figure 19 STFT analysis on a signal with harmonic infiltration and abrupt amplitude change at time 1s.
Results of various options of time-frequency resolution pairs are shown, as indicated on the figure.

8.2.3 Multiresolution Analysis and Wavelet Analysis

With multiresolution analysis techniques, it is feasible to achieve high time resolution and frequency resolution in one single analysis. This is achieved, however, at the expense of redundant calculation, which increases computational burden [117]-[120].

As the name indicates, multiresolution analysis gives interpretation of a waveform on multiple time and frequency resolution pairs. As opposed to STFT, where the time-frequency resolution grid is fixed once its parameters are chosen, multiresolution analysis tools, notably the wavelet transforms, introduce freedom in choosing the exactly time and frequency (scale) details of interest.

Multiresolution analysis is achieved by applying various types of wavelet transforms, such as continuous wavelet transform (CWT), discrete waveform transform (DWT), and fast wavelet transform (FWT) [121]-[122]. CWT is defined in Equation (8.4). In CWT, a section of the waveform, $x(t)$, is compared with an arbitrarily formulated wavelet signal, $\psi(t)$, termed mother wavelet. The mother wavelet has limit time support on $[0, T]$, and thus acts as a truncating window function. The child wavelet, $\psi_{a,b}(t)$, is derived from the mother wavelet, and is characterized by two independent parameters, a and b, as defined in Equation (8.5) below. As a result of the linear transformation, child wavelet $\psi_{a,b}(t)$ has support over $[b, b + aT]$. Parameter a is the scaling factor. When $a > 1$, mother wavelet is dilated; when $a < 1$, the mother wavelet is contracted. Parameter b is the time-shift factor. In a causal system, $b > 0$, moving the mother wavelet further away from time zero.

CWT is an integral transform with kernel $\psi_{a,b}(t)$. More specifically, CWT calculates the correlation factor between $x(t)$ and $\psi_{a,b}(t)$ associated with parameter pair (a, b), which intuitively quantifies the "resemblance" between the two signals.

$$\mathbb{CWT}(x, a, b) = \frac{1}{\sqrt{|a|}} \int_{-\infty}^{\infty} x(t) \psi_{a,b}^{*}(t) \mathrm{d}t \tag{8.4}$$

$$\psi_{a,b}(t) \stackrel{\text{def}}{=} \psi(\frac{t-b}{a}) \tag{8.5}$$

Since the same waveform is analyzed repeatedly with children wavelets characterized by multiple (a, b) selections, CWT is a redundant transform. Due to this redundancy, CWT is able to provide much more detailed descriptions of the compositions of input waveforms. Moreover, the result of CWT depends on the selection of the mother wavelet. Whether a chosen mother wavelet can or cannot extract useful information of an input waveform should be empirically studied. As shown in Figure 20, Morlet wavelet [123] is used to analyze various types of waveform inputs. It can be observed from the figure that Morlet wavelet is not adequate in extracting the features that differentiate different types of waveforms. Similarly, it has been proven in lab simulations that the conventionally used mother wavelets are not able to facilitate the differentiation of power system waveform, and a new wavelet should be designed for this purpose.

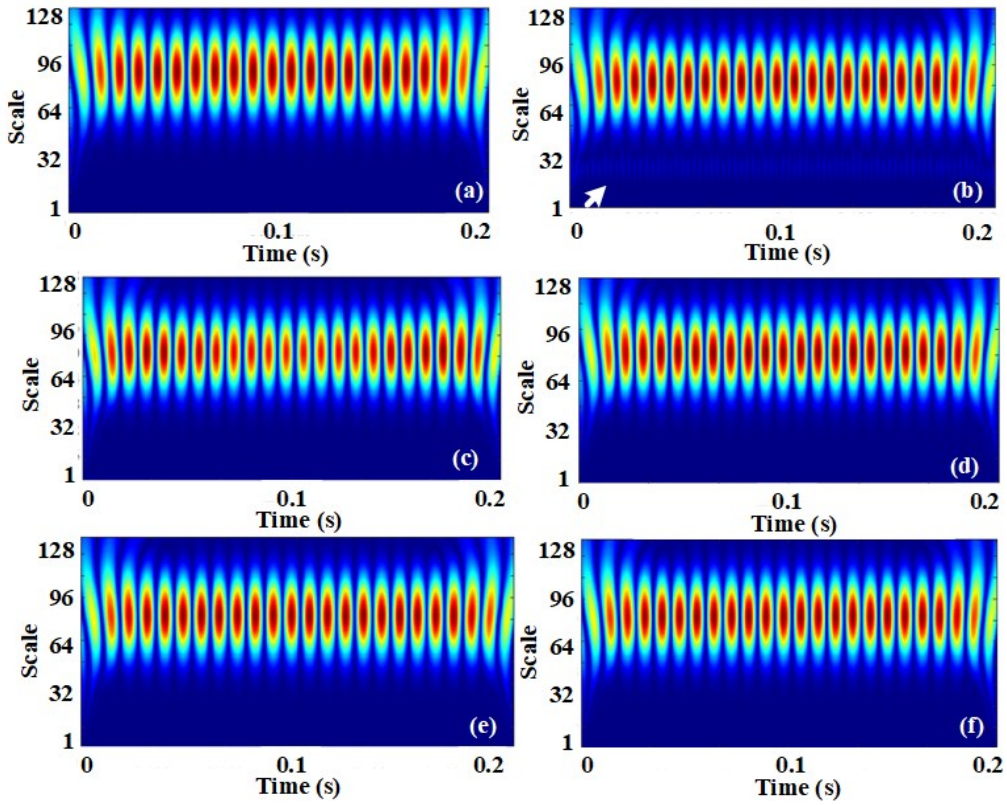

Figure 20 Results of continuous wavelet transform using Morlet wavelet on various inputs. (a) steady-state 65Hz, (b) steady-state 60Hz and 5th harmonic (arrow showing the harmonic component), (c) Amplitude modulation, (d) Frequency modulation, (e) Frequency ramp at 1Hz/s, (f) Frequency ramp at -1Hz/s

8.3 Proposed Multiresolution Analysis Using “Pseudo-Wavelets”

In this Dissertation, a novel mother wavelet is proposed [124]-[125] to more effectively extract time-frequency features from power system waveforms.

8.3.1 Proposed “Pseudo-Wavelet”

The power system waveforms, as previously stated, can be expressed as follows:

$$x(t) = a(t) \cdot \cos\left[2\pi \int f(t)\,\mathrm{d}t + \phi_0\right] + h(t) + u(t) \tag{8.6}$$

where $a(t)$ is the instant amplitude, $f(t)$ is the instant frequency, ϕ_0 is initial phase angle, $h(t)$ is the collective effect of (inter)harmonic components, and $u(t)$ represents uncertainty sources, such as noise.

Define mother wavelet $\vartheta(t)$and children wavelet $\vartheta_{a,b}(t)$,

$$\vartheta(t) = \cos(2\pi \cdot 1 \cdot t), t \in [0,1] \tag{8.7}$$

$$\vartheta_{a,b}(t) = \vartheta(\frac{t-b}{a}) \tag{8.8}$$

$\vartheta(t)$ is simply a single-cycle cosine wave at frequency $f_{\mathrm{pw}} \equiv 1/T_{\mathrm{pw}}$ (Hz). In order to differentiate from conventional mother wavelets, in this Dissertation, $\vartheta(t)$ is termed "pseudo-wavelet", and the parameters associated with pseudo-wavelet are marked with subscript $(*)_{\mathrm{pw}}$.

Define an integral transform $f(x; a, b)$, such that,

$$\begin{gathered} f: (x; a, b) \mapsto \gamma(x; a, b) \\ \gamma(x; a, b) = \int_{-\infty}^{\infty} x(t)\vartheta(\frac{t-b}{a})\mathrm{d}t \end{gathered} \tag{8.9}$$

would yield coefficients $\gamma(x; a, b)$ that represents the time-frequency feature of $x(t)$. The transform $f(x; a, b)$ is uniquely determined by factors a and b.

Analogous to CWT representation, a stands for scaling factor, and b stands for time-shift factor. Since mother wavelet $\vartheta(t)$ is defined in reference to a pure 1Hz sinusoidal wave, children wavelet $\vartheta_{a,b}(t)$ with scale a can be equivalently interpreted in terms of frequency.

$$\vartheta_{a,b}(t) = \cos\left(2\pi \frac{1}{a} t - \frac{2\pi b}{a}\right) \tag{8.10}$$

This is equivalent to defining the children wavelet $\vartheta_{a,b}(t)$ in terms of frequency and phase angle.

$$\vartheta(t;\tau,f_{\mathrm{pw}}) = \cos(2\pi f_{\mathrm{pw}} t + \tau) \tag{8.11}$$

where $f_{\mathrm{pw}} \equiv 1/a$, and $\tau \equiv -2\pi b/a$.

Given a data sample window, the lowest f_{pw} value corresponds to the scenario when $\vartheta(t)$ spans exactly the entire data window. The effect of scaling factor a is perceived in terms of frequency of the sinusoidal $\vartheta_{a,b}(t)$; and the phase shift of $\vartheta_{a,b}(t)$ is treated as the time-shift of $\vartheta_{a,b}(t)$ w.r.t. $\vartheta(t)$. Note that $\vartheta(t;\tau,f_{\mathrm{pw}})$ only has finite support over the range of $[\tau, \tau + T_{\mathrm{pw}}]$, where $T_{\mathrm{pw}} \equiv 1/f_{\mathrm{pw}}$. This scheme can be shown in Figure 21.

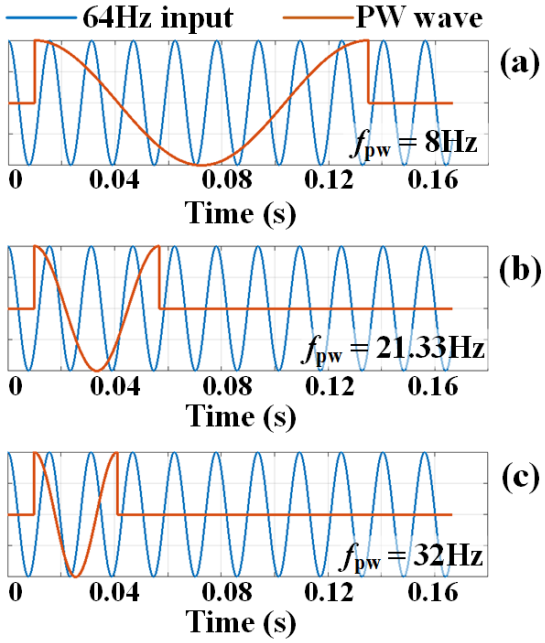

Figure 21 Illustration of correlation intensity at time lag 0.01s.
(a)-(c) Waveforms of 64Hz input and pseudo-wavelets at 8Hz, 21.33Hz, 32Hz, respectively. Reprinted with permission from C. Qian and M. Kezunovic, "A power waveform classification method for adaptive synchrophasor estimation," in *IEEE Transactions on Instrumentation and Measurement*, vol. 67, no. 7, pp. 1646-1658, Jul. 2018. Copyright 2018, IEEE.

As a result, in order to more explicitly show the operation of pseudo-wavelet, equation is expressed equivalently as,

$$\gamma(\tau, f_{\mathrm{pw}}) = \int_{-\infty}^{\infty} x_1(t)\vartheta(t;\tau,f_{\mathrm{pw}})\mathrm{d}t \tag{8.12}$$

where $\vartheta(t;\tau,f_{\mathrm{pw}})$ is the child pseudo-wavelet with frequency f_{pw} and time-shift of τ.

8.3.2 Time-Frequency Analysis Using Proposed "Pseudo-Wavelet"

According to Fourier theory, any input signal $x(t)$ can be decomposed as the summation of an infinite number of sinusoidal waves,

$$x(t) = \int_{-\infty}^{\infty} X(f)e^{\mathrm{j}2\pi ft}\mathrm{d}f = \lim_{\Delta f\to 0}\sum_{k=-\infty}^{\infty} X(k\Delta f)e^{\mathrm{j}2\pi k\Delta ft}\cdot\Delta f \tag{8.13}$$

As previously discussed, in power system signals, the waveform feature of interest is the periodic pattern in the waveform, as well as their characteristics of progression in time. In the following discussion, for the sake of simplicity, the interaction between only one single-tone frequency component in $x(t)$, denoted as $x_1(t)$, and $\vartheta(t)$ is analyzed. $x_1(t)$ has frequency f_1, which is unknown prior to analysis. Moreover, instead of moving pseudo-wavelet along the t-axis, shown as $\vartheta(t;\tau,f_{\mathrm{pw}})$, in the following analysis, $x_1(t)$ will be moved, and this only affects the apparent phase angle ϕ_0. As a result, Equation (8.12) can be further simplified as,

$$\gamma(\tau, f_{\mathrm{pw}}) = \int_{0}^{T_{\mathrm{pw}}} x_1(t+\tau)\vartheta(t,f_{\mathrm{pw}})\mathrm{d}t \tag{8.14}$$

The evaluation of $\gamma(\tau, f_{\mathrm{pw}})$ is shown as follows. Considering a particular pair (τ, f_{pw}), $x_1(t) = \cos(2\pi f_1 t + \phi_1)$, and $\vartheta(t, f_{\mathrm{pw}}) \equiv \cos(2\pi f_{\mathrm{pw}} t)$. The integration

$$\gamma(f_1;\tau,f_{\mathrm{pw}}) = \int_{0}^{T_{\mathrm{pw}}} \cos(\omega_1 t + \omega_1\tau + \phi_1)\cos(\omega_{\mathrm{pw}} t)\mathrm{d}t \tag{8.15}$$

where $\omega_1 \equiv 2\pi f_1$, $\omega_{\mathrm{pw}} \equiv 2\pi f_{\mathrm{pw}}$. Denote $\phi_1' \equiv \omega_1 \tau + \phi_1$. Using trigonometric properties, Equation (8.15) can be broken down as,

$$\gamma(f_1; \phi_1', f_{pw}) = \frac{1}{2}\int_0^{T_{\mathrm{pw}}} \cos\left[\left(\omega_1 + \omega_{\mathrm{pw}}\right)t + \phi_1'\right]\mathrm{d}t + \frac{1}{2}\int_0^{T_{\mathrm{pw}}} \cos\left[\left(\omega_1 - \omega_{\mathrm{pw}}\right)t + \phi_1'\right]\mathrm{d}t \tag{8.16}$$

Depending on the value of $\left(\omega_1 - \omega_{\mathrm{pw}}\right)$, the evaluation of Equation (8.16) can be discussed as follows:

Scenario 1: $\omega_1 - \omega_{\mathrm{pw}} = 0$:

Equation (8.16) can be simplified as:

$$\gamma(\omega_1, \tau) = \frac{1}{2}\left[\int_0^{T_{\mathrm{pw}}} \cos(2\omega_1 t + \phi_1')\mathrm{d}t + \int_0^{T_{\mathrm{pw}}} \cos\phi_1'\mathrm{d}t\right] = \frac{T_{\mathrm{pw}}}{2}\cos\phi_1' = \frac{\pi}{\omega_{\mathrm{pw}}}\cos\left(\omega_{\mathrm{pw}}\tau + \phi_1\right) \tag{8.17}$$

The first integral is zero since $2\omega_1 \equiv 2\omega_{\mathrm{pw}}$ and the integration on 2nd harmonic over a period is zero.

Scenario 2: $\omega_1 - \omega_{\mathrm{pw}} \neq 0$:

$$\gamma(\omega_1, \phi_1') = \frac{\sin\left(\omega_1 T_{\mathrm{pw}} + \phi_1'\right) - \sin\phi_1'}{2\left(\omega_1 + \omega_{\mathrm{pw}}\right)} + \frac{\sin\left(\omega_1 T_{\mathrm{pw}} + \phi_1'\right) - \sin\phi_1'}{2\left(\omega_1 - \omega_{\mathrm{pw}}\right)} = \left[\sin\left(\omega_1 T_{\mathrm{pw}} + \phi_1'\right) - \sin\phi_1'\right]\frac{\omega_1}{\omega_1^2 - \omega_{\mathrm{pw}}^2} \tag{8.18}$$

Note that ω_1 is unknown to the observer.

8.3.3 Further Discussion on Wavelet Analysis Result γ

Applying l'Hôpital's rule [126], the limit of Equation (8.18) as $\omega_1 \to \omega_{\mathrm{pw}}$ can be evaluated. Note that, $\omega_{\mathrm{pw}} T_{\mathrm{pw}} \equiv 2\pi$:

$$\lim_{\omega_1 \to \omega_{\mathrm{pw}}} \gamma = \lim_{\omega_1 \to \omega_{\mathrm{pw}}} \frac{\left[\sin\left(\omega_1 \frac{2\pi}{\omega_{\mathrm{pw}}} + \phi_1'\right) - \sin\phi_1'\right]\omega_1}{\omega_1^2 - \omega_{\mathrm{pw}}^2}$$

$$= \lim_{\omega_1 \to \omega_{\mathrm{pw}}} \frac{\omega_1 T_{\mathrm{pw}} \cos\left(\omega_1 T_{\mathrm{pw}} + \phi_1'\right)}{2\omega_1} + \lim_{\omega_1 \to \omega_{\mathrm{pw}}} \frac{\sin\left(\omega_1 T_{\mathrm{pw}} + \phi_1'\right) - \sin\phi_1'}{2\omega_1} \qquad (8.19)$$

$$= \frac{T_{\mathrm{pw}}}{2}\cos\phi_1' = \quad \text{r.h.s. of equation (8.17)}$$

To conclude, the evaluation of (8.15) can be compactly expressed using (8.19), when the limit value at $\omega_1 = \omega_{\mathrm{pw}}$ is specified. The zeros of (8.19) are acquired by solving $\left[\sin\left(\omega_1 T_{\mathrm{pw}} + \phi_1'\right) - \sin\phi_1'\right] \cdot \omega_1 = 0, \omega_1 \neq \omega_{\mathrm{pw}}$:

$$\omega_1 = k\omega_{\mathrm{pw}}, k = 0,2,3,4, \ldots, \omega_{\mathrm{pw}} \geq \omega_{\mathrm{spw,min}} \equiv \frac{2\pi}{T_{\mathrm{window}}} \qquad (8.20)$$

or,
$$\omega_1 = \frac{(2k+1)\pi - 2\phi_1}{T_{\mathrm{pw}} + 2\tau}, k = 0,1,2,3, \ldots \qquad (8.21)$$

where T_{window} is the length of data observation window in seconds. $\omega_{\mathrm{pw,min}}$ corresponds to the situation where only one cycle of cosine wave spans the entire window length.

Based on Equations (8.20) and (8.21), the evaluation of integral (8.15) will be zero when the pseudo-wavelet frequency value ω_{pw} is zero (trivial case), or the integer fractions of the actual (unknown) signal frequency. Due to this behavior of correlation coefficient $\gamma(\tau, f_{\mathrm{pw}})$, when tracking the zeros of $\gamma(\tau, f_{\mathrm{pw}})$, the focus should be on the frequencies around the integer fractions of 60Hz. For instance, as shown in Figure 22, is the correlation coefficient at lag $\tau = 0.01\mathrm{s}$. When the input waveform is a steady sinusoidal wave at 64Hz, correlation intensities will be zero at frequencies 32Hz, 21.33Hz, 16Hz, 12.8Hz, 10.67Hz, 9.14Hz, 8Hz, 7.11Hz, and 6.4Hz. In this case, since 10 nominal cycles of data are used, the minimal PW frequency is 6Hz. The scale of frequency axis is adjusted to show details at lower frequencies.

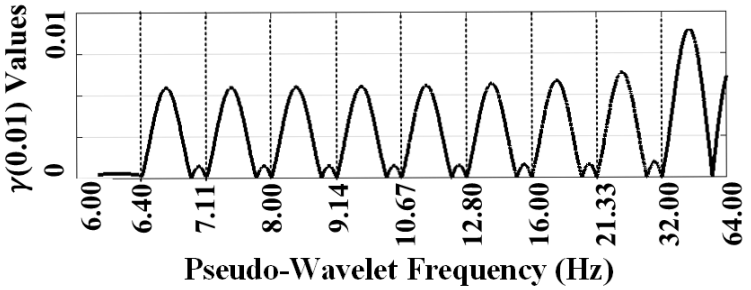

Figure 22 Illustration of correlation intensity at time lag $\tau = 0.01$s, $\gamma(0.01)$. Reprinted with permission from C. Qian and M. Kezunovic, "A power waveform classification method for adaptive synchrophasor estimation," in *IEEE Transactions on Instrumentation and Measurement*, vol. 67, no. 7, pp. 1646-1658, Jul. 2018. Copyright 2018, IEEE.

Moving $\gamma(\tau, f_{\text{pw}})$ along time axis while computing the correlation intensity using Equation (8.15) w.r.t. all the pseudo-wavelet frequency component. With the values of $\gamma(\tau, f_{\text{pw}})$ calculated, a matrix $\boldsymbol{\Gamma}$ can be thereafter formed, with its elements being $\gamma(\tau, f_{\text{pw}})$.

Shown in Figure 23 is a simple illustration for the aforementioned example, with time lag from 0 to 0.16s. Geometrically, given input signal, $\boldsymbol{\Gamma}$ is visualized as a surface, with x-axis being time lag τ, y-axis being PW frequency f_{pw}, and z-axis being the value of $\gamma(\tau, f_{\text{pw}})$. When projected onto $\tau - f_{\text{pw}}$ plain, correlation intensity, the absolute value of $\boldsymbol{\Gamma}$, can be depicted as brightness in Figure 23 (a) and (b), or contours in Figure 23 (c) and (d). As can be seen, the regions of low values of $\boldsymbol{\Gamma}$ form distinct "zero-bands", indicated by red dotted lines.

It is worth mentioning that the proposed method is not designed for accurate frequency estimation, since the correlation integral is merely an approximation, and its accuracy depends on the selected sampling interval and data window length. However, the accuracy of such calculation is sufficient for the purpose of input waveform classification. In obtaining the zero-band frequencies, Equation (8.19) is a sufficient, but not necessary condition. As shown in Figure 22,

$\gamma(\tau = 0.01, f_{\mathrm{pw}})$ may achieve zero values at frequencies other than the integer fractions of 64Hz.

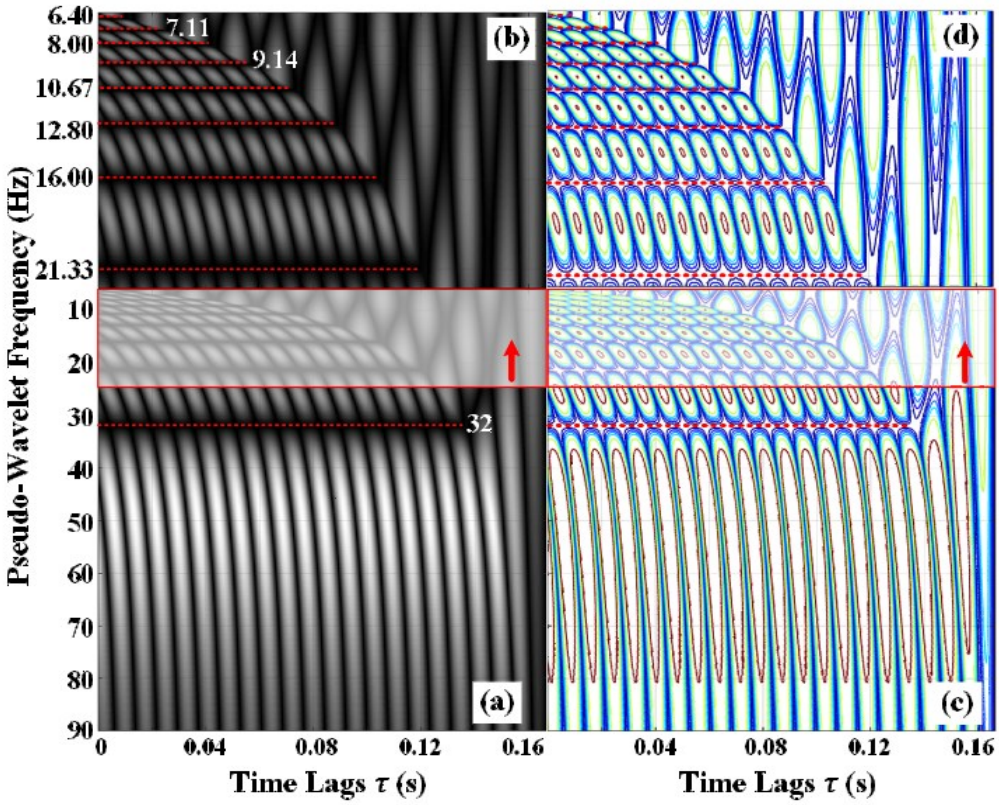

Figure 23 Pseudo-wavelet analysis result on 64Hz signal.
(a) Intensity projection, (b) Zoomed-in intensity projection, (c) Intensity contours, (d) Zoomed-in intensity contours.
Reprinted with permission from C. Qian and M. Kezunovic, "A power waveform classification method for adaptive synchrophasor estimation," in *IEEE Transactions on Instrumentation and Measurement*, vol. 67, no. 7, pp. 1646-1658, Jul. 2018. Copyright 2018, IEEE.

8.3.4 Matrix Formulation of Pseudo-Wavelet Transform

In the description of wavelet transform, it is implied that the correlation coefficients are calculated in an iterative manner, where γ associated with each scaling factor and time-shift is

calculated at each iteration. In practice, the matrix $\boldsymbol{\Gamma}_{i,j} = \gamma(\tau_i, f_{\mathrm{pw},j})$ can be calculated more efficiently more predefinition of pseudo-wavelets and truncated waveforms.

Similar to STFT, the proposed PW method can be considered as performing repeated calculation with hopping windows along data array. Such procedure is illustrated in Figure 24. Meaningful data are depicted as greyed rectangles, forming input signal matrix $\boldsymbol{X}_{\mathrm{input}}$. To enable matrix multiplication, truncated data arrays are zero-padded to maintain the same lengths. The initialization of $\boldsymbol{X}_{\mathrm{input}}$ is shown in Algorithm 1

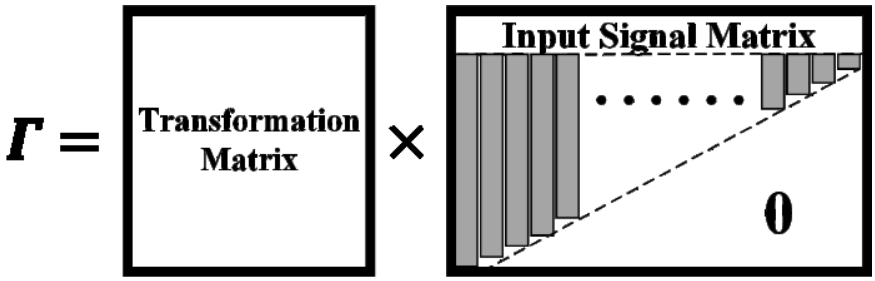

Figure 24 Illustration on the matrix formation of proposed method.
Reprinted with permission from C. Qian and M. Kezunovic, "A power waveform classification method for adaptive synchrophasor estimation," in *IEEE Transactions on Instrumentation and Measurement*, vol. 67, no. 7, pp. 1646-1658, Jul. 2018. Copyright 2018, IEEE.

Algorithm 1 Initialization of matrix $\boldsymbol{X}_{\text{input}}$ (hop size = 1, array size = 4)

1: **READ** input $x(t)$

2: **DETREND & NORMALIZE** input $x(t)$, yielding $\hat{x}(t)$

e.g.: $\hat{x}(t) = [x_1, x_2, x_3, x_4]^{\mathrm{T}}$

3: **CIRCULAR SHIFT** $\hat{x}(t)$ and populate into matrix $\boldsymbol{X}_{\mathrm{N\times N}}$

e.g.: $\boldsymbol{X}_{\mathrm{N\times N}} = \begin{bmatrix} x_4 & x_3 & x_2 & x_1 \\ x_1 & x_4 & x_3 & x_2 \\ x_2 & x_1 & x_4 & x_3 \\ x_3 & x_2 & x_1 & x_4 \end{bmatrix}$

4: **CALCULATE** upper triangular matrix of $\boldsymbol{X}_{\mathrm{N\times N}}$

e.g.: $\boldsymbol{X}_{\mathrm{N\times N}} = \begin{bmatrix} x_4 & x_3 & x_2 & x_1 \\ 0 & x_4 & x_3 & x_2 \\ 0 & 0 & x_4 & x_3 \\ 0 & 0 & 0 & x_4 \end{bmatrix}$

5: **FLIP** along the center, and result in input signal matrix $\boldsymbol{X}_{\mathrm{input}}$

e.g.: $\boldsymbol{X}_{\mathrm{input}} = \begin{bmatrix} x_1 & x_2 & x_3 & x_4 \\ x_2 & x_3 & x_4 & 0 \\ x_3 & x_4 & 0 & 0 \\ x_4 & 0 & 0 & 0 \end{bmatrix}$

The transformation matrix comprises of a set of pseudo-wavelets with customized frequencies. When the frequencies of pseudo-wavelets are predetermined, this matrix does not update, and therefore, can be generated offline. Since each pseudo-wavelet has finite time support, truncation of input signal is also conducted when pseudo-wavelets row vector multiplies input signal column vector. The values of maximum pseudo-wavelet frequency $f_{\mathrm{pw,max}}$, as well as frequency resolution Δf_{pw} are chosen empirically so that enough frequency details can be provided. The minimum value of pseudo-wavelet frequency pseudo-wavelets $f_{\mathrm{pw,min}}$ is determined by the reciprocal of total data length, which is also the frequency resolution of DFT.

8.3.5 Interpretation of Pseudo-Wavelet Analysis result Γ

Any calculated value of $\Gamma_{i,j} = \gamma(\tau_i, f_{\mathrm{pw},j})$ is merely associated with a single time delay and a single frequency component. Since various types of electromechanical dynamic events are

differentiated by their distinct progression signature on both temporal and frequency composition levels, therefore, naturally the next step is to interpret the time-frequency analysis results, i.e., matrix $\boldsymbol{\Gamma}$. Specifically, by fixing a single time instant, we get the frequency composition of the signal associated with a specific time, i.e., vector $\Gamma_{i,*} = \gamma(\tau_i, \boldsymbol{f}_{\mathrm{pw}})$; similarly, the progression of a selected frequency component $f_{\mathrm{pw},j}$ along time is manifested by vector $\Gamma_{*,j} = \gamma(\boldsymbol{\tau}, f_{\mathrm{pw},j})$.

Determined by the settings of the algorithm, the frequency resolution, and the frequency range under scrutiny of pseudo-wavelet analysis together determine the number of columns of matrix $\boldsymbol{\Gamma}$. It is reasonable to produce an illustrative result of the complete pseudo-wavelet analysis result of the waveform, covering all the discrete values of time delays and frequencies. Nevertheless, it is feasible, and often more useful, to choose certain "subsections" of frequency ranges instead of analyzing the whole frequency axis. In the latter case, it matters what ranges of frequency should be of higher priority in terms of providing more insights of the time progression of frequency components in the input signal. Since the power system fundamental frequency is usually within a small range around nominal frequency, and "zero-band" frequencies are theoretically the integer fractions of the actual fundamental frequency, it is reasonable to scrutinize the regions around the integer fractions of 60Hz (e.g., 10Hz, 12Hz, 15Hz, 20Hz, 30Hz, etc.) with higher frequency resolution.

8.3.6 Feature Extraction of Electromechanical Dynamic Waveforms

8.3.6.1 Extraction of Frequency Features

The features of the electromechanical dynamic waveforms are indicated by the progression, or intuitively, the shape, of frequency band $\Gamma_{*,j} = \gamma(\boldsymbol{\tau}, f_{\mathrm{pw},j})$, which corresponds to a region in matrix Γ. Therefore, it is crucial to extract the signature points from matrix Γ that marks the boundary of such frequency bands.

As discussed in Section 8.3.3, the value of $\Gamma_{*,j} = \gamma(\boldsymbol{\tau}, f_{\mathrm{pw},j})$ would theoretically be zero when $f_{\mathrm{pw},j}$ happens to coincide with one of the integer fractions of input signal frequency. It is because of this that the analysis results shown in Figure 23 contains "dark bands". For convenience, these frequencies are named "signature frequencies" of the pseudo-wavelet analysis, denoted by, f_{pwsig}.

Note that, outside f_{pwsig} frequencies, the values $\Gamma_{*,j} = \gamma(\boldsymbol{\tau}, f_{\mathrm{pw},j})$ oscillate, and yet on f_{pwsig} frequencies, values $\Gamma_{*,j} = \gamma(\boldsymbol{\tau}, f_{\mathrm{pw},j})$ are always zero (or nearly zero, practically). Therefore, it is easier to track the progression of frequency components using the "dark bands". On the other hand, as suggested in previous paragraphs, the analysis can be performed only on the vicinities of f_{pwsig} frequencies, and with higher frequency resolution.

As shown in Figure 23 (a) and (b), the "dark band" regions are outlined by the points of each bright region corresponding to the highest and lowest frequency profile. Such points are also mathematically described as having the smallest time derivative values. For the sake of convenience, these dots are termed "signature points" in this Section.

In practice, $\Gamma_{i,j} = \gamma(\tau_i, f_{\mathrm{pw},j})$ represent contours, rather than regions, as shown in Figure 23 (c) and (d). It is worth noting that, due to calculation errors, it is hardly possible to guarantee

that any single discrete raw calculation result $\Gamma_{i,j}$ exactly equals any of the contour values in the figure. In practice, the contours are generated by grouping the "dots" (values of $\Gamma_{i,j}$) within the vicinity of a predetermined value. By setting the margins for depicting the contour lines, areas that satisfy the criteria can be obtained. By carefully setting up threshold values, and criteria restricting the boundaries, $\Gamma_{i,j}$ can be visually perceived as the "thickness" of contour lines, as shown in Figure 25.

As depicted in Figure 25, once the contouring parameters are chosen, the pseudo-wavelet analysis result matrix $\Gamma = \gamma(\tau_i, f_{\mathrm{pw},j})$ can be effectively reduced to a matrix consisting of binary information, i.e., whether a particular value in the matrix, $\gamma(\tau_i, f_{\mathrm{pw},j})$, belongs to the contour. From this point in the discussion, symbol Γ_B is used to represent this matrix consisting only of 0 and 1, in which value 1 represent that $\gamma(\tau_i, f_{\mathrm{pw},j})$ values belongs to the contour region. Intuitively, Figure 25 is a visualization of matrix Γ_B, which consist of elements of 0's and 1's.

In order to locate the signature points in Figure 25, two metrics are introduced: the frequency occurrence rate (FOR), and time occurrence rate (TOR).

FOR is defined as the number of occurrence within a specifically defined frequency range, which is achieved by projecting Γ_B contour onto frequency axis. Since Γ_B consists solely of 0's and 1's, this is easily achieved by summing up the Γ_B elements in each row.

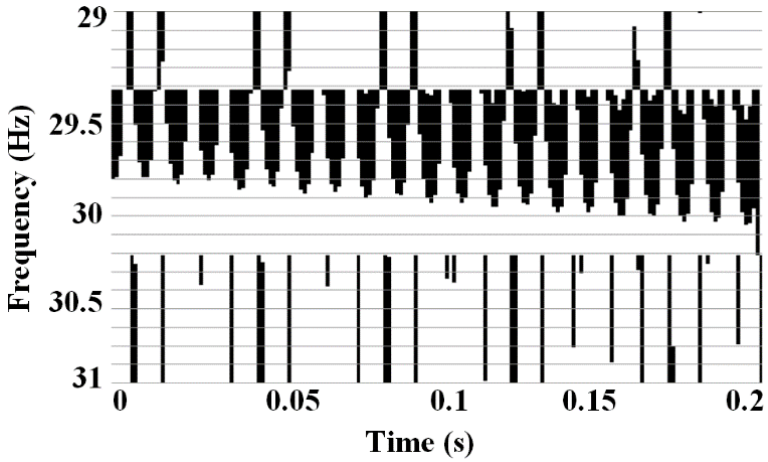

Figure 25 Pseudo-wavelet analysis result for frequency ramp signal.
Reprinted with permission from C. Qian and M. Kezunovic, "A power waveform classification method for adaptive synchrophasor estimation," in *IEEE Transactions on Instrumentation and Measurement*, vol. 67, no. 7, pp. 1646-1658, Jul. 2018. Copyright 2018, IEEE.

Similarly, TOR is defined as the number of Γ_B elements in a predetermined time range, by projecting Γ_B onto time axis. TOR is calculated by summing up the Γ_B element in each column. The steep region of Γ_B is characterized by large TOR values; on the other hand, small value of TOR indicates a more flat feature of the Γ_B elements, which marks the boundary of "dark bands". The points associated with the least TOR are chosen as the "signature points".

As shown in Figure 26 (a), the blue dots represent the extracted signature points from raw analysis result in Figure 26 (b). The feature of the dynamics can be acquired by outlining the envelope of signature points. And in the case of Figure 26, there is a clear frequency oscillation in the waveform.

8.3.6.2 Extraction of Amplitude Features

The amplitude level of each frequency component is represented by the value of $\Gamma_{i,j} = \gamma(\tau_i, f_{\mathrm{pw},j})$. Specifically, the stronger the signal is, the higher the correlation coefficient is. When

there is a variation in waveform amplitude, the correlation coefficients $\Gamma_{i,j}$ will manifest such dynamics. Shown in Figure 27 are the PW analysis results of an amplitude-modulated signal. It can be seen that frequency zero-bands remain stable, while the γ_{ij} values at other frequencies are oscillating.

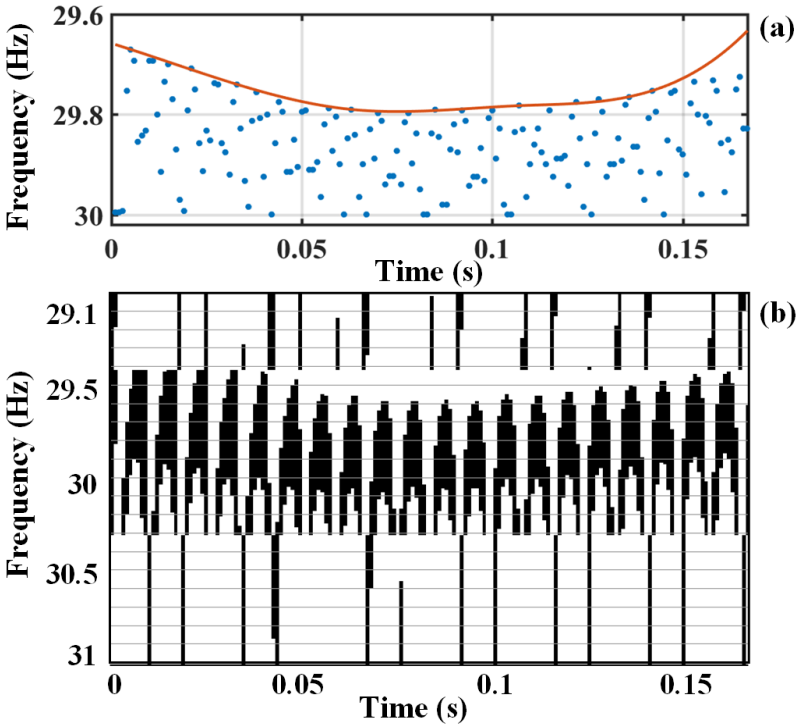

Figure 26 Pseudo-wavelet analysis result for frequency modulation signal.
(a). Extracted time-frequency feature; (b). Raw analysis results showing the contour.
Reprinted with permission from C. Qian and M. Kezunovic, "A power waveform classification method for adaptive synchrophasor estimation," in *IEEE Transactions on Instrumentation and Measurement*, vol. 67, no. 7, pp. 1646-1658, Jul. 2018. Copyright 2018, IEEE.

The extraction of amplitude feature is performed by pulling out the elements of matrix $\boldsymbol{\Gamma}$ that associate with a single frequency component, revealing the trajectory of correlation intensity

w.r.t. time. Practically, as long as the frequency is not zero-band frequency, oscillation patterns can be uncovered.

Note that $\Gamma_{i,j}$ values are in fact oscillating because of the periodical nature of correlation calculation. Hilbert Transform can be utilized in this situation to smooth out the oscillation and reveal the envelope of amplitude features. In order to extract values of $\Gamma_{i,j}$ should not be the signature frequency values. As illustrated in Figure 28, the amplitude fluctuation feature can be captured for various severities of amplitude modulation scenarios.

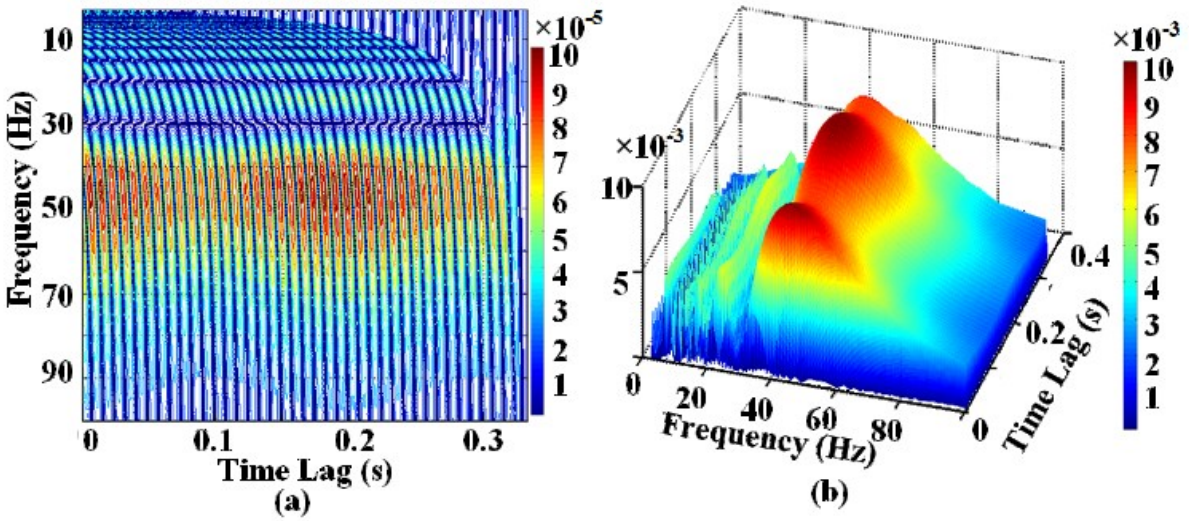

Figure 27 Illustrations of proposed analysis on amplitude-modulated signal. Contours, (b) 3D plot of the elements of correlation matrix $\boldsymbol{\Gamma}$.
Reprinted with permission from C. Qian and M. Kezunovic, "A power waveform classification method for adaptive synchrophasor estimation," in *IEEE Transactions on Instrumentation and Measurement*, vol. 67, no. 7, pp. 1646-1658, Jul. 2018. Copyright 2018, IEEE.

(a)

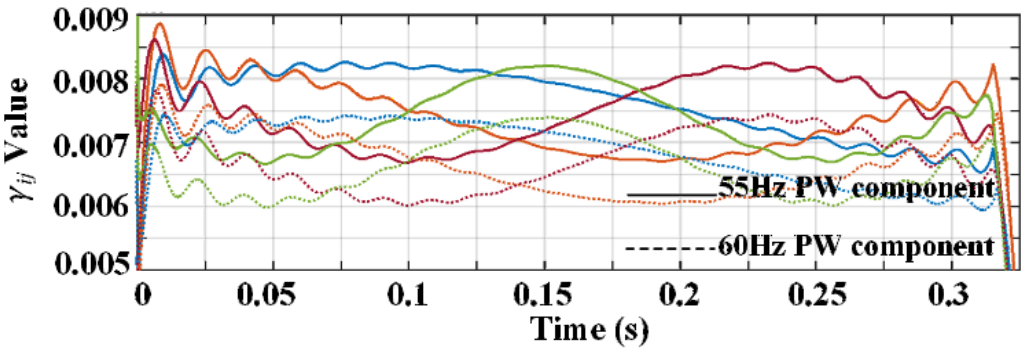

Figure 28 Envelope extraction using Hilbert Transform at various modulation frequencies. 55Hz PW components are shown in solid curves, and 60Hz PW components are shown in dotted curves. Blue: f_{AM}=2Hz, orange: f_{AM}=3Hz, red: f_{AM}=4Hz, green: f_{AM}=5Hz. Reprinted with permission from C. Qian and M. Kezunovic, "A power waveform classification method for adaptive synchrophasor estimation," in *IEEE Transactions on Instrumentation and Measurement*, vol. 67, no. 7, pp. 1646-1658, Jul. 2018. Copyright 2018, IEEE.

8.4 Phasor Parameter Calculation During Electromechanical Transients

During electromechanical dynamic conditions, the modulations on electrical quantities should be adequately detected, captured, and characterized. This is achieved by designing signal models that explicitly represent the features embedded in various dynamic waveforms. Based on the end-use application, the waveform features of interest in electromechanical dynamics conditions are summarized in Table 8.

Table 8. Summary of Electromechanical Dynamic Conditions and Corresponding Control Applications

Electromechanical Dynamic Conditions	Signal Manifestation	Control Applications
Low-frequency oscillation	Amplitude modulation	PSS, AVR, etc.
Sub-synchronous oscillation	Frequency modulation	SVC, etc.
Rotor loss-of-synchronism	Frequency ramp	AVR, etc.

With the waveform switching mechanism shown in Figure 8, the signal models can be adaptively switched to accommodate the actual signal representation. Depending on the specific

empirical conditions under which phasor parameters are extracted, the signal models can be designed accordingly. For example, the oscillation mode frequency information can be used to further specify signal models.

8.4.1 Signal Modeling

8.4.1.1 Rotor Loss-of-synchronism

In the case of rotor loss-of-synchronism, in a small data observation window, it is considered that the frequency ramps linearly at a constant rate quantified as ROCOF, or R_f [127]-[129].

$$x(t) = \sqrt{2} \cdot A \cdot \cos\left(2\pi f_0 t \ + 2\pi \Delta f t + \pi R_f t^2 + \varphi_0\right) \tag{8.22}$$

The phasor parameters of interest is:

$$p(t) = Ae^{\mathrm{j}(2\pi \Delta f t + \pi R_f t^2 + \varphi_0)} \tag{8.23}$$

8.4.1.2 Electromechanical Oscillations

During an electromechanical oscillation dynamic condition, the amplitude and/or frequency of the waveform will be modulated by sinusoidal terms [130]-[132].

$$\begin{aligned} x(t) = \sqrt{2}A[1 + k_a \cos(2\pi f_m t)] \\ \cos\left[2\pi f_0 t + 2\pi \Delta f t + k_f \cos(2\pi f_m t - \pi) + \ \varphi_0\right] \end{aligned} \tag{8.24}$$

The phasor parameters of interest is:

$$p(t) = A[1 + k_a \cos(2\pi f_m t)]e^{\mathrm{j}(2\pi \Delta f t + k_f \cos(2\pi f_m t - \pi) + \varphi_0)} \tag{8.25}$$

8.4.2 Algorithmic Solutions

The phasor parameters of interest in the signal formulations, i.e., Equations (8.24) and (8.25), are embedded in the nonlinear cosine functions. To formulate the problem in terms of mathematical equations, consider a generalized signal equation,

$$f(\boldsymbol{t}; \boldsymbol{p}) = \|\boldsymbol{b} - x(\boldsymbol{t}; \boldsymbol{p})\|_2^2 \tag{8.26}$$

where $f(\boldsymbol{t};\boldsymbol{p})$ is a cost function quantifying the fitting error of predetermined signal model $x(\boldsymbol{t};\boldsymbol{p})$ compared to measurement sample $\boldsymbol{b}$.

The curve-fitting problem described as Equation (8.26) may be solved by various numerical approaches. Most notably, gradient descent algorithm and Gauss-Newton algorithm [133].

8.4.2.1 Gradient Descent Algorithm

Given Equation (8.26), where $f(*)$ is known, and $\boldsymbol{p}$ is the only unknown parameter, the gradient descent solution to the problem can be described as:

$$\boldsymbol{p}^{(k+1)} = \boldsymbol{p}^{(k)} + \gamma^{(k)}\boldsymbol{d}^{(k)} \tag{8.27}$$

where $\gamma^{(k)}$ is the step size for each iteration, and $\boldsymbol{d}^{(k)}$ is the direction of the increment at each step given the latest estimate $\boldsymbol{p}^{(k)}$. $\boldsymbol{d}^{(k)}$ is chosen to be the direction of the most rapid decrease of the function $f(\boldsymbol{t};\boldsymbol{p})$, i.e., the opposite of normalized gradient of $f(\boldsymbol{t};\boldsymbol{p})$:

$$\boldsymbol{d}^{(k)} = -\frac{\nabla f(\boldsymbol{t};\boldsymbol{p})}{\|\nabla f(\boldsymbol{t};\boldsymbol{p})\|_2}$$

where, $$\nabla f(\boldsymbol{t};\boldsymbol{p}) = \left[\frac{\partial f(\boldsymbol{t};\boldsymbol{p})}{\partial p_1}, \frac{\partial f(\boldsymbol{t};\boldsymbol{p})}{\partial p_2}, \dots, \frac{\partial f(\boldsymbol{t};\boldsymbol{p})}{\partial p_{\dim(\boldsymbol{p})}}\right]^{\mathrm{T}} \tag{8.28}$$

And the determination of the value of $\gamma^{(k)}$ is through searching for the γ value that satisfies:

$$\gamma^{(k)} \in \operatorname{argmin}_{\gamma}\left[f\left(\boldsymbol{t};\boldsymbol{p}^{(k)} + \gamma^{(k)}\boldsymbol{d}^{(k)}\right)\right] \tag{8.29}$$

The value of step size is allowed to change at every iteration, and can be obtained through line search, inexact line search, or Barzilai-Borwein method [134]. The selection of step size determines whether gradient descent algorithm can converge, and how fast it converges.

Equation (8.29) minimizes the approximation error, or curve-fitting error:

$$\boldsymbol{b} \approx x\left(\boldsymbol{t};\boldsymbol{p}^{(k)}\right) + \nabla x\left(\boldsymbol{t};\boldsymbol{p}^{(k)}\right)\cdot\left(\boldsymbol{p}^{(k+1)} - \boldsymbol{p}^{(k)}\right) \tag{8.30}$$

8.4.2.2 Newton's Algorithm and Gauss-Newton Algorithm

Similar to Equation (8.27), in Newton's Algorithm, the iteration is in the form of:

$$\boldsymbol{p}^{(k+1)} = \boldsymbol{p}^{(k)} + \left(\boldsymbol{H}^{(k)}\right)^{-1} \cdot \nabla x\left(\boldsymbol{t}; \boldsymbol{p}^{(k)}\right) \tag{8.31}$$

where $\boldsymbol{H}^{(k)} \equiv \nabla^2 f\left(\boldsymbol{p}^{(k)}\right)$ is the Hessian matrix of $f(*)$ at $\boldsymbol{p}^{(k)}$. Equation (8.31) approximate measurement with quadratic terms:

$$\begin{aligned} \boldsymbol{b} \approx x\left(\boldsymbol{t}; \boldsymbol{p}^{(k)}\right) + \nabla x\left(\boldsymbol{t}; \boldsymbol{p}^{(k)}\right) \cdot \left(\boldsymbol{p}^{(k+1)} - \boldsymbol{p}^{(k)}\right) \\ + \frac{1}{2}\left(\boldsymbol{p}^{(k+1)} - \boldsymbol{p}^{(k)}\right)^{\mathrm{T}} \nabla^2 x\left(\boldsymbol{t}; \boldsymbol{p}^{(k)}\right)\left(\boldsymbol{p}^{(k+1)} - \boldsymbol{p}^{(k)}\right) \end{aligned} \tag{8.32}$$

The elements of Hessian matrix $\boldsymbol{H}$ are calculated by differentiating the gradient ∇x:

$$\boldsymbol{H} = \nabla^2 x\left(\boldsymbol{t}; \boldsymbol{p}^{(k)}\right), \boldsymbol{H}_{ij} = \frac{\partial^2 x}{\partial p_i p_j} \tag{8.33}$$

In Gauss-Newton algorithm, Hessian matrix is approximated by:

$$\boldsymbol{H}_{ij} \approx \frac{\partial x}{\partial p_i} \cdot \frac{\partial x}{\partial p_j} \tag{8.34}$$

Thus Equation (8.31) is approximated by:

$$\Delta \boldsymbol{p}^{(k)} = \left[\boldsymbol{J}^{(k)\mathrm{T}} \boldsymbol{J}^{(k)}\right]^{-1} \boldsymbol{J}^{(i)T}\left[\boldsymbol{b} - x(\boldsymbol{t}, \boldsymbol{p}^{(k)})\right] \tag{8.35}$$

where

$$\boldsymbol{J}_{i,j}{}^{(k)} = \frac{\partial [\boldsymbol{b} - x(\boldsymbol{t}; \boldsymbol{p})]_i}{\partial p_j} \tag{8.36}$$

8.4.3 Implementation

The performance evaluation of the algorithms introduced in Chapter 8 are primarily determined by two factors: (i). The accuracy of signal modeling; (ii). The accuracy of numerical optimization method, particularly, convergence rate and divergence issues.

The first issue is alleviated by incorporating a dedicated waveform type identification technique, which is introduced in Section 8.3. By switching the most appropriate signal model according to the input waveform type, the fitting error can be minimized.

The second issue is relevant to the nonlinear regression technique used in solving the optimization problem described by Equation (8.26). For example, gradient descent algorithm is slow near the local optimal point, and Newton's algorithm may diverge.

In this Dissertation, Levenberg-Marquardt algorithm (LMA) is used to solve the optimization problem in Equation (8.26) [135]. The least square solution to Equation (8.26) can be obtained through an iterative process, where the increment on unknown vector $\boldsymbol{p}$ is calculated as:

$$\Delta \boldsymbol{p}^{(k)} = \left[\boldsymbol{J}^{(k)\mathrm{T}}\boldsymbol{J}^{(k)} + \mu^{(k)}\mathrm{diag}\left(\boldsymbol{J}^{(k)\mathrm{T}}\boldsymbol{J}^{(k)}\right)\right]^{-1}\boldsymbol{J}^{(i)T}\left[\boldsymbol{b} - f(\boldsymbol{t}, \boldsymbol{p}^{(k)})\right] \quad (8.37)$$

where

$$\boldsymbol{J}_{i,j}{}^{(k)} = \frac{\partial[\boldsymbol{b} - x(\boldsymbol{t}; \boldsymbol{p})]_i}{\partial p_j}$$

Each iteration of solving parameter $\boldsymbol{p}$ is associated with two parameters: direction of the increment, and size of the increment (step size).

The damping factor $\mu^{(k)}$ is used to achieve a trade-off between Gauss-Newton algorithm and gradient descent algorithm. Specifically, at the beginning of an iteration, $\mu^{(k)}$ is chosen to be large to mimic gradient descent method so that LMA can reach local optimal point fast; then, the value of $\mu^{(k)}$ is reduced so that LMA becomes more similar to Gauss-Newton algorithm so that higher accuracy and fast convergence can be reached. In particular, the two extreme cases of Equation (8.37):

$$\Delta \boldsymbol{p}^{(k)} = \frac{1}{\mu^{(k)}}\boldsymbol{J}^{(i)T}\left[\boldsymbol{b} - f(\boldsymbol{t}, \boldsymbol{p}^{(k)})\right], \mu^{(k)} \to +\infty \quad (8.38)$$

Equation (8.38) describes gradient descent algorithm,

$$\Delta \boldsymbol{p}^{(k)} = \left[\boldsymbol{J}^{(k)\mathrm{T}}\boldsymbol{J}^{(k)}\right]^{-1}\boldsymbol{J}^{(i)T}\left[\boldsymbol{b} - f(\boldsymbol{t}, \boldsymbol{p}^{(k)})\right], \mu^{(k)} \approx 0 \qquad (8.39)$$

Equation (8.39) describes Gauss-Newton algorithm.

8.5 Conclusion

In this Chapter, a phasor parameter calculation approach for electromechanical dynamic events is proposed. In order to improve calculation accuracy, a waveform classification mechanism is designed so that the most appropriate signal model can be used for that waveform. The waveform classification leverages new mother wavelet, termed “pseudo-wavelet”, specifically designed for the time-frequency feature extraction of power system waveforms. With the result of waveform classification, accurate nonlinear waveform models can be designed to fit the actual dynamic scenarios. In order to achieve high accuracy and optimal computational burden, Levenberg-Marquardt algorithm is used to obtain the signal parameters from nonlinear signal models.

9. PERFORMANCE EVALUATION OF PROPOSED PHASOR PARAMETER CALCULATION APPROACH [*]

9.1 Introduction

9.1.1. Goal and Objective

As stated before, the goal of the Dissertation is to present a new phasor parameter calculation algorithm. The objectives of the PMU algorithm development are: (i). Algorithm accuracy should comply with relevant international standard, such as IEC/IEEE 60255-118-1 [10], and (ii). Algorithm should ensure test performance under the non-standard waveforms coming from different application scenarios. This chapter is focused on the validation of the Dissertation hypothesis, which is related to the algorithm performance evaluation under design tests and application tests.

9.1.2. Approach to Hypothesis Validation

The hypothesis is that phasor parameter calculation accuracy can be improved by designing phasor parameter calculation algorithms tailored to the waveforms associated with each type of electromagnetic and electromechanical dynamic event. Hypothesis validation is conducted

---

[*] Reprinted with authors' permission from M. Kezunovic, C. Qian, C. Seidl, J. Ren, "Testbed for timing intrusion evaluation and tools for lab and field testing of synchrophasor system", *IEEE International Conference on Smart Grid Synchronized Measurements and Analytics (SGSMA 2019)*, pp. 1-8, College Station, TX. May 2019. Copyright 2019, IEEE.

through the assessment of algorithm accuracy using different application use cases. Three aspects of hypothesis validation process are discussed: test use cases, test methodology, and test procedure. They are illustrated in Figure 29, and further discussed below.

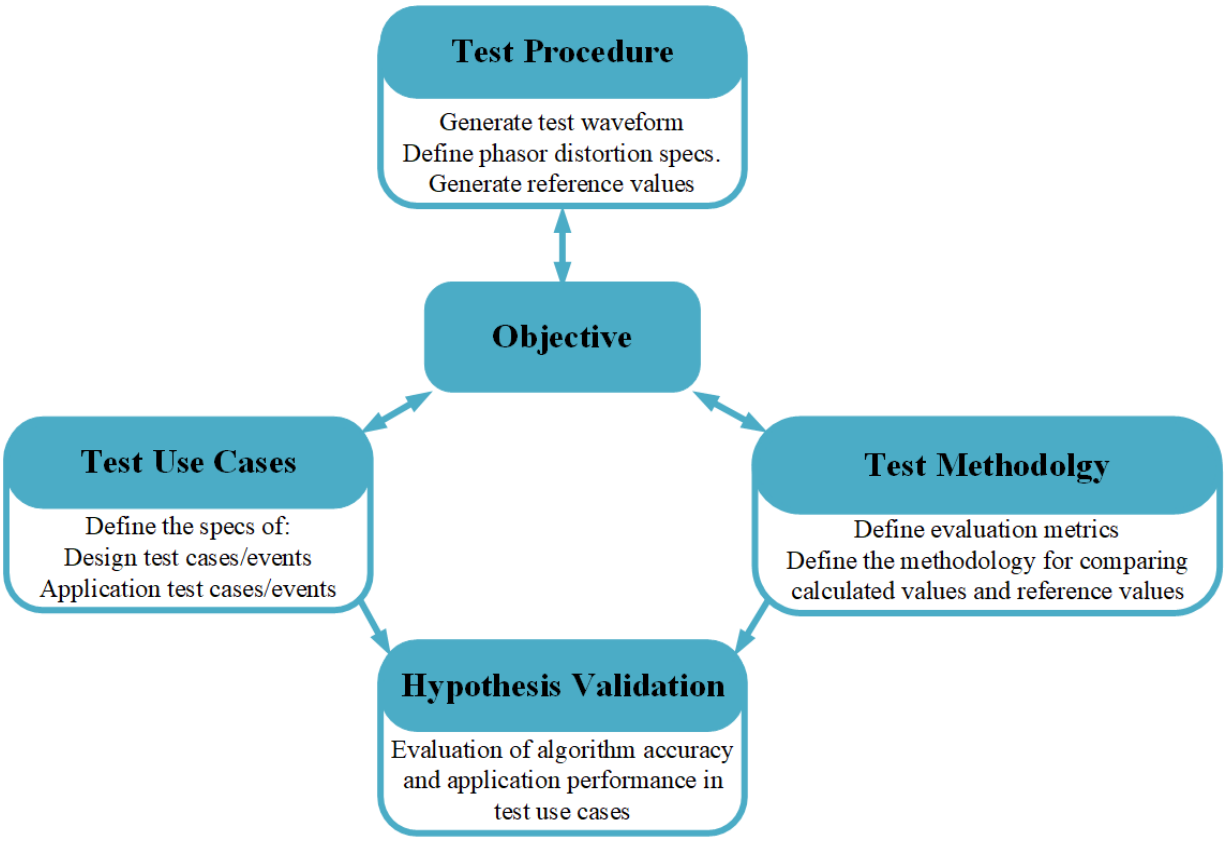

Figure 29 Proposed approach to hypothesis validation

9.1.2.1. Test Procedures

The test procedure, associated with each test case, describes the physical signal connections and resulting data flows in a test. Due to the differences in the design and application test cases, their test procedures are different as depicted in Figure 30 and Figure 31, respectively. The section numbers, where the details of test procedures are discussed, are also noted.

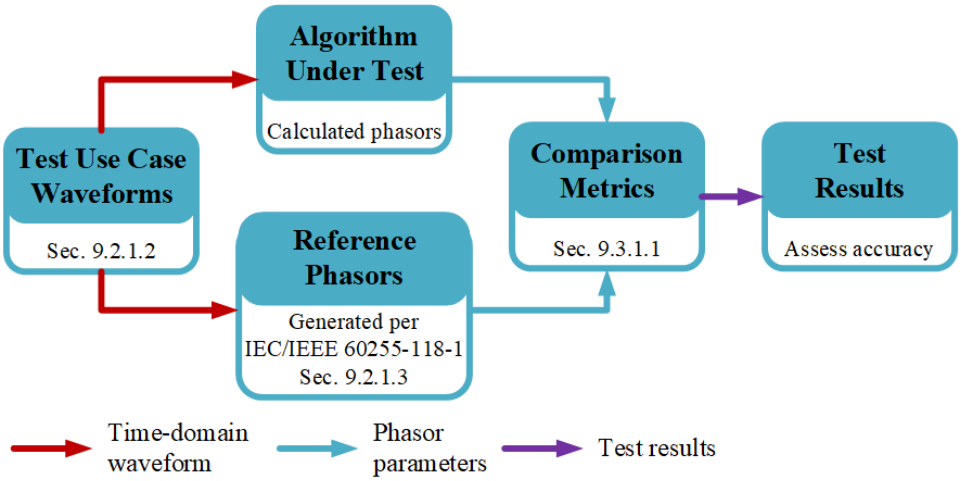

Figure 30 Test procedure for design tests

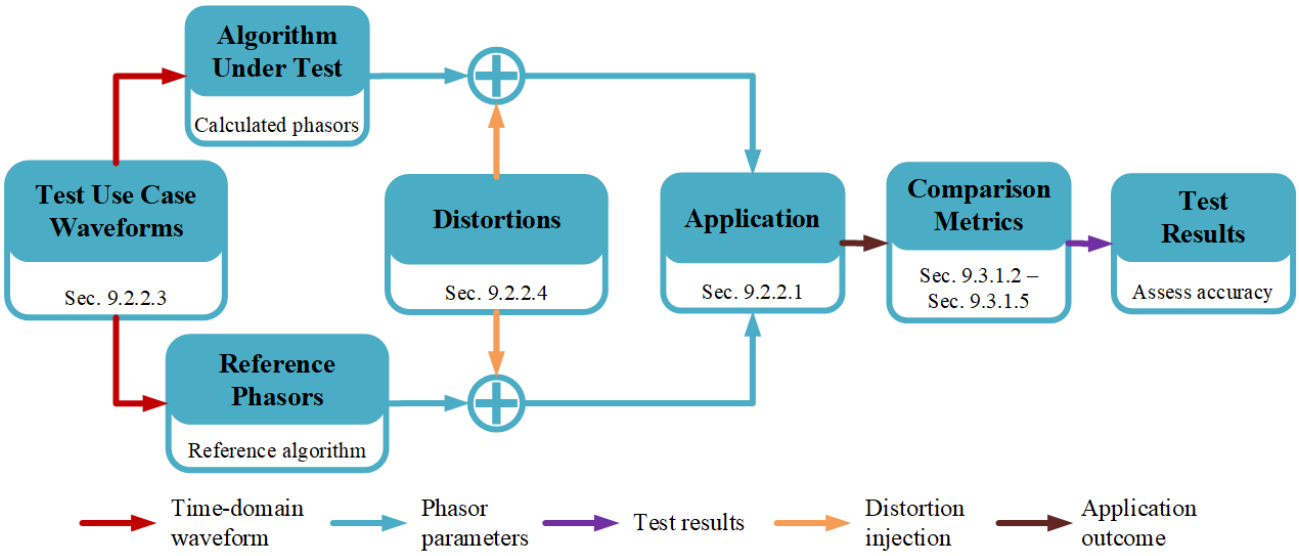

Figure 31 Test procedure for application tests

9.1.2.2. Test Use Cases

The test use cases characterize power system events resulting in selected use cases, and the corresponding test use case waveforms. Test use cases reflect the purpose of the test, and can be classified into two categories: design and application test use cases.

Design test use cases are aimed at evaluating whether an algorithm satisfies the performance requirements specified in standard IEC/IEEE 60255-118-1 [10]. These requirements are outlined in Table 9 in section 9.2.1.

Application test use cases are aimed at assessing whether the algorithm produces phasors that sufficiently meet the performance expectation of subsequent applications. This is done by evaluating the impact of algorithm output accuracy on the application performance, and this impact is quantified in terms of the metrics defined in Section 9.3.1.4 and Section 9.3.1.5. An application test use case is designed for a given application event, which entails the specifications of the dynamic event property of interest, and the test waveforms generated through simulations of such an event's use case using power system models. The application test use cases are not defined in the standards, and are specified in Section 9.2.2.2.

The distortion of phasor parameters during their transfer from PMUs to PDCs may have negative impacts on the application performance. Such impacts should also be evaluated. In order to do so, distortions caused by PDC processing and communication networks are introduced. The characterization of the distortions is discussed in Section 9.2.2.4.

9.1.2.3. Test Methodology

The algorithm assessment in design tests is utilizing the metrics to compare calculated values by the proposed algorithm against the reference values. This entails defining the evaluation metrics, and establishing the algorithm assessment pass/fail criteria. In standard IEC/IEEE 60255-118-1, amplitude and phase angle parameter calculation accuracies are jointly assessed through a comparison metric defined as Total Vector Error percentage (TVE), and frequency accuracy is assessed by Frequency Error (FE). The algorithm pass/fail criteria are also elaborated in the standard [10], as shown in Tables 16 and 17 in Section 9.3.1.1.

The algorithm assessment in the application tests is defined as an impact that the algorithm accuracy has on the application performance. Correspondingly, the comparison metrics need to evaluate the application performance when subjected to the outputs of the proposed algorithm as compared to a reference algorithm. This should result in the performance ranking criteria that allow evaluation of the proposed algorithm performance against the reference algorithm. Since application tests are not specified in the standards, both the comparison metrics and performance ranking criterion will be defined and discussed from Section 9.3.1.2 through Section 9.3.1.5.

9.2. Algorithm Assessment in Test Use Cases

The use cases in both design tests and application tests are discussed in this section. Design and application test use cases are described using different terminologies, and are conducted using different procedures, as shown in Figure 32.

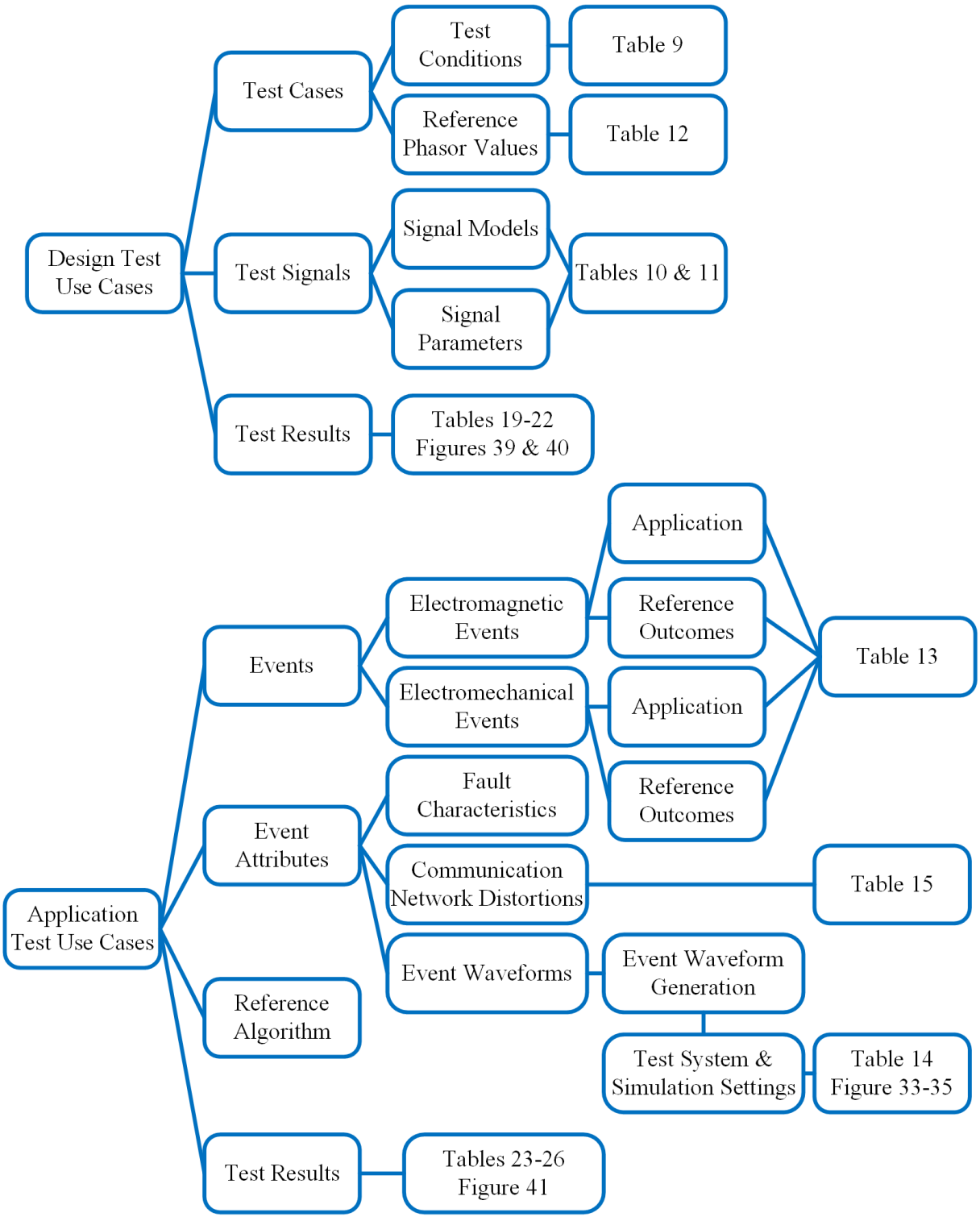

Figure 32 Aspects of hypothesis validation using test use cases

9.2.1. Design Test Use Cases

9.2.1.1. Test Use Case Specifications

Test use cases are specified in standard [10], as shown in Table 9. The standard defines two performance classes: P class and M class. P class is intended for applications that require fast response such as protection applications. P class requires shorter measurement latency time, narrower frequency bandwidth, and lower harmonic signal rejection requirement. On the other hand, M class is intended for applications that require higher precision but do not require minimal reporting delay. M class allows for longer latencies, more sophisticated filtering for a wider frequency range requirement. As a result, the test use case specifications for P class and M class categories are different as shown in Table 9.

Table 9. Design Test Use Case Specifications

Test Case	Test Conditions	
	P class	M class
Signal frequency variation	±2Hz around nominal	±5Hz around nominal
Signal amplitude variation	10%-200% p.u.	10%-200% p.u.
Single harmonic distortion	1% harmonic level	10% harmonic level
Out-of-band interference	None	10% interference level
Amplitude modulation	Modulation frequency 0.1Hz to 2Hz	Modulation frequency 0.1Hz to 2Hz
Frequency modulation		
System frequency ramp	Ramp rate ±1Hz/s, ramp range ±2Hz	Ramp rate ±1Hz/s, ramp range ±5Hz
Magnitude step	±10% p.u. magnitude	
Angle step	±π/18 angle	

9.2.1.2. Test Use Case Waveforms and Test Procedure Implementation

Test waveforms in each test use case are generated according to the design specification [10]. The implementation of test use cases and algorithm performance evaluation are carried out using MATLAB/Simulink program with the waveform specification given in Tables 10 and 11 for design and application tests, respectively.

Table 10. Waveform Specifications for Design Test – Steady State Tests

Test Case	Signal Model
Signal frequency and magnitude tests	$x_a = X_m \cos(2\pi f_{\text{in}} t)$ $x_b = X_m \cos(2\pi f_{\text{in}} t - 2\pi/3)$ $x_c = X_m \cos(2\pi f_{\text{in}} t + 2\pi/3)$ where, x_a, x_b, x_c are the A, B, and C phase signals; X_m is the amplitude of the input signal; f_{in} is the input signal frequency in Hz.
Harmonic distortion test	$x_a = X_m \cos(2\pi f_0 t) + X_m k_x \cos(2\pi n f_0 t)$ $x_b = X_m \cos(2\pi f_0 t - 2\pi/3) + X_m k_x \cos(2\pi n f_0 t - 2\pi n/3)$ $x_c = X_m \cos(2\pi f_0 t + 2\pi/3) + X_m k_x \cos(2\pi n f_0 t + 2\pi n/3)$ where, X_m is the amplitude of the input signal; f_0 is the nominal power system frequency in Hz; k_x is the harmonic amplitude factor, and n is the harmonic order.
Out-of-band interference test	$x_a = X_m \cos(2\pi f_{\text{in}} t) + X_m k_x \cos(2\pi n f_i t)$ $x_b = X_m \cos(2\pi f_{\text{in}} t - 2\pi/3) + X_m k_x \cos(2\pi n f_i t - 2\pi/3)$ $x_c = X_m \cos(2\pi f_{\text{in}} t + 2\pi/3) + X_m k_x \cos(2\pi n f_i t + 2\pi/3)$ where, X_m is the amplitude of the input signal; f_{in} is the input signal frequency in Hz; k_x is the harmonic amplitude factor, and n is the harmonic order; f_i is interference frequency in Hz.

Test Case	Signal Parameters	
	P Class	M Class
Signal frequency variation	f_{in} values: 58Hz to 62Hz, with increment of 0.5Hz	f_{in} values: 55Hz to 65Hz, with increment of 0.5Hz
Signal amplitude variation	X_m values: 0.1 p.u. to 2 p.u., with increment of 0.1 p.u.	

Table 10 Continued

Test Case	Signal Parameters	
	P Class	M Class
Single harmonic distortion	$k_x = 0.01$ n values: 2 to 50	$k_x = 0.1$ n values: 2 to 50
Out-of-band interference	None	$k_x = 0.1$ f_{in} values: 57Hz to 63Hz, with increment of 1Hz f_i values: 17.2Hz, 23.6Hz, 26.8Hz, 28.4Hz, 29.2Hz, 29.6Hz, 29.8Hz, 29.9Hz, 90.1Hz, 90.2Hz, 90.4Hz, 90.8Hz, 91.6Hz, 93.2Hz, 96.4Hz, 102.8Hz, 115.6Hz

Table 11. Waveform Specifications for Design Test – Dynamic State Tests

Test Case	Signal Model
Measurement bandwidth test with modulation signals	$x_a = X_m[1 + k_x\cos(2\pi f_{\text{m}} t)]\cos[2\pi f_0 t + k_a\cos(2\pi f_{\text{m}} t - \pi)]$ $x_b = X_m[1 + k_x\cos(2\pi f_{\text{m}} t)]\cos[2\pi f_0 t - 2\pi/3 + k_a\cos(2\pi f_{\text{m}} t - \pi)]$ $x_c = X_m[1 + k_x\cos(2\pi f_{\text{m}} t)]\cos[2\pi f_0 t + 2\pi/3 + k_a\cos(2\pi f_{\text{m}} t - \pi)]$ where, X_m is the amplitude of the input signal; f_0 is the nominal power system frequency in Hz; f_{m} is the modulation frequency in Hz; k_x is the amplitude modulation factor; k_a is the phase angle modulation factor.
System frequency ramp	$x_a = X_m\cos(2\pi f_0 t + \pi R_f t^2)$ $x_b = X_m\cos(2\pi f_0 t - 2\pi/3 + \pi R_f t^2)$ $x_c = X_m\cos(2\pi f_0 t + 2\pi/3 + \pi R_f t^2)$ where, X_m is the amplitude of the input signal; f_0 is the nominal power system frequency in Hz; R_f is the frequency ramp rate in Hz/s.

Table 11 Continued

Test Case	Signal Model
Step changes in phase and magnitude	$x_a = X_m[1 + k_x u(t)]\cos[2\pi f_0 t + k_a u(t)]$ $x_b = X_m[1 + k_x u(t)]\cos[2\pi f_0 t - 2\pi/3 + k_a u(t)]$ $x_c = X_m[1 + k_x u(t)]\cos[2\pi f_0 t + 2\pi/3 + k_a u(t)]$ where, X_m is the amplitude of the input signal; f_0 is the nominal power system frequency in Hz; $u(t)$ is a unit step function k_x is the magnitude step size; k_a is the phase step size.

Test Case	Signal Parameters	
	P Class	M Class
Measurement bandwidth test with modulation signals	f_m from 0.1Hz to 2Hz, with increment of 0.1Hz $k_x = 0.1$ or $k_a = 0.1$	f_m from 0.1Hz to 2Hz, with increment of 0.1Hz $k_x = 0.1$ or $k_a = 0.1$
System frequency ramp	$R_f = \pm 1\mathrm{Hz/s}$, ramp range ±2Hz	$R_f = \pm 1\mathrm{Hz/s}$, ramp range ±5Hz
Step changes in phase and magnitude	$k_x = \pm 0.1$ or $k_a = \pm \pi/18$	

9.2.1.3. Generation of Reference Phasor Parameters

The reference phasor parameters are generated based on design test signal parameters shown in Table 12.

Table 12. Reference Phasor Parameters for Design Test Use Cases

Test Case	Reference Phasor Parameters	
All steady-state test use cases	Phasor	$X(nT) = \frac{X_m}{\sqrt{2}} \angle \left\{ 2\pi \Delta f nT + p\frac{2}{3}\pi \right\}$
	Frequency	$f(nT) = f_0 + \Delta f$
Amplitude and frequency modulation	Phasor	$X(nT) = \frac{X_m}{\sqrt{2}}[1 + k_x \cos(2\pi f_\mathrm{m} nT)]$ $\angle \left\{ k_a \cos(2\pi f_\mathrm{m} t - \pi) + p\frac{2}{3}\pi \right\}$
	Frequency	$f(nT) = f_0 - k_a \sin(2\pi f_\mathrm{m} t - \pi)$

Table 12 Continued

Test Case	Reference Phasor Parameters	
System frequency ramp	Phasor	$X(nT) = \frac{X_m}{\sqrt{2}} \angle \left\{ 2\pi \Delta f nT + p\frac{2}{3}\pi \right\}$
	Frequency	$f(nT) = f_0 + R_f(nT)$

X_m is the amplitude of input signal;
T is reporting interval;
$p = 0$ for phase A; $p = -1$ for phase B; $p = 1$ for phase C;
Δf is the frequency deviation of actual input frequency from nominal value;
f_0 is nominal frequency;
f_{m} is the modulation frequency in Hz;
k_x is the amplitude modulation factor;
k_a is the phase angle modulation factor;
R_f is the frequency ramp rate in Hz/s.

9.2.2. Application Test Use Cases

9.2.2.1. Selected Applications

Two applications are selected as examples to demonstrate the procedure of application testing. The power system models for the test use cases are implemented in Simulink Simscape Power Systems. All test use cases are performed on a two-area system [136]-[137] in Simulink program, where application test waveforms are obtained through time-domain simulations. A fault location algorithm [138] and an oscillation detection algorithm [139] are chosen as the example applications, in order to assess the impact of proposed algorithm's performance on an application under electromagnetic and electromechanical dynamic events, respectively.

9.2.2.2. Test Power System and Test Use Case Specifications

For each test use case, disturbances and subsequent dynamic events are specified and described in Table 13. The power system model used for application simulation is shown in Figure 33. The generators are modeled using the 6$^{\text{th}}$-order state-space model [59]. The transmission line parameters in the test power system are shown in Table 14.

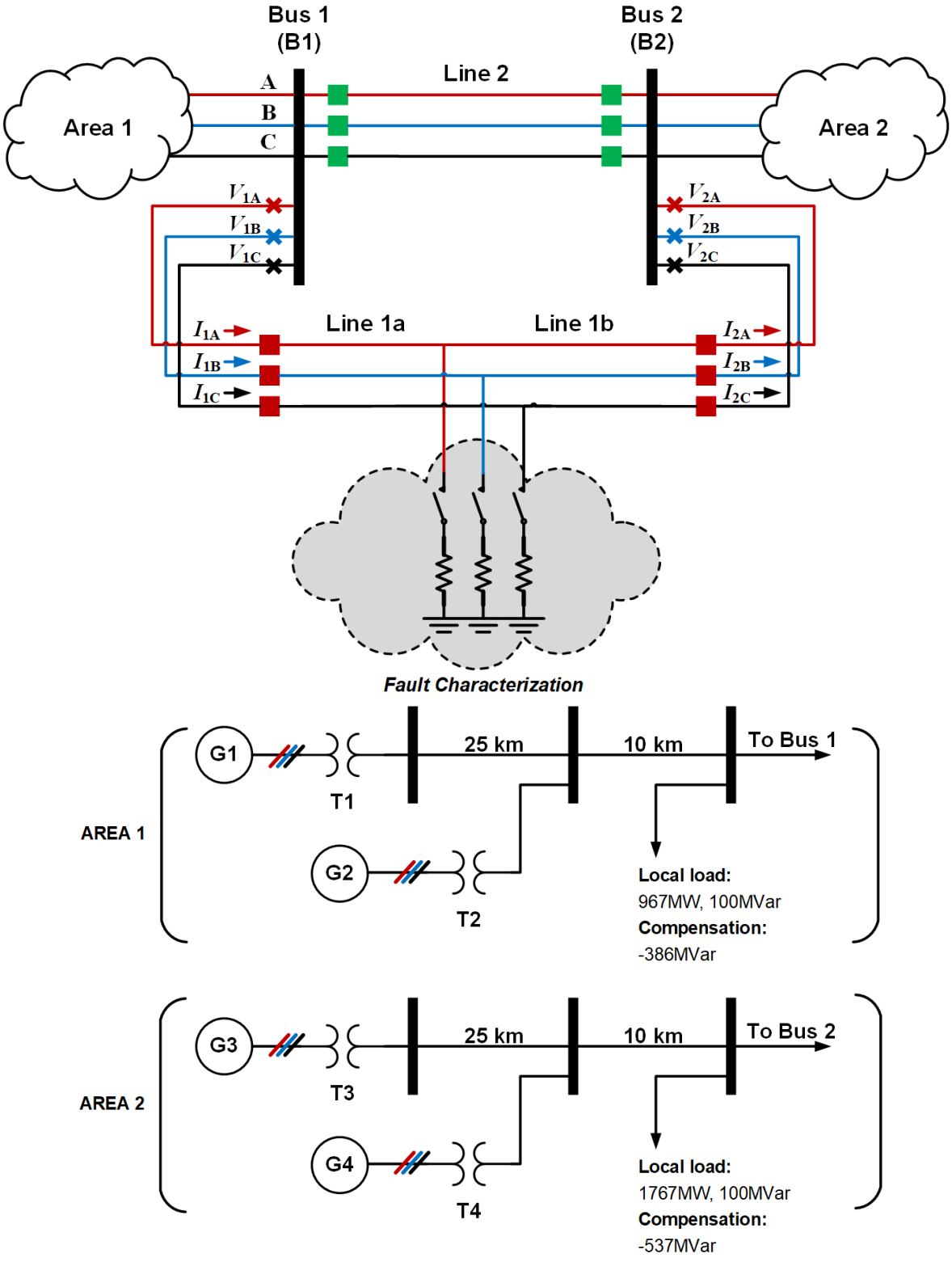

Figure 33 Topology of test power system and voltage/current measurement points

Table 13. Application Test Use Case Specifications

Event Attributes	Attribute Values		
Fault Location Application [138] – Test Use Cases 1,2,3			
Disturbance Specifications	Fault Location	Test use case 1	20% from Bus 1 on Line 1
		Test use case 2	50% from Bus 1 on Line 1
		Test use case 3	80% from Bus 1 on Line 1
	Fault	Type	A-B-C
		Inception	1s
		Duration	10 cycles *
Circuit Breaker (CB) Operation Specs.	CB1	Operation	5 cycles
		Reclose	12 cycles
	CB2	Operation	6 cycles
		Reclose	12 cycles
Measurements	Three phase Bus 1 and Bus 2 voltages Three phase Line 1 currents from sending (Bus 1) and receiving (Bus 2) ends Phasor reporting rate: 120Hz		
Simulation Time	2 seconds		
Oscillation Detection Application [139] – Test Use Case 4			
Disturbance Specifications	Fault 1	Location	50%, on Line 1
		Type	A-B-C
		Inception	20s
		Duration	10 cycles
	Fault 2	Location	10 km from Bus2 Area 2
		Type	A-B-C
		Inception	150s
		Duration	10 cycles
Circuit Breaker (CB) Operation Specs.	CB1	Operating	5 cycles
		Reclosing	12 cycles
	CB2	Operating	6 cycles
		Reclosing	12 cycles
Measurements	Three phase Bus 1 voltages Phasor reporting rate: 60Hz		
Simulation Time	600 seconds		

* cycles post fault, the same hereinafter in this Table

Table 14. Transmission Line Parameters in Application Test Use Case Model Depicted in Figure 33

Component Type	Parameters		
	Positive Sequence	Zero Sequence	Unit
Resistance	0.01273	0.3864	Ω/km
Inductance	0.9337	4.1264	mH/km
Capacitance	12.74	7.751	μF/km
Total Length	220		km

9.2.2.3. Test Use Case Waveforms

Time-domain waveforms are generated for fault location and oscillation detection application test use cases, as illustrated in Figure 34 and Figure 35, respectively.

Figure 34 illustrates the electromagnetic transient waveforms after the three-phase faults associated with the test use cases 3 in Table 13. The waveforms for test use cases 1 and 2 are similar in waveform attributes: voltage waveforms exhibit transient undervoltage and harmonic components during fault; current waveforms show overcurrent, decaying DC and harmonic components.

Figure 35 depicts the Phase A voltage electromechanical dynamic waveform associated with test use case 4 shown in Table 13. The oscillation waveform model used in the derivation of oscillation detection application [139] is a single-phase amplitude modulation signal as modeled in [10]. Therefore, in this Dissertation, a single-phase voltage waveform is used as the application input, and Phase A measurement data are used as an example. For a clearer depiction of the dynamics, Phase B and C data are not shown in Figure 35. The test procedures can be replicated for Phase B and Phase C data as well. The simulation shows sustained electromechanical oscillation induced by faults. A closer study into signal features shows oscillations with an amplitude

modulation level of as much as 3% (w.r.t. mean voltage amplitude post fault), a frequency oscillation around 60.15Hz with an oscillation level of 0.02Hz; both amplitude and frequency oscillate at a frequency of approximately 0.4Hz.

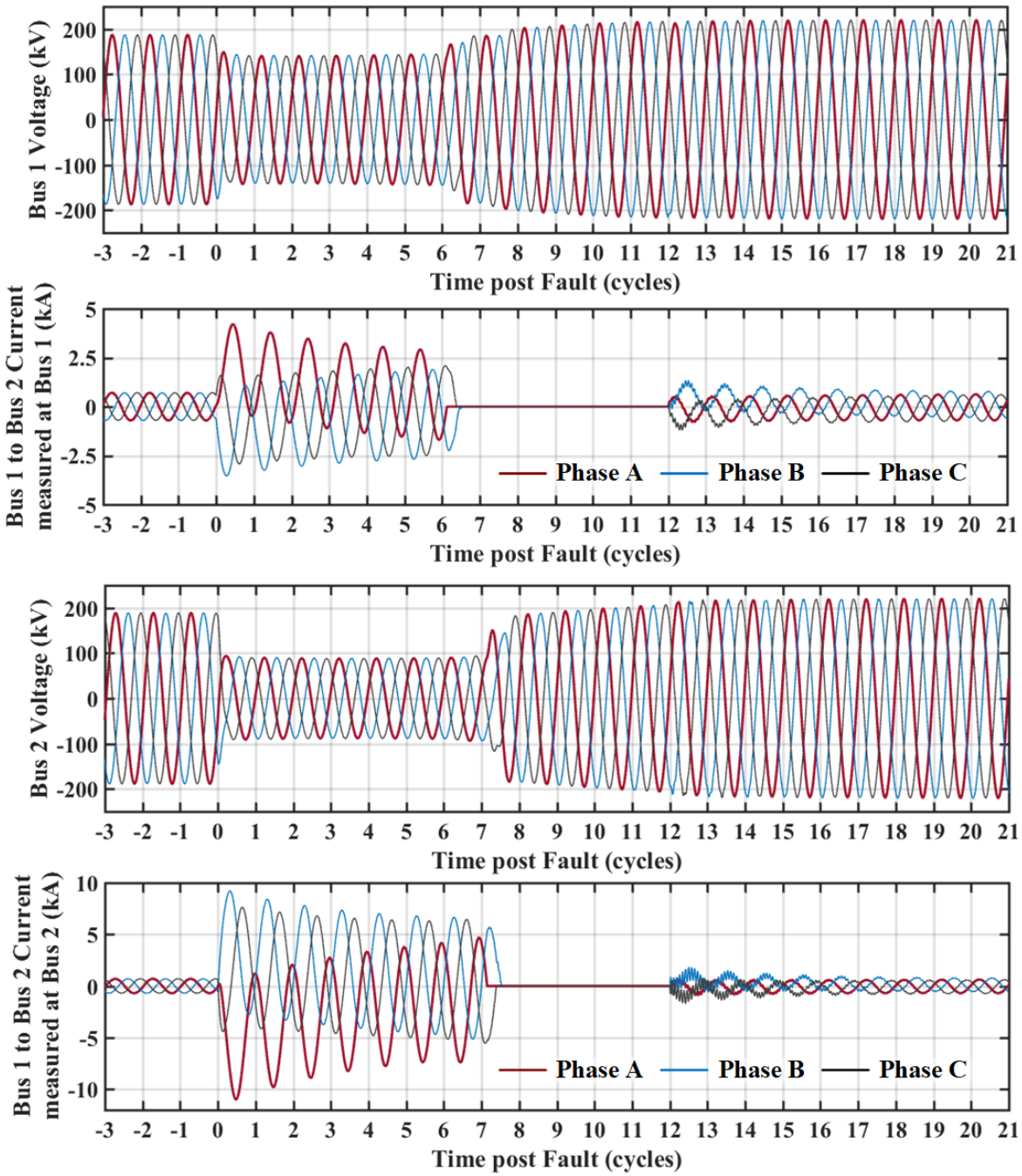

Figure 34 Test voltage and current waveforms for 80% fault location application test use cases measured at sending (Bus 1) and receiving (Bus 2) ends

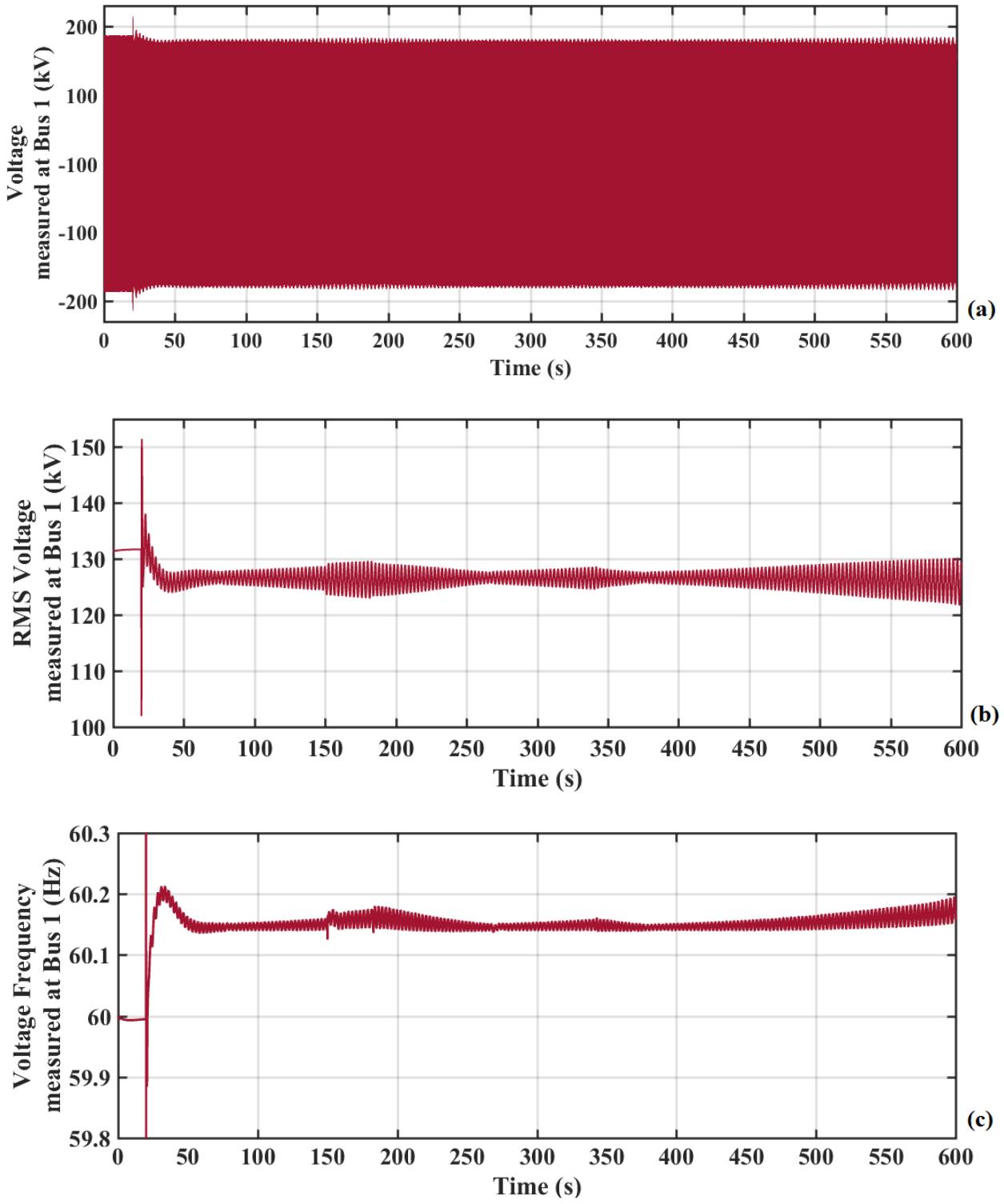

Figure 35 Phase A voltage test waveform, RMS value, and frequency for oscillation detection application test use cases

9.2.2.4. Characterization of Distortions in Phasor Communications

In realistic power system scenarios, various types of distortions may occur in the communication system and related devices located between the output of phasor algorithms (PMU) and the input to the applications. Phasor Data Concentrator (PDC) and communication network, shown in Figure 3, are among the sources of such distortions. The inaccuracies in phasor data may propagate to downstream applications, adversely affecting application performance. Therefore, the extent of distortion impact on application performances needs to be assessed.

In order to demonstrate the assessment of the impact of phasor stream distortions on the performance of an application, arbitrary distortions are chosen in the application testing strategy. Two types of distortions are considered, and they are phasor data packet misalignment in PDC, and phasor data packet loss in communication channels. The distortions are specified in Table 15. These two types of communication network distortion are superimposed on fault location and oscillation detection application test use cases, and are further described below.

Table 15. Specification of Distortion in Calculated Phasor Parameters

Distortion Type	Specifications
Phasor data packet time misalignment in PDC	Phasor data packets are misaligned by 6 and 10 reporting intervals across the entire simulation time. No data rejection occurs.
Phasor data packet loss in communication network	6 and 15 data packets per second are randomly deleted and replaced with zeros. The exact locations of lost packets are determined by a uniformly distributed pseudorandom integer command in MATLAB, `randi`.

- Phasor data packet timestamp misalignment

Phasor packet time alignment is one of the fundamental functions of a PDC [140]. It requires aggregating time synchronized data with matching timestamps from multiple PMUs or

PDCs. Accurate timestamp alignment is crucial to applications that rely on time-synchronized phasor parameters from multiple PMUs/PDCs, such as power system protection and control applications.

Timestamp misalignment may be caused by faulty PMUs/PDCs, or distortions such as clock drift, and cyber-attacks. Under these distortions, a PMU's timestamp may not match other PMU's timestamps, resulting in data rejection. Two scenarios of time misalignment are discussed, as shown in Figure 36.

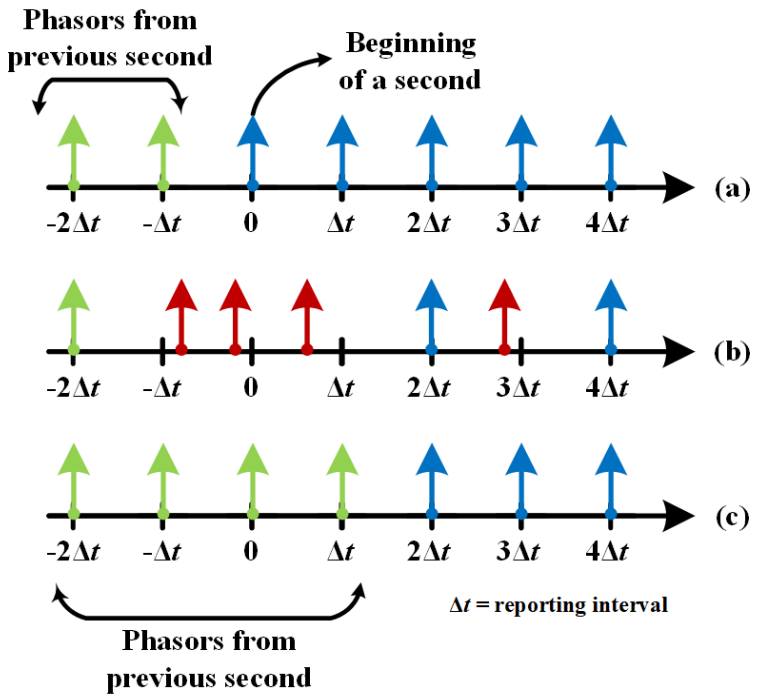

Figure 36 Illustration of phasor packet time-misalignment

(a) Normal phasor packets without time-misalignment; (b) Time-misalignment causing data rejection (rejected data in Red); (c) Time-misalignment that does not result in data rejection

As shown in Figure 36 (a), complying with standards [10] and [11], phasor packets are "expected" to be time-stamped at fractions of a second, which are equivalently multiples of reporting intervals. In the case depicted in Figure 36 (b), the phasor packets whose timestamps fall between reporting times are rejected. When the altered phasor timestamps still match other PMUs, as is in case depicted in Figure 36 (c), the phasor packets will not be rejected, and will be used by applications as they normally would.

Since limited number of phasors are available for fault location calculation prior to circuit breaker operation, i.e., 2 per cycle for 5 or 6 cycles, the time misalignment in case (c) with no data rejection is used for use case demonstration.

- Phasor data packet loss in communication network

Phasor data packets may be lost in the communication network due to network uncertainties, such as data transmission congestion and consequent data dropout [141].

The impact of phasor data packet loss on oscillation detection application is studied further. Sporadic data packet loss is simulated, as shown in Table 15. The lost data is replaced with zeros.

9.3 Test Results, Evaluation and Outcomes of Hypothesis Validation

9.3.1. The Methodology and Metrics for Result Evaluation

9.3.1.1. Design Tests

The performance of the algorithm is evaluated by comparing the calculated values by the proposed algorithm against the reference values defined by the metrics. Two metrics are used in the Design Test: Total Vector Error (TVE), and Frequency Error (FE), as defined in Equations (9.1) and (9.2) [10], respectively.

$$TVE(n) = \sqrt{\frac{\left[\hat{X}_r(n) - X_r(n)\right]^2 + \left[\hat{X}_i(n) - X_i(n)\right]^2}{[X_r(n)]^2 + [X_i(n)]^2}} \quad (9.1)$$

where,

$\hat{X}_r(n)$ and $\hat{X}_i(n)$ are the real and imaginary PMU estimates at reporting time n;

$X_r(n)$ and $X_i(n)$ are the real and imaginary reference values at reporting time n;

n is the reporting number representing the reporting time in a phasor stream time series

$$FE(n) = f_{\text{measured}}(n) - f_{\text{reference}}(n) \quad (9.2)$$

where,

n is the reporting number representing the reporting time in a phasor stream time series

Related TVE and |FE| expectations are specified in the standard for P-class and M-class PMUs, as outlined in Table 16.

Table 16. Algorithm Accuracy Requirements for Design Tests

Test Type	Test Conditions	TVE Limits		|FE| Limits (Hz)	
		P class	M class	P class	M class
Signal frequency variation	See Table 9	1%	1%	0.005	0.005
Signal amplitude variation		1%	1%	0.005	0.005
Single harmonic distortion		1%	1%	0.005	0.025
Out-of-band interference		N/A	1.3%	N/A	0.01
Amplitude modulation		3%	3%	0.06	0.3
Frequency modulation		3%	3%	0.06	0.3
System frequency ramp		1%	1%	0.01	0.01

For step tests, additional metrics are used to characterize the algorithm's step response tracking capability and transition period. This metrics are defined in [10], and shown in Figure 37, and the requirements are outline in Table 17.

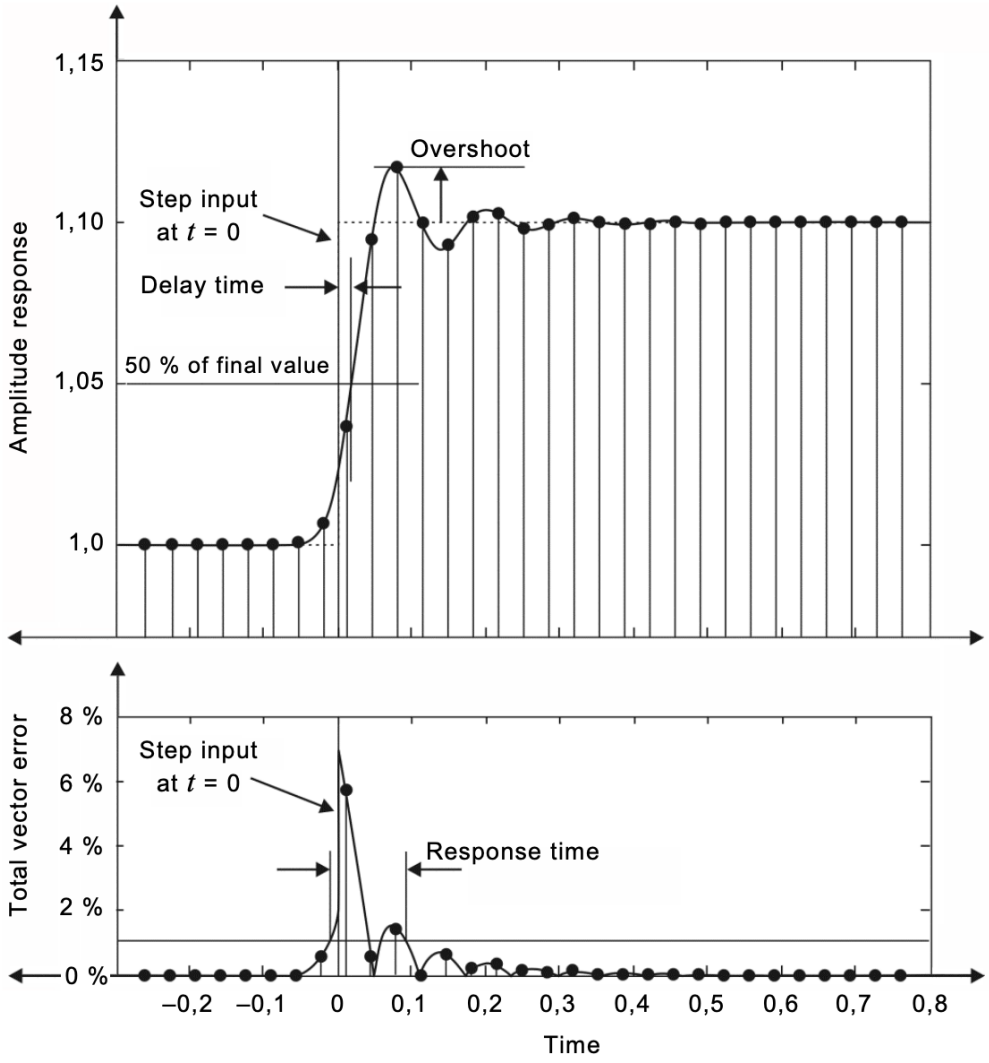

Figure 37 Definition of step test metrics [10]

Table 17. Performance Requirement for Design Tests – Step Change Tests

Test Type	Test Conditions	Error Limits					
		P class			M class		
		RT	|DT|	O/U	RT	|DT|	O/U
Magnitude step	See Table 9	$2/f_0$	$1/(4F_s)$	5% of step mag.	max $\{7/f_0, 7/F_s\}$	$1/(4F_s)$	10% of step mag.
Angle step		$2/f_0$	$1/(4F_s)$	5% of step mag.	max $\{7/f_0, 7/F_s\}$	$1/(4F_s)$	10% of step mag.

RT: Response time
DT: Delay time
F_s: Reporting frequency
O/U: Max overshoot/undershoot

9.3.1.2. Application Tests

The application test entails two points of comparison: a) application input phasor parameters (test use case waveforms filtered by the algorithm), and b) application performance caused by the algorithm error impact. The reasons are outlined below:

(1) An application waveform, produced in a software simulation, is associated with a power system test use case. The waveform is fed to the PMU algorithm, whose output, i.e., phasor parameters, are in turn fed to an application, which produces an application outcome. It is important to make sure the synchrophasor, if corrupted after it has been passed from the source PMU through PDC and communication network still preserves acceptable accuracy when compared to the reference;

(2) The impact of algorithm accuracy performance and phasor communication distortion on the outcome of an application is evaluated through a sensitivity analysis.

(3) In both cases, a phasor calculation results from a recently published algorithm [36],[142] will serve as the reference for the impact evaluation. Unlike the proposed algorithm, the reference algorithm adopts the same signal model for all types of event waveforms.

(4) The comparison results obtained by applying the proposed metrics at both comparison points are summarized in Table 18 in Section 9.3.1.6.

9.3.1.3. Test Methodology and Metrics Definition for Application Input Waveform Comparison

Through phasor parameter estimation algorithms, the features of interest from an application waveform $x(t)$, i.e., phasor parameters, are extracted. Therefore, phasor parameter calculation has a sense of data filtering. At the input of an application, it is important to make sure that the application waveform is not corrupted in the communication network. In this Dissertation, Average Waveform Error % is design as the metric to measure the distortion of synchrophasors

that are passed from the source PMU through PDC and communication network, as defined in Equation (9.3). Average Waveform Error % quantifies the average discrepancy of the filtered waveform from the original waveform throughout the entire time period under analysis. A smaller values indicates lower level of waveform corruption in the filtering process of an algorithm.

$$\text{Average Waveform Error \%} = \frac{\|\boldsymbol{x}_{\text{recovered}} - \boldsymbol{x}_{\text{simulation}}\|_1 / N}{V_{\text{nominal}}} \times 100\% \quad (9.3)$$

where,

$\boldsymbol{x}_{\text{recovered}}$ is the waveform sample vector recovered from the calculated phasor parameters:

$$\boldsymbol{x}(n)_{\text{recovered}} = \boldsymbol{A}(n)_{\text{calculated}} \cos[2\pi \boldsymbol{f}(n)_{\text{calculated}} \boldsymbol{t} + \boldsymbol{\varphi}(n)_{\text{calculated}}]$$

n is the reporting number representing the reporting time in a phasor stream time series

$\boldsymbol{x}_{\text{simulation}}$ is the simulated time-domain waveform sample vector

$\|\boldsymbol{y}\|_1$ is the 1-norm of vector $\boldsymbol{y} = [y_1, y_2, \ldots, y_N]^{\mathbf{T}}$, defined as:

$$\|\boldsymbol{y}\|_1 = \sum_{i=1}^{N} |y_i|$$

N is the total number of samples in the waveform

V_{nominal} is the nominal voltage of the bus voltage, 230kV

9.3.1.4. Test Methodology and Metrics Definition for Fault Location Application Performance Assessment

This application testing strategy is intended to evaluate algorithm performance under electromagnetic transient conditions. Particularly, this evaluation is presented in terms of the impact of the proposed algorithm's accuracy on fault location outcomes, where the calculated phasor streams are subject to communication distortion, such as phasor misalignment. The fault

location technique in paper [138] is selected as the phasor-based application. Three fault location test use cases that are simulated assume faults at 25%, 50%, and 80% the line length from the sending end (Bus 1), respectively.

The reference fault location is the actual fault location (in p.u.) as set up in the simulations. Fault Location Error %, defined in Equation (9.4), is used to measure the accuracy of the fault location algorithm:

$$\text{Fault Location Error \%}(n) = \left|\frac{\rho_{\text{calculated}}(n) - \rho_{\text{actual}}(n)}{\text{Total Line Length}}\right| \times 100\% \quad (9.4)$$

where,

$\rho_{\text{calculated}}$ is the calculated fault location in km

ρ_{actual} is the actual fault location in km, as set up in the simulation

n is the reporting number representing the reporting time in a phasor stream time series

The application outcomes using phasor streams from both the proposed algorithm and reference algorithm are compared to reference value, which is the actual fault location as set up in the simulation. A smaller Fault Location Error % value indicates better application performance, and thus higher phasor algorithm accuracy.

9.3.1.5. Test Methodology and Metrics Definition for Oscillation Detection Application Performance Assessment

This application testing strategy evaluates algorithm performance under electromechanical transient conditions.

The oscillation detection application [139] utilizes the self-coherence spectra of the input waveform to estimate oscillation frequencies. The recommended algorithm use case setup suggested in [139] is used. A total of 10-minute simulation data are used, with a data window length of 12 second and time delay of 6 second.

There is no "absolute reference" in an oscillation detection test use case that can be directly retrieved from the test system, compared to the use case of "actual fault location" in a fault location application test use case. As a result, in this oscillation detection test use case, a "relative reference" should be used. The "accurate application outcome" in this case should be the application outcome using the phasor parameters generated in the phasor-domain simulation during the electromechanical dynamic event. This test methodology is illustrated in Figure 38.

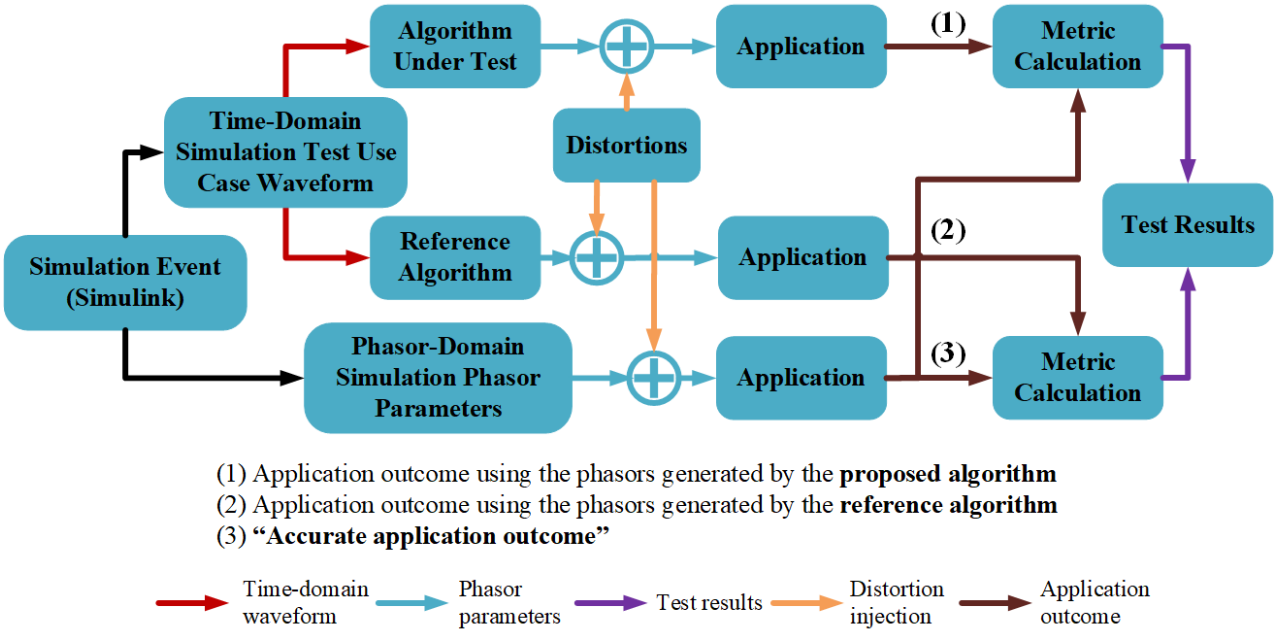

Figure 38 Test methodology for oscillation detection application

The metric Self Coherence Match %, as shown in equation (9.5), represents the percentage at which $\boldsymbol{\zeta}_{\text{calculated}}$ correctly matches $\boldsymbol{\zeta}_{\text{actual}}$. A higher percentage point indicates higher oscillation frequency detection performance, and therefore, the algorithm under test estimates phasor parameters with higher accuracy.

$$\text{Self Coherence Match } \%(n) = \frac{N\{\boldsymbol{\zeta}_{\text{calculated}} = \boldsymbol{\zeta}_{\text{actual}}\}}{N\{\boldsymbol{\zeta}_{\text{actual}}\}} \times 100\% \quad (9.5)$$

where,

$\boldsymbol{\zeta}_{\text{calculated}}$ is the self-coherence spectrum column vector calculated with phasors estimated by proposed algorithm or reference algorithm

$\boldsymbol{\zeta}_{\text{actual}}$ is the self-coherence spectrum column vector calculated with phasors produced by phasor-domain simulation

n is the reporting number representing the reporting time in a phasor stream time series

$N\{\boldsymbol{\zeta}_{\text{calculated}} = \boldsymbol{\zeta}_{\text{actual}}\}$ is the number of elements satisfying $\boldsymbol{\zeta}_{\text{calculated}} = \boldsymbol{\zeta}_{\text{actual}}$

$N\{\boldsymbol{\zeta}_{\text{actual}}\}$ is the number of element in array $\boldsymbol{\zeta}_{\text{actual}}$

9.3.1.6. Summary

The discussions in Section 9.3.1 is summarized in Table 18.

Table 18. Summary of Test Methodology and Metrics

<table>
<tr><th>Test Category</th><th>Metrics</th><th colspan="2">Methodology</th></tr>
<tr><td rowspan="2">Design Tests</td><td rowspan="2"><u>For non-step tests:</u>
Total Vector Error (TVE) [Equation (9.1)]
Frequency Error (FE) [Equation (9.2)]

<u>For step tests:</u>
Response time, delay time, overshoot/undershoot</td><td>Reference Phasor Values</td><td>Generated according to [10]</td></tr>
<tr><td>Comparing Method</td><td>Lower values of TVE and |FE| indicate higher algorithm accuracy</td></tr>
<tr><td rowspan="8">Application Tests</td><td>Waveform</td><td rowspan="2">Reference Outcomes</td><td rowspan="2">Simulation waveforms</td></tr>
<tr><td rowspan="2">Average Waveform Error % [Equation (9.3)]</td></tr>
<tr><td>Comparing Method</td><td>Lower values of Average Waveform Error % indicate higher algorithm accuracy</td></tr>
<tr><td>Fault Location</td><td rowspan="2">Reference Outcomes</td><td rowspan="2">The actual fault location according to simulation setups</td></tr>
<tr><td rowspan="2">Fault Location Error % [Equation (9.4)]</td></tr>
<tr><td>Comparing Method</td><td>Lower values of Fault Location Error % indicate higher algorithm accuracy</td></tr>
<tr><td>Oscillation Detection</td><td rowspan="2">Reference Outcomes</td><td rowspan="2">“Accurate application outcomes” as shown in Figure 38.</td></tr>
<tr><td rowspan="2">Self-Coherence Match % [Equation (9.5)]</td></tr>
<tr><td>Comparing Method</td><td>Higher values of Self-Coherence Match % indicate higher algorithm accuracy</td></tr>
</table>

9.3.2. Test Results Analysis and Hypothesis Validation

9.3.2.1. Test Result Analysis and Hypothesis Validation for Design Test Use Cases

Test results associated with design tests are tabulated in Table 19 and Table 20.

Table 19. Performance Requirements and Test Results for Design Tests – Non-Step Tests

Test Type	Performance Class	Standard Requirement [TVE/|FE| (Hz)]	Algorithm max TVE	Algorithm max |FE| (Hz)
Signal frequency variation	P class	1%/0.005	1e-2%	1e-4
	M class	1%/0.005	1e-2%	1e-4
Signal amplitude variation	P class	1%/0.005	1e-4%	1e-3
	M class	1%/0.005	1e-4%	1e-3
Single harmonic distortion	P class	1%/0.005	0.06%	1e-4
	M class	1%/0.025	0.06%	1e-4
Out-of-band interference	P class	N/A	N/A	N/A
	M class	1.3%/0.01	**3%**	1e-4
Amplitude modulation	P class	3%/0.06	1e-5%	1e-4
	M class	3%/0.3	1e-3%	1e-4
Frequency modulation	P class	3%/0.06	1e-3%	1e-2
	M class	3%/0.3	1e-3%	1e-2
System frequency ramp	P class	1%/0.01	1e-2%	1e-3
	M class	1%/0.01	1e-2%	1e-3

In each type of test, test signal parameters may vary during the test, based on Table 10 and Table 11. The values shown in Table 19 are the maximum error in each type of test. For example, in the P-class signal frequency test, test signal frequency varies from 58Hz to 62Hz, with an increment of 0.5Hz, resulting in 9 "subtests". The TVE and |FE| values are the highest calculation errors in these 9 subtests.

In amplitude and phase angle step test, an "interleaving procedure", recommended in the standard IEC/IEEE 60255-118-1, is applied. In order to achieve a time resolution smaller than one reporting interval, multiple step tests are conducted. In the first step test, the step function is adjusted so that the time of step falls on one of the reporting times. Successive step tests are conducted with step function triggered at increasing fractions of a reporting interval after the initial reporting time. The result of step test measurement points are interleaved by aligning all the steps

at the same starting point and averaging the measurements in each individual step tests. The step time of each individual step test is displaced by 1 sampling interval (1/6000s), thus one reported result at reporting rate 60Hz is an average of 100 step test results.

Table 20. Performance Requirements and Test Results for Design Tests – Step Tests

Test Type	Test Condi-tions	Error Limits					
		P class			M class		
		RT	|DT|	O/U	RT	|DT|	O/U
Magnitude step	See Table 9	$2/f_0$	$1/(4F_s)$	5% of step mag.	max $\{7/f_0, 7/F_s\}$	$1/(4F_s)$	10% of step mag.
Angle step		$2/f_0$	$1/(4F_s)$	5% of step mag.	max $\{7/f_0, 7/F_s\}$	$1/(4F_s)$	10% of step mag.

Test Type	Test Condi-tions	Test Results					
		P class			M class		
		RT	|DT|	O/U	RT	|DT|	O/U
Magnitude step	Positive step	1.5 cycle	1.6 cycle	0/**9.58**	1.5 cycle	1.6 cycle	0/**9.58**
	Negative step	1.5 cycle	0	0/**8.51**	1.5 cycle	0	0/**8.51**
Angle step	Positive step	0	0	0	0	0	0
	Negative step	0	0	0	0	0	0

RT: Response time
DT: Delay time
F_s: Reporting frequency
O/U: Max overshoot/undershoot

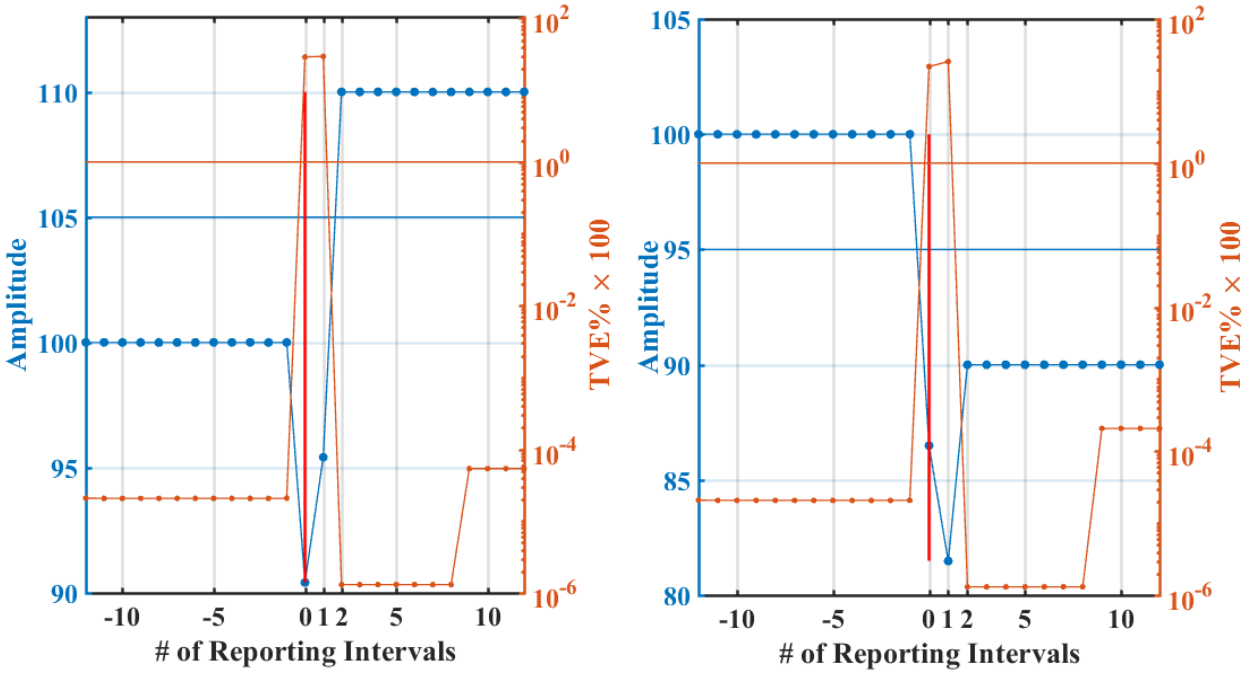

Figure 39 Amplitude step test results

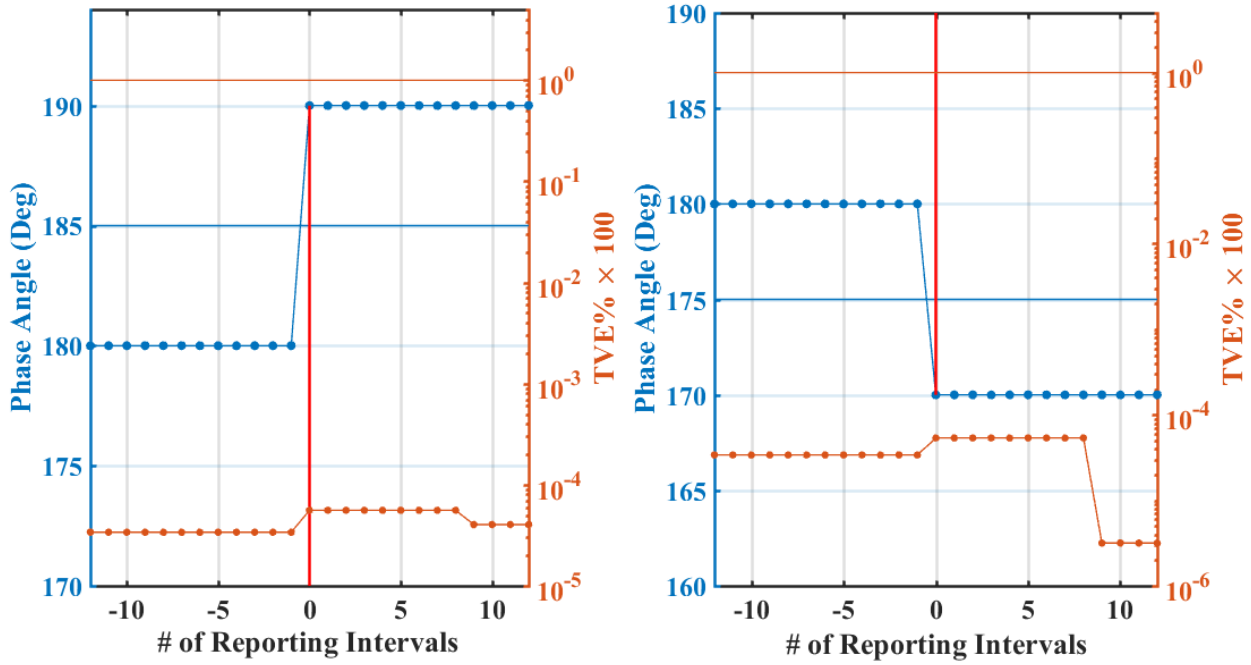

Figure 40 Phase angle step test results

As can be observed in Section 9.3.2.1, with the input waveform classification and adaptive phasor calculation algorithm switching mechanisms that we introduced, the proposed algorithm can achieve high accuracy under most test cases due to customized phasor parameter definition and algorithm modeling design.

However, from the test result data in Table 19, it is also revealed that the proposed algorithm fails to satisfy the TVE requirements in out-of-band test for M-Class tests. From Table 20, Figure 39 and Figure 40, it can be seen that the proposed algorithm has overshoot/undershoot in amplitude step tests. The reasons are discussed below.

As suggested in [143] and [144], passband flatness is required for optimal algorithm performance under the modulation tests; whereas stopband attenuation is needed for out-of-band test performance. As studied in Section 3.3 (window functions), in terms of FIR digital filter design, when the data window length is fixed, achieving optimal passband flatness and sharp transition from passband to stopband are contradicting requirements. The digital filter is applied at the front-end waveform sampling, and based on the out-of-band test result, this digital filter design does not achieve optimal passband attenuation.

It is suggested in [143] and [144] that a dedicatedly designed filter should be added at the output of the algorithm, before phasor decimation to the reporting frequency. As pointed out in [144], the overshoot/undershoot problem can be caused by the negative weights in data window coefficients. The shape of the digital window at the front end of the algorithm should be tailored to lower overshoot/undershoot levels.

Since the proposed algorithm does not fully satisfy the standard requirement, we believe that it is reasonable to validate the hypothesis by demonstrating that the proposed algorithm is able to show improvement in algorithm accuracy when compared to existing algorithms. Such

improvement is demonstrated by comparing the accuracy of phasor parameter calculation against existing algorithms, under the tests in which the proposed algorithm *does* show acceptable accuracy. The results are shown in Tables 21 and 22, where the performance of proposed algorithm is compared to 2 selected existing algorithms: DFT algorithm [24] and polynomial fitting algorithm [36].

Table 21. Estimation Error of Proposed Algorithm Compared to Selected Existing Algorithms – Max TVE

Test Type	Performance Class	Standard TVE Requirement	Algorithm TVE		
			Proposed Algorithm	DFT Algorithm	Curve-Fitting Algorithm
Signal frequency variation	P class	1%	1e-2%	**22.2%**	**100%**
	M class	1%	1e-2%	**53.5%**	**100%**
Signal amplitude variation	P class	1%	1e-4%	0	0
	M class	1%	1e-4%	0	0
Single harmonic distortion	P class	1%	0.06%	0	**1%**
	M class	1%	0.06%	0	**1%**
Amplitude modulation	P class	3%	1e-5%	2.5%	1.5%
	M class	3%	1e-3%	5%	2.65%
Frequency modulation	P class	3%	1e-3%	2.5%	0.5%
	M class	3%	1e-3%	**5%**	0.5%
System frequency ramp	P class	1%	1e-2%	**30%**	**100%**
	M class	1%	1e-2%	**70%**	**100%**

Table 22. Estimation Error of Proposed Algorithm Compared to Selected Existing Algorithms – Max |FE| *

Test Type	Performance Class	Standard |FE| Requirement	Algorithm |FE|		
			Proposed Algorithm	DFT Algorithm	Curve-Fitting Algorithm
Signal frequency variation	P class	0.005	1e-4	**5**	**5**
	M class	0.005	1e-4	**10**	**5**
Signal amplitude variation	P class	0.005	1e-3	0	0
	M class	0.005	1e-3	0	0
Single harmonic distortion	P class	0.005	1e-4	0	0
	M class	0.025	1e-4	0	0
Amplitude modulation	P class	0.06	1e-4	0	0
	M class	0.3	1e-4	0	0
Frequency modulation	P class	0.06	1e-2	0.001	**0.5**
	M class	0.3	1e-2	0.002	**0.5**
System frequency ramp	P class	0.01	1e-3	**6**	**10**
	M class	0.01	1e-3	**12.5**	**10**

* All values in Hz

From Tables 21 and 22, the following can be observed:

(1) In the design test cases where the proposed algorithm *does* show high accuracy, the selected reference algorithms do not satisfy all the test requirements;

(2) An algorithm is able to achieve high accuracy when its assumed algorithm signal model reflects and matches the underlying waveform characteristics. For example, the DFT algorithm models the input signal as a linear combination of DC and harmonic components of single-tone 60Hz signal. This modeling approach perfectly matches the test signals under signal amplitude variation and signal harmonic distortion tests, resulting in zero calculation error. In contrast, the DFT signal modeling does not reflect the dynamic fluctuations in signal amplitude and frequency, resulting in deterioration in algorithm accuracy;

(3) By incorporating waveform classification and algorithm switching mechanisms, the proposed algorithm can achieve consistent accuracy of at least 2 orders of magnitude higher than the standard requirements

Thus, from the aforementioned observations, it can be concluded that hypothesis is validated under the design test use cases because of the following reasons:

(1) The proposed algorithm's accuracy is higher than the selected existing algorithms in all cases;

(2) Higher algorithm accuracy can be achieved when the algorithm's signal modeling matches the underlying waveform features

9.3.2.2. Test Result Analysis and Hypothesis Validation for Application Test Use Cases

Test results are discussed for each application.

- Impact of Algorithm Accuracy on Fault Location Application Performance

The fault location algorithm utilizes time-synchronized bus voltage and line current phasor streams from both the sending and receiving end to calculate the fault location. As illustrated in Figure 41 as an example, during normal operating conditions, fault location application yields negative outcome; during fault, the calculated fault location turns positive and shows the estimated fault location in terms of the percentage length from the sending end.

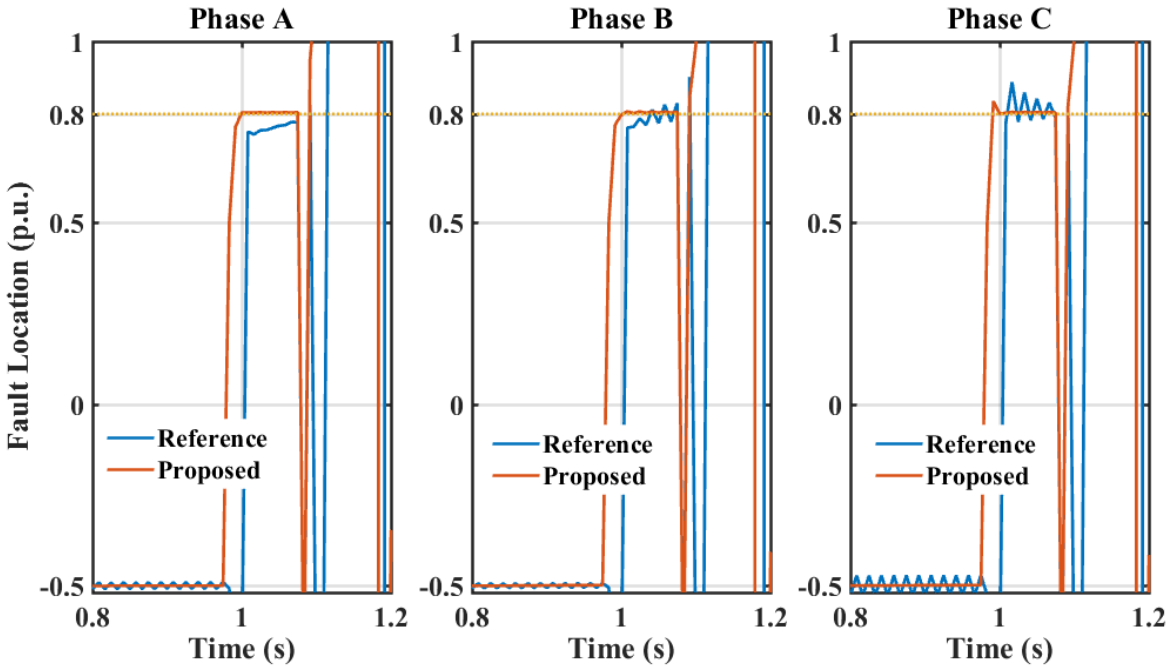

Figure 41 Fault location application result for 80% fault. No phasor packet distortion

Test results are summarized in Table 23 and 24.

Table 23. Application Test Results –
Impact of Phasor Data Packet Misalignment on Fault Location Application Performance *

Compared Quantity	Distortion Characteristics **	Average Waveform Error %	
		Proposed Algorithm	Reference Algorithm
Waveforms	No distortion	1.2% †	2.5%
	Misalignment by 6 reporting intervals	6.4%	7.4%
	Misalignment by 10 reporting intervals	13%	41%

Compared Quantity	Distortion Characteristics	Fault Location Error %		Actual Fault Location (p.u.)
		Proposed Algorithm	Reference Algorithm	
Application Outcomes	No distortion	0.35% ‡	15%	25%
		0.14%	0.73%	50%
		0.7%	8.8%	80%
	Misalignment by 6 reporting intervals	0.6%	6%	25%
		0.4%	14%	50%
		0.65%	12%	80%
	Misalignment by 10 reporting intervals	13%	90%	25%
		36%	68%	50%
		22%	38%	80%

* Phasor reporting rate is 120Hz
** Only Bus 1 measurements are distorted
† Percentage is w.r.t. nominal line voltage 230kV
‡ Percentage is w.r.t. to the total line length 220km

Table 24. Application Test Results –
Impact of Phasor Data Packet Loss on Fault Location Application Performance *

Compared Quantity	Distortion Characteristics **	Average Waveform Error %	
		Proposed Algorithm	Reference Algorithm
Waveforms	No distortion	1.2% †	2.5%
	Losing 6 data packets/second	90%	90%
	Losing 15 data packets/second	60%	60%

Compared Quantity	Distortion Characteristics	Fault Location Error %		Actual Fault Location (p.u.)
		Proposed Algorithm	Reference Algorithm	
Application Outcomes	No distortion	0.35% ‡	15%	25%
		0.14%	0.73%	50%
		0.7%	8.8%	80%
	Losing 6 data packets/second	1%	82%	25%
		0.25%	34%	50%
		0.45%	14%	80%
	Losing 15 data packets/second	1.1%	83%	25%
		0.25%	27%	50%
		0.15%	9%	80%

* Phasor reporting rate is 120Hz
** Only Bus 1 measurements are distorted
† Percentage is w.r.t. nominal line voltage 230kV
‡ Percentage is w.r.t. to the total line length 220km

From the fault location error data in Tables 23 and 24, it can be concluded that:

(1) Compared to the reference algorithm, the proposed algorithm results in lower Average Waveform Error % values under the selected types of communication network distortions. This proves that the filtering associated with the proposed algorithm has lower impact on waveform distortion, compared to the reference algorithm;

(2) Compared to the reference algorithm, the proposed algorithm results in lower values of Fault Location Error %, proving that the proposed algorithm inaccuracy

has a lower impact on fault location application performance, despite the presence of selected types of communication network distortions;

(3) Likewise, the fault location application performance is less sensitive to the selected types of communication network distortions, when utilizing the proposed algorithm phasor stream, compared to the reference algorithm phasor stream;

(4) And therefore, the proposed algorithm has lower impact on fault location application performance than the reference algorithm.

The hypothesis is thus validated for the application use case testing under electromagnetic dynamic event. This is done by showing that, compared to the reference algorithms, the proposed algorithm is less sensitive to synchrophasor corruption, and its inaccuracy has lower impact on fault location application performance.

- Impact of Algorithm Accuracy on Oscillation Detection Application Performance

The oscillation detection application uses the voltage phasors streamed by the PMU on Bus 1 to estimate the oscillation frequency. The test results are summarized in Tables 25 and 26.

Table 25. Application Test Results –
Impact of Phasor Data Packet Misalignment on Oscillation Detection Application Performance *

Compared Quantity	Distortion Characteristics	Average Waveform Error %	
		Proposed Algorithm	Reference Algorithm
Waveforms	No distortion	2.46%	3.34%
	Misalignment by 6 reporting intervals	2.47%	3.24%
	Misalignment by 10 reporting intervals	2.47%	3.17%
Compared Quantity	Distortion Characteristics	Average Self-Coherence Match %	
		Proposed Algorithm	Reference Algorithm
Application Outcomes	No distortion	98.61%	87.14%
	Misalignment by 6 reporting intervals	97.77%	85.85%
	Misalignment by 10 reporting intervals	97.43%	87.85%

* Phasor reporting rate is 60Hz

Table 26. Application Test Results –
Impact of Phasor Data Packet Loss on Oscillation Detection Application Performance *

Compared Quantity	Distortion Characteristics	Average Waveform Error %	
		Proposed Algorithm	Reference Algorithm
Waveforms	No distortion	2.46%	3.34%
	Losing 6 data packets/second	7.02%	7.82%
	Losing 15 data packets/second	12.99%	13.68%
Compared Quantity	Distortion Characteristics	Average Self-Coherence Match %	
		Proposed Algorithm	Reference Algorithm
Application Outcomes	No distortion	98.61%	87.33%
	Losing 6 data packets/second	98.63%	92.26%
	Losing 15 data packets/second	98.11%	91.96%

* Phasor reporting rate is 60Hz

As can be seen from Tables 25 and 26 the following can be summarized for the proposed algorithm:

(1) Compared to the reference algorithm, the proposed algorithm results in lower Average Waveform Error % values under the selected types of communication network distortions. This proves that the filtering associated with the proposed algorithm has lower impact on waveform distortion, compared to the reference algorithm;

(2) Compared to the reference algorithm, the proposed algorithm results in higher values of Self-Coherence Match %, demonstrating that the proposed algorithm inaccuracy has a lower impact on oscillation detection application performance, despite the presence of selected types of communication network distortions;

(3) Likewise, the oscillation detection application performance is less sensitive to the selected types of communication network distortions, when utilizing the proposed algorithm phasor stream, compared to the reference algorithm phasor stream;

(4) And therefore, the proposed algorithm has lower impact on the oscillation detection application than the reference algorithm.

The hypothesis is thus validated for the application use case testing under electromechanical dynamic event. This is done by showing that, compared to the reference algorithms, the proposed algorithm is less sensitive to synchrophasor corruption, and its inaccuracy has lower impact on oscillation detection application performance.

9.4 Conclusion

In this chapter, the hypothesis is validated through algorithm testing using design and application test use cases. The specification of test use cases, test procedures, test results, and result

evaluation metrics and methodologies are elaborated in this chapter. It is concluded that, in design and application test use cases, the hypothesis is validated under the caveats regarding some algorithm inaccuracy under special use case conditions elaborated below.

In design tests, it is concluded that the hypothesis is validated. This is done by showing the improvement on algorithm accuracy compared to the selected existing algorithms in the survey, against design test algorithm accuracy requirements. The design tests revealed that the proposed algorithm fails in TVE accuracy in out-of-band test (M-class) and overshoot level (amplitude step) are out of the range suggested by the standard [10], but is able to achieve a consistent accuracy of 2 orders of magnitude or higher than the standard requirements in other tests.

In Application Tests, various metrics are defined to evaluate the performance of proposed algorithm in term of the level of synchrophasor corruption caused by communication distortions, and the impact of algorithm inaccuracy on application performance. It is shown in 24.
Table 23 through Table 26 that, compared to the reference algorithm in [36], the proposed algorithm is less sensitive to synchrophasor corruption, and algorithm inaccuracy has lower impact on both fault location and oscillation detection application performances, despite the presence of communication network distortions. Therefore, under application test use cases, the hypothesis is validated.

To reiterate, this Dissertation hypothesized that phasor parameter calculation accuracy can be improved by tailoring phasor parameter definition and phasor parameter calculation approach based on the waveform features of events in the power system. As can be concluded in both the design and application test uses cases, the hypothesis is validated.

Final conclusions, a summary of the Dissertation contribution, and future work are outlined in the next chapter.

10. CONCLUSIONS

The characterization of dynamic events, particularly the extreme disturbances, is of fundamental significance to power system operation. With the growing deployment of PMUs and evolving application strategies for the use of synchrophasor data in the modern power grid, GPS-time synchronized waveform sampling and phasor parameter calculation techniques are becoming increasingly important in providing unequalled capacities in detecting extreme events and avoiding catastrophic consequences.

In this Dissertation, the waveform manifestations of electromagnetic and electromechanical dynamic events are extensively studied. Framework and algorithm are proposed to characterize power system operating conditions in terms of time-synchronized phasor parameters. In hypothesis validation, design test use cases are utilized to evaluate the performance of proposed algorithm under standardized tests. Application test use cases, test methodologies, and test metrics are defined to demonstrate the impact of algorithm inaccuracy and communication network distortion on application performance.

10.1 Summary of Dissertation Work

In Chapters 1 and 2, we discussed the features of SCADA system in monitoring power system operating conditions. We emphasized the shortcomings of SCADA system's inadequate measurement data accuracy and measurement data reporting resolution for the mitigation actions during extreme power system dynamic events. Then, we introduced the benefits of complementing SCADA system with synchrophasor system by incorporating time-synchronized waveform sampling technique and PMU algorithms. We concluded that synchrophasor phasor system is more advantageous than SCADA system in monitoring extreme dynamic events.

After examining and critiquing prior work of time-synchronized waveform sampling techniques and PMU algorithms in Chapter 3, hypothesis, as well as hypothesis validation approach, are proposed in Chapter 4. The hypothesis is that a higher phasor parameter calculation accuracy can be achieved through phasor parameter definition and algorithm design tailored to the match the features of each type of dynamic waveform.

In order to validate the hypothesis, PMU algorithm and hypothesis validation approach are studied and elaborated from Chapter 5 through Chapter 9. Power system dynamic events and dynamic waveform modeling are discussed in Chapter 5. The tools utilized in the proposed PMU algorithm are introduced and discussed from Chapter 6 to Chapter 8. The hypothesis validation is conducted through algorithm testing in Chapter 9 under both design and application test use cases. The main conclusions of this Dissertation work are summarized as follows:

(1) *Defining phasor parameters and tailoring PMU algorithm modeling to reflect and match the features of power system waveforms improve algorithm accuracy*:

It is proposed in the hypothesis that phasor parameter definition should reflect the features of power system waveforms, such as the variations in amplitude, angle, and frequency.

In order to validate this, we first proposed an algorithmic framework, outlined in Figure 9 in Chapter 6. The proposed framework enables differentiation between electromagnetic and electromechanical dynamic waveforms, and switches the algorithm between P-class and M-class mode as needed. By doing so, the proposed algorithm is able to achieve fast computational speed, as required for P-class PMUs under electromagnetic transients, and high calculation accuracy, as needed for M-class PMUs under electromechanical transients.

(2) *The time-frequency signature of a waveform can be used to distinguish various types of electromagnetic and electromechanical dynamic events*:

In order to validate this, we proposed a new time-frequency analysis tool, named "pseudo-wavelet" in Chapter 8, which is proven effective in extracting the time-frequency signatures from power system waveform samples. Such time-frequency features are then leveraged to detect the onset of electromechanical dynamics, categorize various types of electromechanical dynamic events, and enable adaptive algorithm switching mechanism.

Once the types of dynamic event is identified, we proposed customized phasor parameter definition and algorithm modeling to match different types of event, so that algorithm accuracy can be improved, compared to the surveyed existing algorithms. This is verified under the design test use cases in Chapter 9, where the improvement of algorithm accuracy is illustrated.

(3) *The algorithm accuracy during electromagnetic transients can be improved by adaptive spectral compensation according to the fundamental frequency of the power waveform*:

In order to validate this, we proposed a fundamental frequency estimator and DFT-based phasor calculation algorithm. Unscented Kalman Filter is used to reduce the estimation error due to prevalent noise. A spectral compensation technique is proposed to alleviate the error caused by DFT spectral leakage. The hypothesis validation in Chapter 9 proves that this approach is able to achieve high frequency estimation accuracy, and eliminate the impact of spectral leakage phenomenon caused by frequency deviation.

(4) *The impact of algorithm inaccuracy and communication network distortion on the end-use applications should be evaluated, and such impact should be used as one of the metrics of algorithm accuracy*:

The Dissertation discussed the approach of assessing algorithm accuracy in terms of the impact on the performance of applications. We designed application test use cases, and proposed test procedure, test methodology, and performance evaluation metrics for application testing

strategy. The application test results in Chapter 9 validated the hypothesis by showing better application performance with phasors calculated using the proposed algorithm.

(5) *Time-synchronized waveform sampling is key to algorithm accuracy*: The fault location application test use case in Chapter 9 assesses the impact of phasor data time-misalignment on fault location application performance. It is shown that the performance of fault location application deteriorates as time-misalignment among the phasor data increases. As expected, accurate time-synchronization is key to the accuracy determination of phasor parameters and electrical quantities associated with multiple locations in the power grid.

To summarize, the hypothesis of this Dissertation is validated in the tests

10.2 Dissertation Contributions

Compared to prior research, the Dissertation work contributions are:

(1) The Dissertation hypothesis contributes to specification and implementation of a new algorithm design framework, shown in Figure 9, which leads to a single PMU algorithm that is able to achieve consistent accuracy under various dynamic power system conditions. The proposed framework, by utilizing the input waveform detection and classification tool, adaptively switches the most appropriate signal modeling to match the input signal type, thus results in higher accuracy under various power system events than any single algorithm proposed in the literature survey.

(2) The Dissertation proposed framework, shown in Figure 7, fundamentally eliminates the impact of frequency leakage to DFT-based algorithm accuracy. A spectral compensation technique is developed to fully compensate the phasor calculation errors attributed to spectral leakage. The level of spectral compensation is adaptively tuned to the actual power system

fundamental frequency, estimated by the proposed, noise-resistant, UKF-based frequency estimator. In order to model the exponentially decaying DC component that may be present in the input signal, the Dissertation proposes a hybridization framework that models the DC component in terms of polynomial terms, preventing it from leaking into the DFT bin components. The test results in Chapter 9 shows accurate phasor parameter calculation under electromagnetic transient signal input.

(3) The Dissertation also proposes a framework, shown in Figure 8, that leverages the capability to detect and classify the type of input signal, identified by the proposed waveform extraction and classification tool, to then adaptively match the signal model to the actual signal samples. This strategy, as shown in Chapter 9, achieves high accuracy under electromechanical dynamic signal input.

(4) Moreover, the proposed algorithmic framework in this Dissertation is future-proof. With the integration of new technologies such as distributed energy resources, the power system is expected to experience new dynamic events manifested as waveforms not observed nowadays. With the proposed algorithmic framework, the accuracy of phasor parameter calculation can be maintained by updating the waveform detection and classification features and algorithm features, which is a more efficient way than designing a new algorithm from scratch.

(5) The Dissertation also elaborated on the application testing strategy. Compared to the standardized design testing strategy, which is outlined in relevant standard such as [10], the application testing strategy is aimed to assess the impact of algorithm inaccuracy on the performance of end-use control applications. Application and design testing strategies together provide a more comprehensive evaluation of the PMU algorithm performance than design testing strategy alone.

10.3 Future Work

In design tests, the algorithm accuracy under out-of-band tests (M-class PMUs), and the amplitude overshoot/undershoot under amplitude step test should be further studied. As discussed in Section 9.3.2.1, the inaccuracy may stem from filter design issues.

We would like to propose two potential strategies in future work to further improve algorithm accuracy:

(1) *Designing and tuning the digital filters in the algorithm*. One pre-processing filter, i.e., data window, installed at the front end of the algorithm, to alleviate overshoot/undershoot in amplitude step tests. The other post-processing filter installed at the output of the algorithm to achieve phasor data decimation needs to be tuned to improve out-of-band test accuracy.

(2) *Design a waveform feature characterization and classification techniques that operates on-the-fly*. To match the input signal features with high accuracy, the algorithm could benefit from a specialized fast online signal feature analysis tool, such as frequency content analysis. The outcome of such input signal content analysis can be used to accurately select the matching PMU algorithm, as well as tuning the PMU algorithm parameters on-the-fly. The implication may be that such dedicated mechanism can cause extra delay to the algorithm. Therefore, care should be taken in assessing the usefulness of such technique in applications requiring fast vs. slow response time.

REFERENCES

[1] A. Monticelli, "Electric power system state estimation," in *Proceedings of the IEEE*, vol. 88, no. 2, pp. 262-282, Feb. 2000.

[2] D. Kumari and S. P. Bhattacharyya, "A data-driven approach to power system dynamic state estimation," *2017 19th International Conference on Intelligent System Application to Power Systems (ISAP)*, San Antonio, TX, pp. 1-6, Sep. 2017.

[3] M. Kezunovic, "Future trends in protective relaying, substation automation, testing and related standardization," *IEEE/PES Transmission and Distribution Conference and Exhibition*, Yokohama, Japan, pp. 598-602, Oct. 2002.

[4] C. A. Ordonez, H. R. Chamorro, J. Quintero, R. Leelaruji, J. C. Peng and L. Nordström, "Prony-based on-line oscillation detection with real PMU information," *2016 IEEE Colombian Conference on Robotics and Automation (CCRA)*, Bogota, pp. 1-5, Sep. 2016.

[5] O. Samuelsson and N. Strath, "Islanding detection and connection requirements," *2007 IEEE Power Engineering Society General Meeting*, Tampa, FL, pp. 1-6, Jun. 2007.

[6] I. J. Balaguer, Q. Lei, S. Yang, U. Supatti and F. Z. Peng, "Control for grid-connected and intentional islanding operations of distributed power generation," in *IEEE Transactions on Industrial Electronics*, vol. 58, no. 1, pp. 147-157, Jan. 2011.

[7] "IEEE Standard for SCADA and Automation Systems," in *IEEE Std. C37.1-2007 (Revision of IEEE Std. C37.1-1994)*, pp.1-143, May 2008.

[8] National Institute of Standards and Technology (NIST) SP 800-82. Guide to Industrial Control System (ICS) System Security. June 2011. [Online]. Available: https://nvlpubs.nist.gov/nistpubs/specialpublications/nist.sp.800-82r2.pdf.

[9] IEEE Standard for Synchrophasor Measurements for Power Systems -- Amendment 1: Modification of Selected Performance Requirements," in *IEEE Std C37.118.1a-2014 (Amendment to IEEE Std C37.118.1-2011)*, pp.1-25, April 2014.

[10] IEEE/IEC International Standard - Measuring relays and protection equipment - Part 118-1: Synchrophasor for power systems - Measurements," in *IEC/IEEE 60255-118-1:2018*, pp.1-78, Dec. 2018.

[11] IEEE Standard for Synchrophasor Data Transfer for Power Systems," in *IEEE Std. C37.118.2-2011 (Revision of IEEE Std. C37.118-2005)*, pp.1-53, Dec. 2011.

[12] “August 14, 2003 blackout: NERC actions to prevent and mitigate impacts of future cascading blackouts”. [Online]. Available: https://www.nerc.com/comm/PC/System%20Protection%20and%20Control%20Subcommittee%20SPCS%20DL/NERC_Recommendations_2-10-04.pdf.

[13] “August 14, 2003 outage, sequence of events, FERC, US/Canada power outage task force, 9/12/03”. [Online]. Available: https://www.ferc.gov/sites/default/files/2020-05/09-12-03-blackout-sum.pdf.

[14] “Arizona-Southern California outages on September 8, 2011: causes and recommendations”. [Online]. Available: https://www.nerc.com/pa/rrm/ea/September%202011%20Southwest%20Blackout%20Event%20Document%20L/AZOutage_Report_01MAY12.pdf.

[15] “Phase angle monitoring industry experience following the 2011 Pacific Southwest outage recommendation 27”. [Online]. Available: https://www.nerc.com/comm/PC/Synchronized%20Measurement%20Subcommittee/Phase%20Angle%20Monitoring%20Technical%20Reference%20Document%20-%20FINAL.pdf.

[16] F. F. Wu, K. Moslehi and A. Bose, "Power system control centers: past, present, and future," in *Proceedings of the IEEE*, vol. 93, no. 11, pp. 1890-1908, Nov. 2005.

[17] A. G. Phadke and B. Kasztenny, "Synchronized phasor and frequency measurement under transient conditions," in *IEEE Transactions on Power Delivery*, vol. 24, no. 1, pp. 89-95, Jan. 2009.

[18] QPS. “UTC to GPS time correction”. [Online]. Available: https://confluence.qps.nl/qinsy/en/utc-to-gps-time-correction-32245263.html.

[19] NIST Physical Measurement Laboratory, Time and Frequency Division. “Radio station WWVB”. [Online]. Available: https://www.nist.gov/pml/time-and-frequency-division/radio-stations/wwvb.

[20] NIST Physical Measurement Laboratory, Time and Frequency Division. “Help with WWVB radio controlled clocks”. [Online]. Available: https://www.nist.gov/pml/time-and-frequency-division/radio-stations/wwvb/help-wwvb-radio-controlled-clocks.

[21] “GPS system overview”. [Online]. Available: https://www.gps.gov/systems/gps/.

[22] M. G. Shayesteh and M. Mottaghi-Kashtiban, "FIR filter design using a new window function," *16th International Conference on Digital Signal Processing*, Santorini-Hellas, pp. 1-6, Jul. 2009.

[23] F. J. Harris, "On the use of windows for harmonic analysis with the discrete Fourier Transform," in *Proceedings of the IEEE*, vol. 66, no. 1, pp. 51-83, Jan. 1978.

[24] A. G. Phadke, J. S. Thorp and M. G. Adamiak, "A new measurement technique for tracking voltage phasors, local system frequency, and rate of change of frequency," in *IEEE Transactions on Power Apparatus and Systems*, vol. PAS-102, no. 5, pp. 1025-1038, May 1983.

[25] A.G. Phadke, J.S. Thorp. "Synchronized phasor measurements and their applications". New York, Springer, Aug. 2008.

[26] M. T. Heath, "Scientific computing: an introductory survey, Chapter 7 – interpolation". [Online]. Available: http://heath.cs.illinois.edu/scicomp/notes/chap07.pdf.

[27] T. Grandke, "Interpolation algorithms for Discrete Fourier Transforms of weighted signals," in *IEEE Transactions on Instrumentation and Measurement*, vol. 32, no. 2, pp. 350-355, Jun. 1983.

[28] D. Macii, D. Petri and A. Zorat, "Accuracy analysis and enhancement of DFT-based synchrophasor estimators in off-nominal conditions," in *IEEE Transactions on Instrumentation and Measurement*, vol. 61, no. 10, pp. 2653-2664, Oct. 2012.

[29] D. Belega and D. Petri, "Accuracy analysis of the multicycle synchrophasor estimator provided by the interpolated DFT algorithm," in *IEEE Transactions on Instrumentation and Measurement,* vol. 62, no. 5, pp. 942-953, May 2013.

[30] P. Romano and M. Paolone, "Enhanced interpolated-DFT for synchrophasor estimation in FPGAs: theory, implementation, and validation of a PMU prototype," in *IEEE Transactions on Instrumentation and Measurement*, vol. 63, no. 12, pp. 2824-2836, Dec. 2014.

[31] R. Ferrero, P. A. Pegoraro and S. Toscani, "Employment of interpolated DFT-based PMU algorithms in three-phase systems," *2017 IEEE International Workshop on Applied Measurements for Power Systems (AMPS)*, Liverpool, pp. 1-5, Sep. 2017.

[32] C. Qian and M. Kezunovic, "Spectral interpolation for frequency measurement at off-nominal frequencies," *2017 IEEE Power & Energy Society General Meeting*, Chicago, IL, pp. 1-5, Jul. 2017.

[33] IEEE Guide for Protective Relay Applications to Transmission Lines, in *IEEE Std C37.113-2015 (Revision of IEEE Std C37.113-1999)* pp.1-141, Jun. 2016.

[34] J. A. de la O Serna, "Dynamic phasor estimates for power system oscillations," in *IEEE Transactions on Instrumentation and Measurement*, vol. 56, no. 5, pp. 1648-1657, Oct. 2007.

[35] M. Platas-Garza and J. A. de la O Serna, "Dynamic phasor and frequency estimates through maximally flat differentiators," in *IEEE Transactions on Instrumentation and Measurement*, vol. 59, no. 7, pp. 1803-1811, Jul. 2010.

[36] W. Premerlani, B. Kasztenny and M. Adamiak, "Development and implementation of a synchrophasor estimator capable of measurements under dynamic conditions," in *IEEE Transactions on Power Delivery*, vol. 23, no. 1, pp. 109-123, Jan. 2008.

[37] P. Castello, J. Liu, C. Muscas, P. A. Pegoraro, F. Ponci and A. Monti, "A fast and accurate PMU algorithm for P+M Class measurement of synchrophasor and frequency," in *IEEE Transactions on Instrumentation and Measurement*, vol. 63, no. 12, pp. 2837-2845, Dec. 2014

[38] J. Ren and M. Kezunovic, "An adaptive phasor estimator for power system waveforms containing transients," in *IEEE Transactions on Power Delivery*, vol. 27, no. 2, pp. 735-745, Apr. 2012.

[39] Hao Liu, Tianshu Bi and Qixun Yang, "The evaluation of phasor measurement units and their dynamic behavior analysis", in *IEEE Trans. Instrumentation and Measurements*, vol. 62, no. 6, pp. 1479-1485, Jun. 2013.

[40] C. Qian and M. Kezunovic, "Dynamic synchrophasor estimation with modified hybrid method," *2016 IEEE Power & Energy Society Innovative Smart Grid Technologies Conference (ISGT)*, Minneapolis, MN, pp. 1-5, Sep. 2016.

[41] G. N. Karystinos and D. A. Pados, "On overfitting, generalization, and randomly expanded training sets," in *IEEE Transactions on Neural Networks*, vol. 11, no. 5, pp. 1050-1057, Sep. 2000.

[42] C. Qian, T. Bi, J. Li, H. Liu and Z. Liu, "Synchrophasor estimation algorithm using Legendre polynomials," *2014 IEEE PES General Meeting | Conference & Exposition*, National Harbor, MD, pp. 1-5, Jul. 2014.

[43] B. Boashash, "Estimating and interpreting the instantaneous frequency of a signal. I. Fundamentals," in *Proceedings of the IEEE*, vol. 80, no. 4, pp. 520-538, Apr. 1992.

[44] B. Picinbono, "On instantaneous amplitude and phase of signals," in *IEEE Transactions on Signal Processing*, vol. 45, no. 3, pp. 552-560, Mar. 1997.

[45] P. M. Oliveira and V. Barroso, "Instantaneous frequency of multicomponent signals," in *IEEE Signal Processing Letters,* vol. 6, no. 4, pp. 81-83, Apr. 1999.

[46] IEEE Standard Definitions of Physical Quantities for Fundamental Frequency and Time Metrology--Random Instabilities, in *IEEE Std. 1139-2008 (Revision of IEEE Std. 1139-1999)*, pp.1-50, Feb. 2009.

[47] “Analytic signals and Hilbert Transform filters”. [Online]. Available: https://ccrma.stanford.edu/~jos/st/Analytic_Signals_Hilbert_Transform.html.

[48] T. Lobos and J. Rezmer, "Real-time determination of power system frequency," in *IEEE Transactions on Instrumentation and Measurement*, vol. 46, no. 4, pp. 877-881, Aug. 1997.

[49] H. Kirkham, W. Dickerson and A. Phadke, "Defining power system frequency," *2018 IEEE Power & Energy Society General Meeting (PESGM)*, Portland, OR, pp. 1-5, Aug. 2018.

[50] I. Knowles, R.J. Renka. "Methods for numerical differentiation of noisy data". [Online]. Available: https://ejde.math.txstate.edu/conf-proc/21/k3/knowles.pdf.

[51] A. Routray, A. K. Pradhan and K. P. Rao, "A novel Kalman filter for frequency estimation of distorted signals in power systems," in *IEEE Transactions on Instrumentation and Measurement*, vol. 51, no. 3, pp. 469-479, Jun. 2002.

[52] M. Mojiri, M. Karimi-Ghartemani and A. Bakhshai, "Estimation of power system frequency using an adaptive notch filter," in *IEEE Transactions on Instrumentation and Measurement*, vol. 56, no. 6, pp. 2470-2477, Dec. 2007.

[53] J. Bertsch, C. Carnal, D. Karlson, J. McDaniel and K. Vu, "Wide-area protection and power system utilization," in *Proceedings of the IEEE*, vol. 93, no. 5, pp. 997-1003, May 2005.

[54] S.M. Schoenung, W.V. Hassenzahl. "Characteristics and technologies for long vs. short-term energy storage: a study by the DOE Energy Storage Systems Program SAND2001-0765". [Online]. Available: https://prod-ng.sandia.gov/techlib-noauth/access-control.cgi/2003/032783.pdf.

[55] S. Takayama and R. Matsuhashi, "Development of model for load frequency control in power system with large-scale integration of renewable energy," *2016 IEEE Power and Energy Conference at Illinois (PECI)*, Urbana, IL, pp. 1-8, Feb. 2016.

[56] M.A. Ibrahim. "Disturbance analysis for power systems". Hoboken, N.J., Wiley: IEEE Press, Sep. 2012.

[57] P. Kundur, "Power system stability and control". New York: McGraw-Hill, Jan. 1994.

[58] P. Kundur, "Definition and classification of power system stability IEEE/CIGRE joint task force on stability terms and definitions," in *IEEE Transactions on Power Systems*, vol. 19, no. 3, pp. 1387-1401, Aug. 2004.

[59] P.W. Sauer, M.A. Pai. "Power system dynamics and stability". [Online]. Available: https://courses.engr.illinois.edu/ece576/sp2018/Sauer%20and%20Pai%20book%20-%20Jan%202007.pdf.

[60] J. McCalley. “Power system dynamic course, time constant”. [Online]. Available: http://home.engineering.iastate.edu/~jdm/ee554/TimeConstants.pdf.

[61] IEEE Guide for Synchronous Generator Modeling Practices and Applications in Power System Stability Analyses," in *IEEE Std 1110-2002 (Revision of IEEE Std 1110-1991)* , pp. 1-72, Nov. 2003.

[62] K. Sun. “Power system analysis course, short circuit and open circuit time constants”. [Online]. Available. http://web.eecs.utk.edu/courses/spring2018/ece522/ECE522_2.1-Modeling_gen_4.pdf.

[63] A. A. Renjit, M. S. Illindala, A. Mondal and D. A. Klapp, "Analysis and prevention of prime-mover stalling in a mixed source microgrid," *2016 IEEE International Conference on Power Electronics, Drives and Energy Systems (PEDES)*, Trivandrum, pp. 1-6, Sep. 2016.

[64] J. Machowski, J. Bialek and J. Bumby, “Power system dynamics: stability and control”, 3nd Edition, Wiley, Feb. 2020.

[65] E. Kurtz, G. Corcoran. “Introduction to electric transients”. John Wiley & Sons, Inc. New York, Jan. 1935. [Online]. Available: https://archive.org/details/in.ernet.dli.2015.166238/page/n6.

[66] H. Ghasemi and C. Canizares, "Damping torque estimation and oscillatory stability margin prediction," *2006 IEEE Power Engineering Society General Meeting*, Montreal, Que., pp. 6, Jun. 2006.

[67] “Spectral analysis via the DFT”. [Online]. Available: https://engineering.purdue.edu/~bouman/ece438/lecture/module_1/1.6_dft/1.6.3_spect_analys_via_dft.pdf.

[68] A.V. Oppenheim, R.W. Schafer. “Discrete-time signal processing”, 3rd Edition. Pearson, Jan. 2010.

[69] IEEE Standard for Synchrophasors for Power Systems," in *IEEE Std C37.118-2005 (Revision of IEEE Std 1344-1995)* , pp. 1-57, May 2006.

[70] C. Qian and M. Kezunovic, "Power system fundamental frequency estimation using Unscented Kalman Filter," *2019 IEEE Power & Energy Society General Meeting (PESGM)*, Atlanta, GA, USA, pp. 1-5, Aug. 2019.

[71] C. Qian and M. Kezunovic, "Hybridization framework for improved dynamic phasor parameter estimation algorithms," *2019 IEEE Power & Energy Society Innovative Smart Grid Technologies Conference (ISGT)*, Washington, D.C., pp. 1-5, Feb. 2019.

[72] J. K. Hwang and Y. Liu, "Noise analysis of power system frequency estimated from angle difference of Discrete Fourier Transform coefficient," in *IEEE Transactions on Power Delivery*, vol. 29, no. 4, pp. 1533-1541, Aug. 2014.

[73] A.H. Jazwinski. “Stochastic Processes and Filtering Theory”. Academic Press, Jan. 1970.

[74] R.E. Kalman. “A new approach to linear filtering and prediction problems”. [Online]. Available: http://www.cs.unc.edu/~welch/kalman/media/pdf/Kalman1960.pdf.

[75] G. Noriega and S. Pasupathy, "Application of Kalman filtering to real-time preprocessing of geophysical data," in *IEEE Transactions on Geoscience and Remote Sensing*, vol. 30, no. 5, pp. 897-910, Sep. 1992.

[76] S. Bittanti and S. M. Savaresi, "On the parametrization and design of an extended Kalman filter frequency tracker," in *IEEE Transactions on Automatic Control*, vol. 45, no. 9, pp. 1718-1724, Sep. 2000.

[77] M. S. Grewal and A. P. Andrews, "Applications of Kalman Filtering in aerospace 1960 to the present [historical perspectives]," in *IEEE Control Systems Magazine*, vol. 30, no. 3, pp. 69-78, Jun. 2010.

[78] F. Auger, M. Hilairet, J. M. Guerrero, E. Monmasson, T. Orlowska-Kowalska and S. Katsura, "Industrial applications of the Kalman Filter: a review," in *IEEE Transactions on Industrial Electronics*, vol. 60, no. 12, pp. 5458-5471, Dec. 2013.

[79] A. Saxena. “Kalman filter applications”. [Online]. Available: https://www.cs.cornell.edu/courses/cs4758/2012sp/materials/MI63slides.pdf.

[80] J. P. Muñoz, M. E. Magaña and E. Cotilla-Sanchez, "Adaptive master-slave Unscented Kalman Filter for grid voltage frequency estimation," in *IET Signal Processing*, vol. 12, no. 4, pp. 496-505, Jun. 2018.

[81] W. Wang, X. Wang, C. Xiang, C. Wei and Y. Zhao, "Unscented Kalman Filter-based battery SOC estimation and peak power prediction method for power distribution of hybrid electric vehicles," in *IEEE Access*, vol. 6, pp. 35957-35965, Jun. 2018.

[82] S.M. Kay. “Fundamentals of statistical processing, volume I: estimation theory”. Prentice Hall, Jan. 1993.

[83] R.G. Brown, P. Hwang. “Introduction to random signals and applied Kalman Filtering with MATLAB exercises and solutions”, 4th Edition. John Wiley & Sons, Feb. 2012.

[84] S. Haykin. “Adaptive filter theory”, 4th Edition. Prentice Hall, Upper Saddle River, New Jersey, Jan. 2002.

[85] A. Zaknich. “Principles of adaptive filters and self-learning systems”. Springer, Apr. 2005.

[86] X. Hu. “Discrete Kalman Filter”. [Online]. Available. https://www.math.kth.se/optsyst/grundutbildning/kurser/SF2832/Notes/Kalman_hu.pdf.

[87] G.A. Terejann. “Extended Kalman Filter tutorial”. [Online]. Available: https://www.cse.sc.edu/~terejanu/files/tutorialEKF.pdf.

[88] S. Boyd. “The Extended Kalman Filter”. [Online]. Available: https://stanford.edu/class/ee363/lectures/ekf.pdf.

[89] J.K. Uhlmann. “Dynamic map building and localization: new theoretical foundations”. [Online]. Available: http://faculty.missouri.edu/uhlmannj/Dissertation-pref.pdf.

[90] S. Julier, J. Uhlmann and H. F. Durrant-Whyte, "A new method for the nonlinear transformation of means and covariances in filters and estimators," in *IEEE Transactions on Automatic Control*, vol. 45, no. 3, pp. 477-482, Mar. 2000.

[91] S. J. Julier. “A skewed approach to filtering”. [Online]. Available: http://www.gatsby.ucl.ac.uk/~byron/paper.pdf.

[92] S. J. Julier, J.K. Uhlmann, "Consistent debiased method for converting between polar and cartesian coordinate systems," in *Proceeding SPIE 3086, Acquisition, Tracking, and Pointing XI*, Jul. 1997.

[93] S. J. Julier, J.K. Uhlmann. “A new extension of the Kalman Filter to nonlinear systems”. [Online]. Available: http://citeseerx.ist.psu.edu/viewdoc/download?doi=10.1.1.5.2891&rep=rep1&type=pdf.

[94] S. J. Julier, J.K. Uhlmann. “Unscented Filtering and nonlinear estimation”. [Online]. Available: https://www.cs.ubc.ca/~murphyk/Papers/Julier_Uhlmann_mar04.pdf.

[95] E.A. Wan, R. van der Merwe. “The Unscented Kalman Filter for nonlinear estimation”. [Online]. Available: https://www.seas.harvard.edu/courses/cs281/papers/unscented.pdf.

[96] G.A. Terejanu. “Unscented Kalman Filter tutorial”. [Online]. Available: https://www.cse.sc.edu/~terejanu/files/tutorialUKF.pdf.

[97] S.J. Julier, J.K. Uhlmann, “A consistent, debiased method for converting between polar and cartesian coordinate systems”. [Online]. Available:https://pdfs.semanticscholar.org/b347/0d801eb1bd16d4e835a0d930613ee80ac29e.pdf.

[98] C.D. Meyer. “Matrix analysis and applied linear algebra”, SIAM: Society of Industrial and Applied Mathematics, Jan. 2010.

[99] A. Routray, A. K. Pradhan and K. P. Rao, "A novel Kalman filter for frequency estimation of distorted signals in power systems," in *IEEE Transactions on Instrumentation and Measurement*, vol. 51, no. 3, pp. 469-479, Jun. 2002.

[100] H. M. T. Menegaz, J. Y. Ishihara, G. A. Borges and A. N. Vargas, "A systematization of the Unscented Kalman Filter theory," in *IEEE Transactions on Automatic Control*, vol. 60, no. 10, pp. 2583-2598, Oct. 2015.

[101] P. Regulski and V. Terzija, "Estimation of frequency and fundamental power components using an Unscented Kalman Filter," in *IEEE Transactions on Instrumentation and Measurement*, vol. 61, no. 4, pp. 952-962, Apr. 2012.

[102] Einstein Summation, from Wolfram MathWorld. [Online]. Available: http://mathworld.wolfram.com/EinsteinSummation.html.

[103] A. Einstein, “The foundation of the general theory of relativity”. [Online]. Available: https://web.archive.org/web/20060831163721/http://www.alberteinstein.info/gallery/pdf/CP6Doc30_English_pp146-200.pdf.

[104] J. Ren and M. Kezunovic, "A hybrid method for power system frequency estimation," in *IEEE Transactions on Power Delivery*, vol. 27, no. 3, pp. 1252-1259, Jul. 2012

[105] S. Boyd. “Orthonormal sets of vectors and QR factorization”. [Online]. Available: https://see.stanford.edu/materials/lsoeldsee263/04-qr.pdf.

[106] E. Anderson, Z. Bai, J. Dongarra. “Generalized QR factorization and its application”. [Online]. Available: http://web.cs.ucdavis.edu/~bai/publications/andersonbaidongarra92.pdf.

[107] North American Electric Reliability Corporation (NERC). “Update on NERC reliability guideline: PMU placement”. [Online]. Available: https://www.nerc.com/comm/PC/Synchronized%20Measurement%20Subcommittee/SMS%20Meeting%20Presentations%20-%20November%2003-05,%202015%20(San%20Diego,%20CA).pdf.

[108] North American Electric Reliability Corporation (NERC). “2018 frequency response annual analysis”. [Online]. Available: https://www.nerc.com/comm/OC/Documents/2018_FRAA_Report_Final.pdf.

[109] C. Qian and M. Kezunovic, "Synchrophasor reference algorithm for PMU Calibration System," *2016 IEEE/PES Transmission and Distribution Conference and Exposition (T&D)*, Dallas, TX, pp. 1-5, May 2016.

[110] G. Cosoli, L. Casacanditella, F. Pietroni, A. Calvaresi, G. M. Revel and L. Scalise, "A novel approach for features extraction in physiological signals," *2015 IEEE International Symposium on Medical Measurements and Applications (MeMeA) Proceedings*, Turin, Italy, pp. 380-385, May 2015.

[111] Z. Li, M-A Meier, E. Hauksson, Z. Zhan, J. Andrews. "Machine learning seismic wave discrimination: application to earthquake early warning". [Online]. Available: http://web.gps.caltech.edu/~zefengli/papers/Li_etal_GRL_2018.pdf.

[112] K. Umapathy, S. Krishnan and R. K. Rao, "Audio signal feature extraction and classification using local discriminant bases," in *IEEE Transactions on Audio, Speech, and Language Processing*, vol. 15, no. 4, pp. 1236-1246, May 2007.

[113] M. Wang and A. V. Mamishev, "Classification of power quality events using optimal time-frequency representations-Part 1: theory," *IEEE Transactions on Power Delivery*, vol. 19, no. 3, pp. 1488-1495, Jul. 2004.

[114] D. Griffin and J. Lim, "Signal estimation from modified short-time Fourier transform," in *IEEE Transactions on Acoustics, Speech, and Signal Processing*, vol. 32, no. 2, pp. 236-243, Apr. 1984.

[115] X. Zhu, G. T. Beauregard and L. L. Wyse, "Real-time signal estimation from modified Short-Time Fourier Transform magnitude spectra," in *IEEE Transactions on Audio, Speech, and Language Processing*, vol. 15, no. 5, pp. 1645-1653, Jul. 2007.

[116] N.Y. Bey. "Multi-resolution Fourier analysis: time-frequency resolution in xxcess of Gabor-Heisenberg limit. Signal, image, and video processing". vol. 8, no. 4. [Online]. Available: https://link.springer.com/article/10.1007/s11760-013-0582-7.

[117] S. Santoso, E. J. Powers, W. M. Grady and A. C. Parsons, "Power quality disturbance wave-form recognition using wavelet-based neural classifier. I. Theoretical foundation," in *IEEE Transactions on Power Delivery*, vol. 15, no. 1, pp. 222-228, Jan. 2000.

[118] Z-L Gaing, "Wavelet-based neural network for power disturbance recognition and classification," *IEEE Transactions on Power Delivery*, vol. 19, no. 4, pp. 1560-1568, Oct. 2004.

[119] J. L. Rueda, C. A. Juarez and I. Erlich, "Wavelet-based analysis of power system low-frequency electromechanical oscillations," in *IEEE Transactions Power Systems*, vol. 26, no. 3, pp. 1733-1743, Aug. 2011.

[120] J. Barros, R. I. Diego and M. de Apraiz, "Applications of wavelet transform for analysis of harmonic distortion in power systems: a review," in *IEEE Transactions on Instrumentation and Measurement*, vol. 61, no. 10, pp. 2604-2611, Oct. 2012.

[121] G. Strang, T. Nguyen, “Wavelets and Filter Banks”. Wellesley, MA: Wellesley-Cambridge Press, Oct. 1997.

[122] C. Vonesch, T. Blu and M. Unser, "Generalized Daubechies wavelet families," in *IEEE Transactions on Signal Processing*, vol. 55, no. 9, pp. 4415-4429, Sep. 2007.

[123] S.-J. Huang, C.-T. Hsieh and C.-L. Huang, "Application of Morlet wavelets to supervise power system disturbances," in *IEEE Transactions on Power Delivery*, vol. 14, no. 1, pp. 235-243, Jan. 1999.

[124] C. Qian and M. Kezunovic, "A novel time-frequency analysis for power system waveforms based on “pseudo-wavelets”," *2018 IEEE/PES Transmission and Distribution Conference and Exposition (T&D)*, Denver, CO, pp. 1-9, Apr. 2018.

[125] C. Qian and M. Kezunovic, "A power waveform classification method for adaptive synchrophasor estimation," in *IEEE Transactions on Instrumentation and Measurement*, vol. 67, no. 7, pp. 1646-1658, Jul. 2018.

[126] D. A. Kouba. “Determining limits using l’Hopital’s rules”. [Online]. Available: https://www.math.ucdavis.edu/~kouba/CalcOneDIRECTORY/lhopitaldirectory/LHopital.html.

[127] P. M. Djuric and S. M. Kay, "Parameter estimation of chirp signals," in *IEEE Transactions on Acoustics, Speech, and Signal Processing*, vol. 38, no. 12, pp. 2118-2126, Dec 1990.

[128] B. Volcker and B. Ottersten, "Chirp parameter estimation from a sample covariance matrix," in *IEEE Transactions on Signal Processing*, vol. 49, no. 3, pp. 603-612, Mar 2001.

[129] D. Fourer, F. Auger, K. Czarnecki, S. Meignen and P. Flandrin, "Chirp rate and instantaneous frequency estimation: application to recursive vertical synchrosqueezing," *IEEE Signal Processing Letters*, vol. 24, no. 11, pp. 1724-1728, Nov. 2017.

[130] G. N. Stenbakken, "Calculating combined amplitude and phase modulated power signal parameters," *2011 IEEE Power and Energy Society General Meeting*, San Diego, CA, Jul. 2011.

[131] T. Luginbuhl and P. Willett, "Estimating the parameters of general frequency modulated signals," in *IEEE Transactions on Signal Process*ing, vol. 52, no. 1, pp. 117-131, Jan. 2004.

[132] P. Wang, H. Li and B. Himed, "Parameter estimation of linear frequency-modulated signals using integrated cubic phase function," *42nd Asilomar Conference on Signals, Systems and Computers*, Pacific Grove, CA, pp. 487-491, Oct. 2008.

[133] C.T. Kelley. “Iterative method for optimization”. Philadelphia, PA: Society for Industrial and Applied Mathematics (SIAM), Jan. 2009.

[134] W. Yin, “The Barzilai-Borwein method”. [Online]. Available: https://www.math.ucla.edu/~wotaoyin/math273a/slides/Lec4a_Baizilai_Borwein_method_273a_2015_f.pdf.

[135] S. Roweis. “Levenberg-Marquardt optimization”. [Online]. Available: https://cs.nyu.edu/~roweis/notes/lm.pdf.

[136] P. Kundur, N. J. Balu, and M. G. Lauby, “Power system stability and control”. McGraw-Hill, New York, Jan. 1994.

[137] "PMU (PLL-based, positive-sequence) Kundur's two-area system". [Online]. Available: https://www.mathworks.com/help/physmod/sps/examples/pmu-pll-based-positive-sequence-kundur-s-two-area-system.html.

[138] C. Liu, T. Lin, C. Yu and J. Yang, "A fault location technique for two-terminal multi-section compound transmission lines using synchronized phasor measurements," in *IEEE Transactions on Smart Grid*, vol. 1403, no. 1, pp. 113-121, Mar. 2012.

[139] N. Zhou and J. Dagle, "Initial results in using a self-coherence method for detecting sustained oscillations," in *IEEE Transactions on Power Systems*, vol. 30, no. 1, pp. 522-530, Jan. 2015.

[140] IEEE Standard for Phasor Data Concentrators for Power Systems," in *IEEE Std C37.247-2019*, pp.1-44, 10 Sep. 2019.

[141] S. Wang, X. Meng and T. Chen, "Wide-area control of power systems through delayed network communication," in *IEEE Transactions on Control Systems Technology*, vol. 20, no. 2, pp. 495-503, Mar. 2012.

[142] D. Belega and D. Petri, "A real-valued Taylor weighted least squares synchrophasor estimator," *2014 IEEE International Workshop on Applied Measurements for Power Systems Proceedings (AMPS)*, Aachen, Germany, pp. 1-6, Nov. 2014.

[143] A. J. Roscoe, B. Dickerson and K. E. Martin, "Filter design masks for C37.118.1a-compliant frequency-tracking and fixed-filter M-class phasor measurement units," in *IEEE Transactions on Instrumentation and Measurement*, vol. 64, no. 8, pp. 2096-2107, Aug. 2015.

[144] A. Roscoe, “PMU (algorithm) Testing to C37.118.1(a) in software”. [Online]. Available: https://erigrid.eu/wp-content/uploads/2018/04/PMU_Testing.pdf.

APPENDIX A

AUTHOR'S PUBSLISHED WORK

Peer Reviewed Journal Paper

[1] C. Qian and M. Kezunovic, "A power waveform classification method for adaptive synchrophasor estimation," in *IEEE Transactions on Instrumentation and Measurement*, vol. 67, no. 7, pp. 1646-1658, Jul. 2018.

Conference Proceedings

[1] C. Qian and M. Kezunovic, "Synchrophasor reference algorithm for PMU Calibration System," *2016 IEEE/PES Transmission and Distribution Conference and Exposition (T&D)*, Dallas, TX, pp. 1-5, May 2016.

[2] C. Qian and M. Kezunovic, "Dynamic synchrophasor estimation with modified hybrid method," *2016 IEEE Power & Energy Society Innovative Smart Grid Technologies Conference (ISGT)*, Minneapolis, MN, pp. 1-5, Sep. 2016.

[3] M. Kezunovic, A. Esmaeilian, T. Becejac, P. Dehghanian, and C. Qian, "Life-cycle management tools for synchrophasor systems: why we need them and what they should entail," *2016 IFAC Workshop on Control of Transmission and Distribution Smart Grids (CTDSG 2016)*, Prague, Czech Republic, pp. 1-6, Oct. 2016.

[4] C. Qian and M. Kezunovic, "Spectral interpolation for frequency measurement at off-nominal frequencies," *2017 IEEE Power & Energy Society General Meeting*, Chicago, IL, pp. 1-5, Jul. 2017.

[5] Q. Yan, C. Qian, B. Zhang, and M. Kezunovic, “Statistical analysis and modeling of plug-in electric vehicle charging demand in distribution systems,”, *2017 International Conference on Intelligent Systems Applications to Power (ISAP 2017)*, San Antonio, TX, pp. 1-5, Sep. 2017.

[6] C. Qian and M. Kezunovic, "A novel time-frequency analysis for power system waveforms based on “pseudo-wavelets”," *2018 IEEE/PES Transmission and Distribution Conference and Exposition (T&D)*, Denver, CO, pp. 1-9, Apr. 2018.

[7] C. Qian and M. Kezunovic, "Hybridization framework for improved dynamic phasor parameter estimation algorithms," *2019 IEEE Power & Energy Society Innovative Smart Grid Technologies Conference (ISGT)*, Washington, D.C., pp. 1-5, Feb. 2019.

[8] M. Kezunovic, C. Qian, C. Seidl, J. Ren, “Testbed for timing intrusion evaluation and tools for lab and field testing of synchrophasor system”, *IEEE International Conference on Smart Grid Synchronized Measurements and Analytics (SGSMA 2019)*, pp. 1-8, College Station, TX. May 2019.

[9] C. Qian and M. Kezunovic, "Power system fundamental frequency estimation using Unscented Kalman Filter," *2019 IEEE Power & Energy Society General Meeting (PESGM)*, Atlanta, GA, USA, pp. 1-5, Aug. 2019.

APPENDIX B

CIRCUIT ANALYSIS OF POWER SYSTEM DURING ELECTROMAGNETIC TRANSIENTS*

Faults in the power system are essentially sudden interruptions of RLC circuits. Such interruptions may be caused by short circuits, or open circuits. Short circuits may be the result of insulation flashover, and connections between phase-phase and/or phase-ground.

B.1 Symbols and Abbreviations

A_1	amplitude of $i_s(t)$
C	equivalent capacitance of Thévenin equivalent of fault circuit
$i_f(t)$	fault current
$i_s(t)$	steady-state component in fault current
$i_t(t)$	transient component in fault current
L	equivalent inductance of Thévenin equivalent of fault circuit
q, Q	electric charges
Z_1	modulo of the impedance of equivalent fault circuit
R	equivalent resistance of Thévenin equivalent of fault circuit
θ_1	power angle of Thévenin equivalent of fault circuit
ϕ_1	initial phase angle of fault circuit

* The derivation of formulas in this Appendix follows the methods in [65].

B.2 Equivalent Circuit Analysis

As shown in Figure 42 (a), the electric power network is composed of passive components, such as transmission lines, which can be represented by RLC parameters. Within the electric power network, at a given location *F*, a Thévenin equivalent circuit can be acquired w.r.t. to the two-terminal port *F*-*G*, shown in Figure 42 (b). During normal operating conditions, *F* and *G* are not electrically connect, which is represented by an open circuit at *S*.

When a fault occurs at location *F*, the switch *S* closes, resulting in faulty current i_f. The dynamic phenomenon of i_f depends on the parameters of Thévenin equivalent circuit, and is discussed in the following sections.

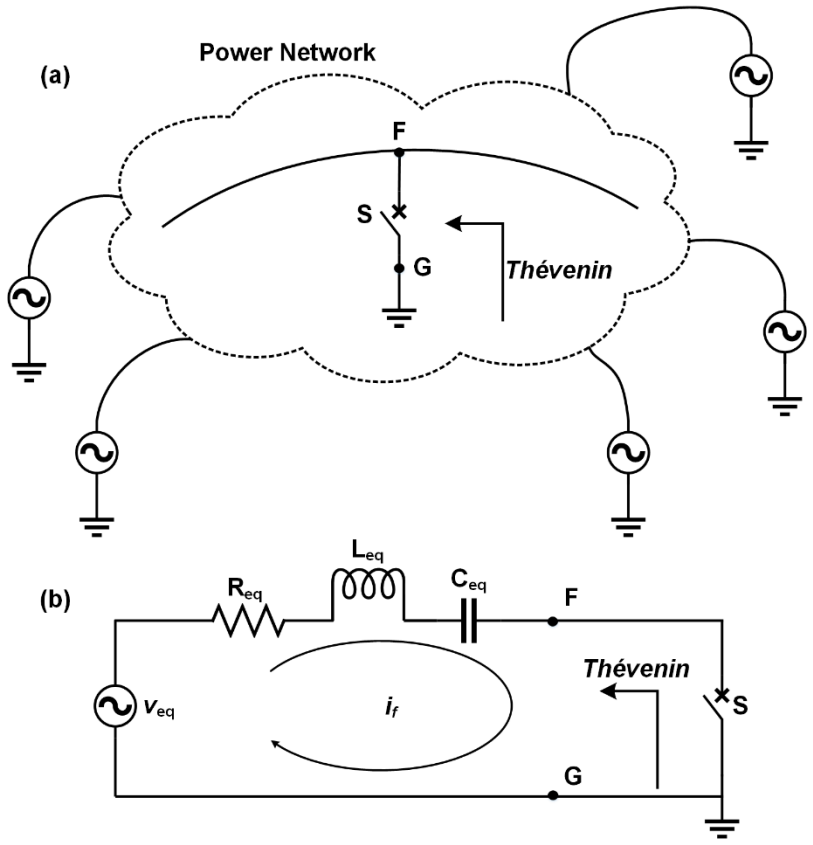

Figure 42 Equivalent circuit of fault in electric power network

B.3 Short Circuit Waveform Analysis

Based on the equivalent circuit shown in Figure 42 (b), the dynamic phenomena of faulty current can be studied by analyzing the transients in the RLC circuit.

Let,

$$v_{\text{eq}}(t) = A_1 \cos(\omega t + \phi_1) \tag{B2.1}$$

According to KVL,

$$v_{\text{eq}}(t) = A_1 \cos(\omega t + \phi_1) = i_f(t) + L\frac{\mathrm{d}i_f(t)}{\mathrm{d}t} + \frac{q(t)}{C} \tag{B2.2}$$

Differentiate equation (B2.2) w.r.t. time,

$$L\frac{\mathrm{d}^2 i_f(t)}{\mathrm{d}t^2} + R\frac{\mathrm{d}i_f(t)}{\mathrm{d}t} + \frac{i_f(t)}{C} = -A_1 \sin(\omega t + \phi_1) \tag{B2.3}$$

The resultant fault current consists of a steady-state component, denoted by $i_s(t)$, and a decaying transient component, denoted by $i_t(t)$.

$$i_f(t) = i_s(t) + i_t(t) \tag{B2.4}$$

where,

$$i_s(t) = \frac{A_1}{Z_1}\cos(\omega t + \phi_1 - \theta_1) \tag{B2.5}$$

where,

$$Z_1 = \sqrt{R^2 + (\omega L - \frac{1}{\omega C})^2} \tag{B2.6a}$$

$$\theta_1 = \tan^{-1}(\frac{\omega L - \frac{1}{\omega C}}{R}) \tag{B2.6b}$$

In steady-state, according to KVL,

$$L\frac{\mathrm{d}^2 i_s(t)}{\mathrm{d}t^2} + R\frac{\mathrm{d}i_s(t)}{\mathrm{d}t} + \frac{i_s(t)}{C} = -A_1 \sin(\omega t + \phi_1) \tag{B2.7}$$

Compared to equation (B2.3), there is,

$$\frac{\mathrm{d}^2 i_t(t)}{\mathrm{d}t^2} + \frac{R}{L}\frac{\mathrm{d}i_t(t)}{\mathrm{d}t} + \frac{i_t(t)}{LC} = 0 \tag{B2.8}$$

The characteristic equation of differential equation (B2.8) is,

$$r^2 + \frac{R}{L}r + \frac{1}{LC} = 0 \tag{B2.9}$$

Solving the characteristic equation,

$$r_{1,2} = \frac{1}{2}\left(-\frac{R}{L} \pm \sqrt{\frac{R^2}{L^2} - \frac{4}{LC}}\right) = -\frac{R}{2L} \pm \sqrt{\frac{R^2}{4L^2} - \frac{1}{LC}} \stackrel{\text{def}}{=} -a \pm b \tag{B2.10}$$

where,

$$a = \frac{R}{2L} \tag{B2.11a}$$

$$b = \sqrt{\frac{R^2}{4L^2} - \frac{1}{LC}} \tag{B2.11b}$$

The complete solution of $i_t(t)$ follows the form:

$$i_t(t) = I_1 e^{r_1 t} + I_2 e^{r_2 t} \tag{B2.12}$$

Therefore, the complete fault current can be expressed by,

$$i_f(t) = \frac{A_1}{Z_1}\cos(\omega t + \phi_1 - \theta_1) + I_1 e^{r_1 t} + I_2 e^{r_2 t} \tag{B2.13}$$

I_1 and I_2 are constant, which is associated with the initial conditions of the circuit. Determined by the physical facts of the circuit, let initial conditions,

$$i(t)|_{t=0} = 0 \tag{B2.14a}$$

$$q(t)|_{t=0} = Q_0 \tag{B2.14b}$$

Imposing initial conditions on equation (B2.13),

$$\frac{A_1}{Z_1}\cos(\phi_1 - \theta_1) + I_1 + I_2 = 0 \tag{B2.15a}$$

$$-\frac{A_1}{Z_1}\sin(\phi_1 - \theta_1)\,\omega L + (I_1 r_1 + I_2 r_2)L + \frac{Q_0}{C} = A_1\cos(\phi_1) \tag{B2.15b}$$

Solve for I_1 and I_2,

$$I_1 = \frac{E_d{}'}{2bL} - \frac{A_1}{2Z_1}\cos(\phi_1 - \theta_1) \tag{B2.16a}$$

$$I_2 = -\frac{E_d{}'}{2bL} - \frac{A_1}{2Z_1}\cos(\phi_1 - \theta_1) \tag{B2.16b}$$

where,

$$E_d{}' \stackrel{\text{def}}{\equiv} A_1\cos(\phi_1) + \frac{A_1}{Z_1}\sin(\phi_1 - \theta_1)\,\omega L - \frac{Q_0}{C} - \frac{A_1 R}{2Z_1}\cos(\phi_1 - \theta_1) \tag{B2.17}$$

As a result,

$$i_t(t) = I_1 e^{(-a+b)t} + I_2 e^{(-a-b)t} \tag{B2.18a}$$

$$i_t(t) = e^{-at}(I_1 e^{bt} + I_2 e^{-bt}) \tag{B2.18b}$$

$$= e^{-at}\left[\frac{E_d{}'}{2bL}(e^{bt} - e^{-bt}) - \frac{A_1}{2Z_1}\cos(\phi_1 - \theta_1)\,(e^{bt} + e^{-bt})\right] \tag{B2.18c}$$

where, $$a = \frac{R}{2L}\,, b = \sqrt{\frac{R^2}{4L^2} - \frac{1}{LC}}$$

The dynamics manifestation of $i_t(t)$ depends on the value of b, and is further discussed below.

CASE 1 $\quad \frac{R^2}{4L^2} > \frac{1}{LC}$

In this case, b is real, and therefore:

$$i_t(t) = e^{-\alpha t}\left[\frac{E_d{}'}{bL}\sinh(bt) - \frac{A_1}{Z_1}\cos(\phi_1 - \theta_1)\cosh(bt)\right] \qquad \text{(B2.19a)}$$

CASE 2 $\quad \dfrac{R^2}{4L^2} < \dfrac{1}{LC}$

In this case, b is imaginary. Let,

$$\alpha = \frac{R}{2L}, b = \mathrm{j}\beta, \beta = \sqrt{-\frac{R^2}{4L^2} + \frac{1}{LC}}$$

Therefore,

$$i_t(t) = e^{-\alpha t}\left\{\frac{E_d{}'}{\beta L}\sin(\beta t) - \frac{A_1}{Z_1}\cos(\phi_1 - \theta_1)\cos(\beta t)\right\} \qquad \text{(B2.19b)}$$

CASE 3 $\quad \dfrac{R^2}{4L^2} = \dfrac{1}{LC}$

In this case, $b \equiv 0$. Note that,

$$\lim_{b\to 0}\frac{(e^{bt} - e^{-bt})}{b} = \lim_{b\to 0}\frac{(te^{bt} + te^{-bt})}{1} = 2t$$

Therefore,

$$i_t(t) = e^{-\alpha t}\left[\frac{E_d{}'}{L}t - \frac{A_1}{Z_1}\cos(\phi_1 - \theta_1)\right] \qquad \text{(B2.19c)}$$

APPENDIX C

DERIVATION OF FREQUENCY PROFILE OF FREQUENCY-MODULATED SIGNAL*

C.1 Symbols

f_0	fundamental frequency
f_m	modulation frequency
$J_\alpha(x)$	Bessel function of the first kind
k_m	modulation level
$x(n)$	input waveform measurements/samples
ϕ_0	initial phase angle of fundamental frequency component
ϕ_m	initial phase angle of frequency modulation component

C.2 Useful Trigonometric Identities

$$J_{-n}(x) = (-1)^n J_n(x) \tag{C2.1}$$

$$\cos(z \cdot \sin\theta) = J_0(z) + 2\sum_{k=1}^{\infty} J_{2k}(z)\cos(2k\theta) \tag{C2.2}$$

$$\sin(z \cdot \sin\theta) = 2\sum_{k=1}^{\infty} J_{2k+1}(z)\sin[(2k+1)\theta] \tag{C2.3}$$

$$\cos(z \cdot \cos\theta) = J_0(z) + 2\sum_{k=1}^{\infty} (-1)^k J_{2k}(z)\cos(2k\theta) \tag{C2.4}$$

---

* Reprinted with authors' permission from C. Qian and M. Kezunovic, "Synchrophasor reference algorithm for PMU Calibration System," *2016 IEEE/PES Transmission and Distribution Conference and Exposition (T&D)*, Dallas, TX, 2016, pp. 1-5. Copyright 2016, IEEE.

$$\sin(z \cdot \cos\theta) = 2\sum_{k=1}^{\infty}(-1)^k J_{2k+1}(z)\sin[(2k+1)\theta] \tag{C2.5}$$

$$\cos(\alpha \pm \beta) = \cos\alpha\cos\beta \mp \sin\alpha\sin\beta \tag{C2.6}$$

C.3 Frequency Profile of Frequency-Modulated Signal

Consider input signal:

$$x(t) = \cos[2\pi f_0 t + k_m \cos(2\pi f_m t + \phi_m) + \phi_0] \tag{C3.1}$$

Apply property (C2.6) to $x(t)$:

$$\begin{aligned} x(t) = {} & \cos(2\pi f_0 t + \phi_0) \cdot \cos[k_m \cos(2\pi f_m t + \phi_m)] \\ & - \sin(2\pi f_0 t + \phi_0) \cdot \sin[k_m \cos(2\pi f_m t + \phi_m)] \end{aligned} \tag{C3.2}$$

Apply properties (C2.1) through (C2.5):

$$\begin{aligned} & \cos[k_m \cos(2\pi f_m t + \phi_m)] \\ & = J_0(k_m) + 2\sum_{k=1}^{\infty}(-1)^k J_{2k}(k_m) \cdot \cos[2k(2\pi f_m t + \phi_m)] \end{aligned} \tag{C3.3}$$

$$\begin{aligned} & \sin[k_m \cos(2\pi f_m t + \phi_m)] \\ & = 2\sum_{k=1}^{\infty}(-1)^k J_{2k+1}(k_m)\sin[(2k+1)(2\pi f_m t + \phi_m)] \end{aligned} \tag{C3.4}$$

Therefore:

$$\begin{aligned} & \cos(2\pi f_0 t + \phi_0) \cdot \cos[k_m \cos(2\pi f_m t + \phi_m)] \\ & = \cos(2\pi f_0 t + \phi_0) \cdot J_0(k_m) \\ & \quad + 2\sum_{k=1}^{\infty}(-1)^k J_{2k}(k_m) \cdot \cos(2\pi f_0 t + \phi_0) \cdot \cos[2k(2\pi f_m t + \phi_m)] \\ & = \cos(2\pi f_0 t + \phi_0) \cdot J_0(k_m) \end{aligned} \tag{C3.5}$$

$$+\sum_{k=0,2,4,\ldots}^{\infty}(-1)^{\frac{k}{2}}J_k(k_m)\{\cos[2\pi(f_0-kf_m)t+\phi_0-\phi_m]$$

$$+\cos[2\pi(f_0+kf_m)t+\phi_0+\phi_m]\}$$

Similarly:

$$\sin(2\pi f_0 t+\phi_0)\cdot\sin[k_m\cos(2\pi f_m t+\phi_m)]$$

$$=\sum_{k=1,3,5,\ldots}^{\infty}(-1)^{\frac{k-1}{2}}J_k(k_m)\{\sin[2\pi(f_0-kf_m)t+\phi_0-\phi_m] \tag{C3.6}$$

$$+\sin[2\pi(f_0+kf_m)t+\phi_0+\phi_m]\}$$

To summarize:

$$x(t)=\cos(2\pi f_0 t+\phi_0)\cdot J_0(k_m)$$

$$+\sum_{k=0,2,4,\ldots}^{\infty}(-1)^{\frac{k}{2}}J_k(k_m)\{\cos[2\pi(f_0-kf_m)t+\phi_0-\phi_m]$$

$$+\cos[2\pi(f_0+kf_m)t+\phi_0+\phi_m]\} \tag{C3.7}$$

$$-\sum_{k=1,3,5,\ldots}^{\infty}(-1)^{\frac{k-1}{2}}J_k(k_m)\{\sin[2\pi(f_0-kf_m)t+\phi_0-\phi_m]$$

$$+\sin[2\pi(f_0+kf_m)t+\phi_0+\phi_m]\}$$

APPENDIX D

DERIVATION OF LINEAR KALMAN FILTER*

In Appendix D, the derivation of linear Kalman filter, is outlined.

D.1 Symbols and Operators

$\boldsymbol{\alpha}(n)$	observation innovation vector, $N\times1$
	$\boldsymbol{\alpha}(n) \stackrel{\text{def}}{=} \boldsymbol{y}(n) - \hat{\boldsymbol{y}}(n\|\mathcal{Y}_{n-1})$
$\boldsymbol{C}(n)$	measurement matrix, $N\times M$
$\boldsymbol{\varepsilon}(n)$	a posteriori state-estimate error vector, $M\times1$
	$\boldsymbol{\varepsilon}(n) \stackrel{\text{def}}{=} \boldsymbol{x}(n) - \hat{\boldsymbol{x}}(n\|\mathcal{Y}_{n})$
$\boldsymbol{\varepsilon}(n, n-1)$	predicted state-estimate error vector, $M\times1$
	$\boldsymbol{\varepsilon}(n, n-1) \stackrel{\text{def}}{=} \boldsymbol{x}(n) - \hat{\boldsymbol{x}}(n\|\mathcal{Y}_{n-1})$
$\boldsymbol{F}(n, n-1)$	state transition matrix from step $n-1$ to n, $M\times M$
$\boldsymbol{G}(n)$	Kalman gain, $M\times N$
$\boldsymbol{K}(n)$	correlation matrix of $\boldsymbol{\varepsilon}(n)$, , $\mathcal{E}[\boldsymbol{\varepsilon}\boldsymbol{\varepsilon}^{\mathrm{H}}]$, $M\times M$
$\boldsymbol{K}(n, n-1)$	correlation matrix of $\boldsymbol{\varepsilon}(n, n-1)$
	$\mathcal{E}[\boldsymbol{\varepsilon}(n, n-1)\boldsymbol{\varepsilon}^{\mathrm{H}}(n, n-1)]$, $M\times M$
$\boldsymbol{P}(n)$	process noise covariance matrix, $\mathcal{E}[\boldsymbol{w}\boldsymbol{w}^{\mathrm{H}}]$, $M\times M$
$\boldsymbol{Q}(n)$	measurement noise covariance matrix, $\mathcal{E}[\boldsymbol{v}\boldsymbol{v}^{\mathrm{H}}]$, $N\times N$

* Reprinted with the permission from C. Qian, M. Kezunovic, "Power system fundamental frequency estimation using unscented Kalman filter," *2019 IEEE Power & Energy Society General Meeting*, Atlanta, GA. 2019. Copyright 2019, IEEE.

$\boldsymbol{R}(n)$	correlation matrix of $\boldsymbol{\alpha}(n)$, $\mathcal{E}[\boldsymbol{\alpha}\boldsymbol{\alpha}^{\mathrm{H}}]$, $N\times N$
$\boldsymbol{x}(n)$	state variable vector at step n, $M\times 1$
$\hat{\boldsymbol{x}}(i\|\mathcal{Y}_k)$	the MMSE estimate of $\boldsymbol{x}(i)$, given observation $\mathcal{Y}_k$, $M\times 1$
$\boldsymbol{v}(n)$	measurement noise, $N\times 1$
$\boldsymbol{w}(n)$	process noise vector, $M\times 1$
$\mathcal{Y}_n$	space spanned by $\boldsymbol{y}(1)$, $\boldsymbol{y}(2)$,…, $\boldsymbol{y}(n)$
$\boldsymbol{y}(n)$	observation vector, $N\times 1$
$\hat{\boldsymbol{y}}(i\|\mathcal{Y}_k)$	the MMSE estimate of $\boldsymbol{y}(i)$, given observation $\mathcal{Y}_k$, $M\times 1$
$\langle a,b\rangle$	inner product of two scalar variables, $\langle a,b\rangle \triangleq^{\text{def}} \mathcal{E}[ab^*]$
$\langle \boldsymbol{a},\boldsymbol{b}\rangle$	inner product of two vector variables, $\langle \boldsymbol{a},\boldsymbol{b}\rangle \triangleq^{\text{def}} \mathcal{E}[\boldsymbol{a}\boldsymbol{b}^{\mathrm{H}}]$

D.2 Basic Philosophy of Kalman Filter

The model of a dynamic system is described as follows:

$$\boldsymbol{x}(n) = \boldsymbol{F}(n, n-1)\boldsymbol{x}(n-1) + \boldsymbol{w}(n) \tag{D.1}$$

$$\boldsymbol{y}(n) = \boldsymbol{C}(n)\boldsymbol{x}(n) + \boldsymbol{v}(n) \tag{D.2}$$

The symbols in (4.3) are explained as follows:

n: step number (scalar)

$\boldsymbol{x}(n)$: state vector at step n ($p \times 1$ vector)

$\boldsymbol{w}(n)$: process noise vector. $E[\boldsymbol{w}(n)\boldsymbol{w}^{\mathrm{H}}(k)] = \boldsymbol{Q}(n)$ for $n = k$; $E[\boldsymbol{w}(n)\boldsymbol{w}^{\mathrm{H}}(k)] \equiv \boldsymbol{0}$ otherwise.

$\boldsymbol{v}(n)$: measurement noise vector.$E[\boldsymbol{v}(n)\boldsymbol{v}^{\mathrm{H}}(k)] = \boldsymbol{P}(n)$ for $n = k$; $E[\boldsymbol{v}(n)\boldsymbol{v}^{\mathrm{H}}(k)] \equiv \boldsymbol{0}$ otherwise. $E[\boldsymbol{w}(n)\boldsymbol{v}^{\mathrm{H}}(k)] \equiv \boldsymbol{0}$ for all n and k.

The dynamic system described in Equations (6.4) and (6.5) can be illustrated in Figure 43.

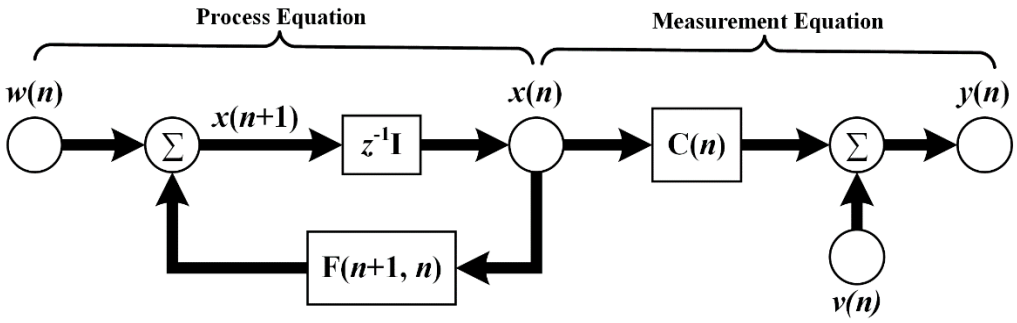

Figure 43 Block diagram representation of linear, discrete dynamic system described by Equations (6.4) and (6.5)

Kalman filter is designed to minimize the MMSE of state vector $\boldsymbol{x}(n)$, given all the observation data $\mathcal{Y}_n \stackrel{\text{def}}{=} \text{span}\{\boldsymbol{y}(1), \boldsymbol{y}(2), \dots, \boldsymbol{y}(n)\}$**.** The best MMSE estimate of state vector $\boldsymbol{x}(n)$ is approached in two steps:

Step 1: Prediction with prior information

Estimate state $\hat{\boldsymbol{x}}(n|\mathcal{Y}_{n-1})$ using last step state $\hat{\boldsymbol{x}}(n-1|\mathcal{Y}_{n-1})$ and state transition. Estimate measurement $\hat{\boldsymbol{y}}(n|\mathcal{Y}_{n-1})$ using the measurement matrix and available measurement data $\mathcal{Y}_{n-1}$.

Step 2: Correcting of predicted state by adding weighted innovations derived from measurements.

The estimation process is optimized in that the information innovation on each step n, defined by $\boldsymbol{\alpha}(n) \stackrel{\text{def}}{=} \boldsymbol{y}(n) - \hat{\boldsymbol{y}}(n|\mathcal{Y}_{n-1})$ is orthogonal to the space spanned by the past innovation terms $\text{span}\{\boldsymbol{\alpha}(1), \boldsymbol{\alpha}(2), \dots, \boldsymbol{\alpha}(n-1)\} \equiv \mathcal{Y}_{n-1}$. The implicit Gram-Schmidt orthogonalization procedure guarantees that the estimate is optimal in the sense of achieving MMSE by minimizing the state estimate error $E\{\|\boldsymbol{x}(n) - \hat{\boldsymbol{x}}(n|\mathcal{Y}_n)\|_2^2\}$.

The Kalman filter uses measurements $\{\boldsymbol{y}(1), \boldsymbol{y}(2), \dots, \boldsymbol{y}(n)\}$ to yield an estimate $\hat{\boldsymbol{x}}(n|\mathcal{Y}_n)$ of the state $\boldsymbol{x}(n)$, so that the estimator is optimal in the sense of achieving MMSE, i.e.,

$$\text{minimize } \|\boldsymbol{\varepsilon}(n)\|_2^2 = \|\boldsymbol{x}(n) - \hat{\boldsymbol{x}}(n|\mathcal{Y}_n)\|_2^2$$

The logic framework of using Kalman filter to achieve an MMSE estimate is,

$$\hat{\boldsymbol{x}}(n|\mathcal{Y}_n) = \hat{\boldsymbol{x}}(n|\mathcal{Y}_{n-1}) + \boldsymbol{G}(n)[\boldsymbol{y}(n) - \hat{\boldsymbol{y}}(n|\mathcal{Y}_{n-1})] \tag{D.3}$$

where $\hat{\boldsymbol{x}}(n|\mathcal{Y}_{n-1})$ is the *a posteriori* estimate of state $\boldsymbol{x}(n)$ given measurements up to $\boldsymbol{y}(n-1)$, $\hat{\boldsymbol{y}}(n|\mathcal{Y}_{n-1})$ is the *a posteriori* estimate of measurement $\boldsymbol{y}(n)$ given measurements up to $\boldsymbol{y}(n-1)$, $\boldsymbol{G}(n)$ is a weight term expressed in terms of posterior covariance matrices, as shown in Appendix C.

The Kalman filter is a recursive process that update the one-step forward prediction $\hat{\boldsymbol{x}}(n|\mathcal{Y}_{n-1}) = \boldsymbol{F}(n, n-1)\hat{\boldsymbol{x}}(n-1|\mathcal{Y}_{n-1})$ with the update between the latest measurement input $\boldsymbol{y}(n)$ and the predicted measurement given past observations $\hat{\boldsymbol{y}}(n|\mathcal{Y}_{n-1})$. The procedure of deriving the Kalman filter essentially abide by the orthogonal projection theorem, guaranteeing the estimator is optimal in a MMSE sense. The derivation of Kalman filter assumes a linear dynamic system model.

The derivation of $\boldsymbol{G}(n)$ (Kalman gain) depending on the aforementioned available information is the key to Kalman filtering. As shown in Section D.4, the $\boldsymbol{G}(n)$ can be acquired with available information.

D.3 Recursive Minimum Least Square Estimator for Scalar Random Variables

In this section, a special case, where the state and observation are both scalar, is presented. The procedure will be generalized to vector and matrix forms in the next section.

Assume based on a set of observations $\mathcal{Y}_{n-1} = \text{span}\{y(1), y(2), \dots, y(n-1)\}$, we found the MMSE estimate of state $\hat{x}(n-1|\mathcal{Y}_{n-1})$ of the corresponding zero-mean scalar random variable $x(n-1)$. Suppose now a new measurement is acquired, denoted by $y(n)$, and it is desirable to obtain the updated the estimate $\hat{x}(n|\mathcal{Y}_n)$ associated with random variable $x(n)$. It is preferable to perform this calculation recursively, in which the update can be expressed in the form of:

$$\hat{x}(n|\mathcal{Y}_n) = \hat{x}(n|\mathcal{Y}_{n-1}) + \boldsymbol{G}(n)[y(n) - \hat{y}(n|\mathcal{Y}_{n-1})] \tag{C.4}$$

where $\hat{y}(n|\mathcal{Y}_{n-1})$ is the prediction of random variable $y(n)$ given all the available information stored in space $\mathcal{Y}_{n-1}$, and thus the term $\alpha(n) \stackrel{\text{def}}{=} y(n) - \hat{y}(n|\mathcal{Y}_{n-1})$ is termed "innovation". By definition, $\alpha(n)$ cannot be expressed using any combinations in space $\mathcal{Y}_{n-1}$, and therefore,

$$\alpha(n) \perp \mathcal{Y}_{n-1} \quad \text{or,} \quad \mathcal{E}[\alpha(n)y^*(k)], k = 1,2, \dots, n-1$$

It is also noticeable that, since the "update" inherited within the new measurement $y(n)$ is denoted equivalently by $\alpha(n)$ and $\hat{y}(n|\mathcal{Y}_{n-1})$, therefore, it can be deduced that,

$$\text{span}\{y(1), y(2), \dots, y(n)\} \equiv \text{span}\{\alpha(1), \alpha(2), \dots, \alpha(n)\}$$

Note that $y(1), y(2), \dots, y(n)$ need not be mutually uncorrelated (orthogonal), but $\alpha(1), \alpha(2), \dots, \alpha(n)$ are orthogonal, since $\alpha(n) \perp \mathcal{Y}_{n-1} = \text{span}\{\alpha(1), \alpha(2), \dots, \alpha(n-1)\}$. The innovation $\alpha(k)$ can be obtained from measurements $\{y(1), y(2), \dots, y(k-1)\}$ through Gram-Schmidt orthogonalization procedure, where,

$$\alpha(1) = y(1) \tag{D.5}$$

$$\alpha(2) = y(2) - \frac{\langle y(2), \alpha(1)\rangle}{\langle \alpha(1), \alpha(1)\rangle}\alpha(1) \tag{D.6}$$

$$\alpha(3) = y(3) - \frac{\langle y(3), \alpha(2)\rangle}{\langle \alpha(2), \alpha(2)\rangle}\alpha(2) - \frac{\langle y(3), \alpha(1)\rangle}{\langle \alpha(1), \alpha(1)\rangle}\alpha(1) \tag{D.7}$$

$$\vdots$$

Next, define the MMSE estimate of $x(n)$ $\hat{x}(n|\mathcal{Y}_n)$ as the linear combination of innovation terms $\alpha(1), \alpha(2), \dots, \alpha(n)$:

$$\hat{x}(n|\mathcal{Y}_n) = \sum_{k=1}^{n} b_k \alpha(k) = \sum_{k=1}^{n-1} b_k \alpha(k) + b_n \alpha(n) \tag{D.8}$$

$$\hat{x}(n|\mathcal{Y}_n) = \hat{x}(n-1|\mathcal{Y}_{n-1}) + b_n \alpha(n) \tag{D.9}$$

where b_k are to be determined.

The goal is to minimize MMSE of state estimate, i.e., $x(n) - \hat{x}(n|\mathcal{Y}_n)$. And this this achieved by setting coefficient b_k values to the *projection* of $x(n)$ onto orthogonal basis $\{\alpha(1), \alpha(2), \dots, \alpha(n)\}$:

$$b_k = \frac{\langle x(k), \alpha(k) \rangle}{\langle \alpha(k), \alpha(k) \rangle} \tag{D.10}$$

Compared with equation C2,

$$G(n) = b_n = \frac{\langle x(n), \alpha(n) \rangle}{\langle \alpha(n), \alpha(n) \rangle}$$

Note that equation C8 is in the form of recursion, and the new estimate $\hat{x}(n|\mathcal{Y}_n)$ can be efficiently achieved by updating the most recent one-step backward value $\hat{x}(n-1|\mathcal{Y}_{n-1})$ with a correction term that embodies the information extracted from the new measurement. This procedure can be generalized to vector state and vector measurement.

D.4 Kalman Filter for Vector Random Variables

The special scalar random variable case discussed in the previous subsection is generalized to vector cases. The procedure is described in Algorithm 2.

Algorithm 2 Kalman Filtering Procedure

1: **INPUT** observations/measurements $\boldsymbol{y} = \{\boldsymbol{y}(1), \boldsymbol{y}(2), \dots, \boldsymbol{y}(n)\}$
2: **KNOWN PARAMETERS** from system equation
Transition matrix: $\boldsymbol{F}(n, n-1)$
Measurement matrix: $\boldsymbol{C}(n)$
Correlation matrix of process noise: $\boldsymbol{Q}(n)$
Correlation matrix of measurement noise: $\boldsymbol{P}(n)$
3: **INITIAL CONDITIONS**
$\hat{\boldsymbol{x}}(1|\mathcal{Y}_0) = E[\boldsymbol{x}(1)]$
$\boldsymbol{K}(1,0) = E\{(\boldsymbol{x}(1) - E[\boldsymbol{x}(1)])(\boldsymbol{x}(1) - E[\boldsymbol{x}(1)])^{\mathrm{H}}\}$
4: **COMPUTATION ITERATION** for $n = 1,2,3 \dots$
Kalman gain:
$\boldsymbol{G}(n) = \boldsymbol{F}(n, n-1)\boldsymbol{K}(n, n-1)\boldsymbol{C}^{\mathrm{H}}(n)[\boldsymbol{C}(n)\boldsymbol{K}(n, n-1)\boldsymbol{C}^{\mathrm{H}}(n) + \boldsymbol{P}(n)]^{-\mathbf{1}}$
Innovation vector:
$\boldsymbol{\alpha}(n) = \boldsymbol{y}(n) - \boldsymbol{C}(n)\hat{\boldsymbol{x}}(n|\mathcal{Y}_{n-1})$
$\hat{\boldsymbol{x}}(n+1|\mathcal{Y}_n) = \boldsymbol{F}(n+1, n)\hat{\boldsymbol{x}}(n|\mathcal{Y}_{n-1}) + \boldsymbol{G}(n)\boldsymbol{\alpha}(n)$
$\boldsymbol{K}(n) = \boldsymbol{K}(n, n-1) - \boldsymbol{F}(n, n+1)\boldsymbol{G}(n)\boldsymbol{C}(n)\boldsymbol{K}(n, n-1)$
$\boldsymbol{K}(n+1, n) = \boldsymbol{F}(n+1, n)\boldsymbol{K}(n)\boldsymbol{F}^{\mathrm{H}}(n+1, n) + \boldsymbol{Q}(n)$

D.5 Unscented Kalman Filter Procedure

The UKF procedure for the dynamic system characterized by equations:

$$\boldsymbol{x}(n) = \boldsymbol{F}[n, \boldsymbol{x}(n-1), \boldsymbol{u}(n)] + \boldsymbol{w}(n) \tag{D.11}$$

$$\boldsymbol{y}(n) = \boldsymbol{C}[n; \boldsymbol{x}(n)] + \boldsymbol{v}(n) \tag{D.12}$$

where $\boldsymbol{F}$ and $\boldsymbol{C}$ are time-varying vector-valued nonlinear functions. The process noise and measurement noise terms are both assumed to be additive. The estimation of state vector $\boldsymbol{x}$ using UKF is demonstrated in Algorithm 3.

Algorithm 3 Unscented Kalman Filtering Procedure

1: **KNOWN PARAMETERS**

$M = \dim\{\boldsymbol{x}(n)\}$

$N = \dim\{\boldsymbol{y}(n)\}$

Parameters that determine the selections of σ-points: α, β, κ

$\lambda = \alpha^2(M + \kappa) - M$

$$W_0^{(m)} = \frac{\lambda}{M + \lambda}$$

$$W_0^{(c)} = \frac{\lambda}{M + \lambda} + (1 - \alpha^2 + \beta)$$

$$W_i^{(m)} = W_c^{(c)} = \frac{\lambda}{2(M + \lambda)}, i = 1,2, \dots ,2M$$

Correlation matrix of process noise: $\boldsymbol{Q}(n)$

Correlation matrix of measurement noise: $\boldsymbol{P}(n)$

2: **INITIALIZATION**

$\widehat{\boldsymbol{x}}(0) = E[\widehat{\boldsymbol{x}}(0)]$

$\boldsymbol{K}(0) = E\{[\boldsymbol{x}(0) - \widehat{\boldsymbol{x}}(0)][\boldsymbol{x}(0) - \widehat{\boldsymbol{x}}(0)]^{\mathrm{H}}\}$

3: **COMPUTATION**

3.1. Determination of σ-points

$\boldsymbol{\chi}_0(n-1) = \widehat{\boldsymbol{x}}(n-1)$

$$\boldsymbol{\chi}_i(n-1) = \widehat{\boldsymbol{x}}(n-1) \pm \left[\sqrt{(M + \lambda)\boldsymbol{K}(n-1)}\right]_i$$

where $\left[\sqrt{(M + \lambda)\boldsymbol{K}(n-1)}\right]_i$ is the i-th column of the matrix square root.

3.2. Time updates

$\boldsymbol{\chi}_i(n|n-1) = \boldsymbol{F}[\boldsymbol{\chi}_i(n-1), \boldsymbol{u}(n)], i = 0,1, \dots ,2M$

$$\widehat{\boldsymbol{x}}(n|n-1) = \sum_{i=0}^{2M} W_i^{(m)} \boldsymbol{\chi}_i(n|n-1)$$

$$\boldsymbol{K}(n|n-1) = \sum_{i=0}^{2M} W_i^{(c)}[\boldsymbol{\chi}_i(n|n-1) - \widehat{\boldsymbol{x}}(n|n-1)]$$
$$[\boldsymbol{\chi}_i(n|n-1) - \widehat{\boldsymbol{x}}(n|n-1)]^{\mathrm{H}} + \boldsymbol{Q}(n)$$

$\boldsymbol{Y}_i(n|n-1) = \boldsymbol{C}[\boldsymbol{\chi}_i(n|n-1)], i = 0,1, \dots ,2M$

$$\boldsymbol{y}(n|n-1) = \sum_{i=0}^{2M} W_i^{(m)} \boldsymbol{Y}_i(n|n-1)$$

3.3. Measurement updates

$\boldsymbol{K}(n) = \boldsymbol{K}(n|n-1) - \boldsymbol{G}(n)\boldsymbol{K}_{yy}(n)\boldsymbol{G}^{\mathrm{H}}(n)$

Algorithm 3 Continued

$$\boldsymbol{K}_{yy}(n) = \sum_{i=0}^{2M} W_i^{(c)} [\boldsymbol{Y}_i(n|n-1) - \widehat{\boldsymbol{y}}(n|n-1)] [\boldsymbol{Y}_i(n|n-1) - \widehat{\boldsymbol{y}}(n|n-1)]^{\mathrm{H}} + \boldsymbol{P}(n)$$

$$\boldsymbol{K}_{xy}(n) = \sum_{i=0}^{2M} W_i^{(c)} [\boldsymbol{\chi}_i(n|n-1) - \widehat{\boldsymbol{x}}(n|n-1)] [\boldsymbol{Y}_i(n|n-1) - \widehat{\boldsymbol{y}}(n|n-1)]^{\mathrm{H}}$$

$$\boldsymbol{G}(n) = \boldsymbol{K}_{xy}(n)\boldsymbol{K}_{yy}^{-1}(n)$$

$$\widehat{\boldsymbol{x}}(n) = \widehat{\boldsymbol{x}}(n|n-1) + \boldsymbol{G}(n)[\boldsymbol{y}(n) - \widehat{\boldsymbol{y}}(n|n-1)]$$

$$\boldsymbol{K}(n) = \boldsymbol{K}(n|n-1) - \boldsymbol{G}(n)\boldsymbol{K}_{yy}(n)\boldsymbol{G}^{\mathrm{H}}(n)$$